NATIONAL TECHNICAL UNIVERSITY OF ATHENS
SCHOOL OF CHEMICAL ENGINEERING
LABORATORY OF INORGANIC MATERIALS TECHNOLOGY

DIPLOMA THESIS

Title

CATHODES FOR ZINC-AIR BATTERIES

by

MARIA MECHILI

Supervisor: Prof. Dr.-Ing. Christos Argirusis

ATHENS, June 2021

ACKNOWLEDGMENTS

I would like to express my gratitude to my supervisor Christos Argirusis, professor at School of Chemical Engineering, NTUA, for giving me the opportunity to research on a subject I was greatly interested in and for his constant support, guidance and encouragement throughout all the progress of this thesis. I offer my special thanks to Dr. Pavlos Pandis, Post-Doctoral Researcher in Laboratory of Inorganic Materials Technology, for his most precious consistent assistance during all the challenges faced when conducting laboratory experiments and his sincere counseling from the beginning of this project. I would also like to thank professor Antonios Karantonis for his kind help providing me with insightful directions of great importance regarding electrochemistry scientific issues. I sincerely thank Christos Vaitsis, PhD candidate in Laboratory of Inorganic Materials Technology, for tirelessly helping me investigate all my questions and sharing all his knowledge regarding laboratory processes. Finally, I should particularly thank my mother, Alketa Mechili, for her incomparable support and inspiration and my sister Ioanna Mechili for her continuous interest and valuable suggestions on laboratory procedures during the conduct of this thesis.

ABSTRACT

Zinc-air batteries (ZABs) are rising contenders for future applications in power sources and storage sectors, due to their intrinsically elevated energy capacity coexisting with eco-friendly characteristics. Although rechargeable aqueous ZABs hold a considerable position in current research reports, their practical large-scale adoption is still obstructed by poor durability and cyclability. The bifunctional electrocatalyst in the cathode appears to be the controlling factor of the efficiency of the zinc-air cell, thus special effort has been invested into discovering effective and low-cost alternatives. Transition metal oxides have invariably been considered as competent ORR and OER electrocatalysts for other energy applications, while perovskites have been recently explored as lower cost candidates. The scope of the present thesis is to investigate the performance of layered perovskites $PrBaCo_2O_{6-\delta}$ (PBC) and $PrBaCo_{1.4}Fe_{0.6}O_{6-\delta}$ (PBCF) when implemented as cathode materials in a laboratory secondary aqueous Zinc Air Cell.

Before moving to the experimental procedure, a theoretical background of the subject is outlined. Firstly, the fundamental operational aspects of zinc air batteries (ZABs) are defined. ZABs function differently from conventional batteries, as the oxidizing material is oxygen from the environment, that enters through the cathode (gas-diffusion electrode) to the system, allowing the battery to possess essentially reduced weight. Then, the principal limitations and recent research advances of each component of ZABs are discussed. It appears that ZABs constitute a complex system whose operation can be restricted by various sources, such as anode passivation and parasitic reactions. Nevertheless, the gas-diffusion electrode remains the most delicate part of ZABs, thus recently a remarkable number of reports are devoted into figuring out efficient and scalable solutions for ZABS cathode materials. The major demand from cathode materials is the simultaneous catalysis of Oxygen Reduction Reaction (ORR) and Oxygen Evolution Reaction (OER) in alkaline media and a resilience throughout consistent cycling of the battery. Considering the continuous recent research for bifunctional electrocatalysts, a brief overview of perovskites applied lately as air electrodes is provided.

In order to evaluate the performance of PBC and PBCF, electrochemical characterization half-cell and full-cell tests were conducted. Half-cell tests were devoted to the verification of electrocatalytic activity of the perovskites, in a three-electrode configuration, via voltammetry techniques. After the catalysis of ORR and OER was confirmed, Linear Sweep Voltammetry was used to estimate OER kinetic parameters, so an overall comparison of the activity of the two perovskites could be derived. Tafel slope was conceived as the main activity descriptor for OER dynamics

Finally, PBC and PBCF catalyst inks were coated on carbon paper (gas diffusion layer) to form cathode electrodes which were applied in a in situ assembled ZAB. Each ZAB was tested as a primary battery system and afterwards towards its rechargeability in the same test protocol and conditions, in order to obtain comparable results for the two catalysts. After measuring the Open Circuit Voltage (OCV) of ZABs, Galvanodynamic Polarization curves were acquired, so as to inspect voltage losses during applied currents. Peak Power Densities were also calculated for each catalyst. Taking into consideration the data from the current scan of the cell, a current density was chosen to conduct a galvanostatic full discharge of each cell for Battery Capacity and Working Voltage determination. Following the primary battery tests, a charge voltage profile was obtained, through galvanostatic charging of the battery and polarization towards OER was inspected. Lastly, the ZABs were submitted to continuous galvanostatic charge-discharge cycling to observe voltage polarizations and test the durability of catalysts.

Both electrochemical half-cell tests and battery tests revealed enhanced performance of Fe-doped PBC comparing to pristine PBC. Tafel slopes of PBCF samples were overall reduced compared to PBC, implying better OER activity of PBCF which was confirmed by following battery tests. Although both catalysts delivered relatively low Specific Capacity, the Peak Powe Density derived from Polarization plots illustrate the potential of the two catalysts to facilitate ORR. During galvanostatic cycling PBCF appears more efficient than PBC it exhibited less extended Voltage Gap throughout its cycle life. It is highlighted that PBCF could attain 130 (20min) cycles at 2.3-3 mAcm^{-2} without exceeding the charging voltage of 2V, verifying the successful limitation of overpotentials during OER, compared to recent reports of catalysts applied in ZABs. Despite the fact that no direct comparison of the two catalysts can be driven, due to lack of morphology, porosity and real surface area information, the improved performance of PBCF could be partially attributed to B-site doping of PBC.

Keywords: Zinc-Air Battery, Cathode, Gas-diffusion electrode, Electrocatalyst, Perovskite

ΠΕΡΙΛΗΨΗ

Οι συσσωρευτές Ψευδαργύρου-Αέρα είναι ανερχόμενοι ανταγωνιστές για μελλοντικές εφαρμογές στους τομείς πηγών και αποθήκευσης ενέργειας, λόγω της εγγενώς υψηλής τους ενεργειακής χωρητικότητας και των φιλικών προς το περιβάλον χαρακτηριστικών τους. Παρ’όλο που οι επαναφορτιζόμενες υδατικές μπαταρίες Ψευδραργύρου- Αέρα κατέχουν μια αξιοσημείωτη θέση στην τρέχουσα έρευνα, η πρακτική τους υιοθέτηση σε μεγάλη κλίμακα προς το παρόν εμποδίζεται λόγω ελλειπούς αντοχής κατά την διεκπεραίωση πολλών κύκλων φόρτισης-εκφόρτισης. Ο διδραστικός ηλεκτροκαταλύτης στην κάθοδο φαίνεται να είναι ο σημαντικότερος παράγων που επηρεάζει την απόδοση του κελιού ψευδαργύρου-αέρα, επομένως έχει γίνει εκτενής προσπάθεια να ανακαλυφθούν αποτελεσματικές εναλλακτικές καταλυτών χαμηλού κόστους. Τα οξείδια μετάλλων μεταπτώσεως ανέκαθεν θεωρούνταν υλικά ικανά να καταλύουν την αντίδραση Αναγωγής και Παραγωγής του Οξυγόνου για ενεργειακές εφαρμογές, ενώ πρόσφατα έχουν μελετηθεί και οι περοβσκίτες λόγω του χαμηλού τους κόστους. Ο σκοπός της παρούσας διπλωματικής εργασίας είναι η διερεύνηση της απόδοσης των διπλών περοβσκιτών $PrBaCo_2O_{6-\delta}$ (PBC) και $PrBaCo_{1.4}Fe_{0.6}O_{6-\delta}$ (PBCF) κατά την εφαρμογή τους ως υλικα καθόδου σε εργαστηριακους υδατικούς συσσωρευτές ψευδαργύρου-αέρα δεύτερου είδους.

Πριν γίνει επεξήγηση της πειραματικής διαδικασίας, περιγράφεται το θεωρητικό υπόβαθρο για τους προαναφερόμενους συσσωρευτές. Πρώτον ορίζονται τα θεμελιώδη χαρακτηριστικά λειτουργίας των συγκεκριμένων μπαταριών. Οι συσσωρευτές Ψευδαργύρου – Αέρα λειτουργούν διαφορετικά από τους συμβατικούς συσσωρευτές, εφόσον το οξειδωτικό υλικό του κελιού είναι το οξυγόνο από το περιβάλλον που εισέρχεται μέσω της καθόδου (ηλεκτρόδιο διάχυσης αέρα) στο σύστημα, επιτρέποντας στο κελί να κατέχει εξαιρετικά μικρό βάρος. Αμέσως μετά, γίνεται συζήτηση σχετικά με τους κύριους περιορισμούς και τις τελευταίες ερευνητικές εξελίξεις για κάθε στοιχείο του κελιού. Είναι φανερό ότι οι μπαταρίες Ψευδαργύρου – Αέρα είναι ένα αρκετά σύνθετο σύστημα του οποίου η λειτουργία μπορεί να περιοριστεί με διάφορους τρόπους, όπως αδρανοποίηση της ανόδου και ανεπιθύμητες χημικές αντιδράσεις. Παρ’όλα αυτά το ηλεκτρόδιο διάχυσης αέρα παραμένει το πιο «ευαίσθητο» στοιχείο της μπαταρίας, κατά συνέπεια, ενας αξιοσημείωτος αριθμός εργασιών είναι αφιερωμένος στην έυρεση αποδοτικών και επεκτάσιμων λύσεων για την κατασκευή της καθόδου. Η κύρια απαίτηση από τα υλικά στην κάθοδο είναι η ταυτόχρονη κατάλυση των αντιδράσεων Αναγωγής (Oxygen Reduction Reaction -ORR) και Παραγωγής (Oxygen Evolution Reaction-OER) του οξυγόνου σε αλκαλικό περιβάλλον, καθώς και η ενθεκτικότητα τους κατά

την διάρκεια συνεχόμενων κυκλων φόρτισης-εκφόρτισης της μπαταρίας. Λαμβάνοντας υπ’όψιν την συνεχή πρόσφατη έρευνα πάνω στους συγκεκριμένους διδραστικούς καταλύτες, παρέχεται επίσης μια σύντομη ανασκόπηση των περοβσκιτών εφαρμοσμένους σε καθόδους αέρα συσσωρευτών ψευδραργύρου-αέρα.

Περνόντας στο πειραματικό μέρος, για να εκτιμηθεί η απόδοση του PBC και PBCF έγιναν ηλεκτροχημικά πειράματα σε διατάξεις τριών ηλεκτροδιών και στον ίδιο τον συσσωρευτή. Στην διάταξη τριών ηλεκτροδίων χρησιμοποιήθηκαν Βολταμετρικές Τεχνικές, αφιερωμένες στον χαρακτηρισμό των περοβσκιτών σε σχέση με ηλεκτροκαταλυτική τους δράση. Εφόσον επιβεβαιώθηκε η καταλυτική δράση των περοβσκιτών, χρησιμοποιήθηκε η Γραμμική Βολταμετρία για την εκτίμηση κάποιων κινητικών παραμέτρων σχετικά με την αντίδραση OER και έτσι έγινε μια πρώτη σύγκριση των δυο υλικών. Το κύριο μέγεθος περιγραφής της δράσης του κάθε περοβσκίτη όσων αφορά το OER ήταν η κλίση Tafel (παράμετρος της εξίσωσης Tafel).

Τέλος, έγινε επικάλυψη των στρωμάτων διάχυσης αέρα άνθρακα από τα διαλύματα με PBC και PBCF και φτιάχτηκαν τα καθοδικά ηλεκτρόδια, για να συναρμολογηθούν οι αντίστοιχοι συσσωρευτές. Ο κάθε συσσωρευτής εξετάστηκε πρώτα σαν πρώτου είδους και ύστερα σαν δεύτερου είδους σχετικά με την επαναφορτισιμότητα του, με την ίδια ακριβώς διαδικασία και συνθήκες για να μπορεί να γίνει έγγυρη σύγκριση των δυο καταλυτών. Αφού μετρήθηκε η Τάση Ανοιχτού Κυκλώματος (OCV) του κάθε συσσωρευτή, έγινε Γαλβανοδυναμική Πόλωση για να εξεταστούν οι απώλειες τάσης κατά την εφαρμογή αυξανόμενων ρευμάτων. Από τις καμπύλες πόλωσης εκφόρτισης υπολογίστηκαν επίσης η μέγιστη ισχύς που ήταν ικανή να παρέχει κάθε μπαταρία. Λαμβάνοντας υπ’οψιν τα δεδομένα από τα παραπάνω πειράματα, επιλέχθηκε το κατάλληλο ρεύμα για κάθε συσσωρευτή έτσι ώστε να γίνει μια Πλήρης Γαλβανοστατική Εκφόρτιση, με στόχο την εύρεση της Χωρητικότητας και της Τάσης Λειτουργίας του. Αμέσως μετά καταγράφηκε η τάση κατά την γαλβανοστατική φόρτιση κάθε συσσωρευτή και παρατηρήθηκε η πόλωση για την αντίδραση φόρτισης (OER). Τέλος, οι συσσωρευτές υποβλήθηκαν σε συνεχομένους γαλβανοστατικούς κύκλους φόρτισης-εκφόρτισης για την συνολική αποτίμηση των πολώσεων και αντοχής των καταλυτών.

Και τα δυο είδη πειραμάτων που έγιναν, σε κελιά τριών ηλεκτροδίων και συσσωρευτές, κατέδειξαν καλύτερη απόδοση του PBCF σε σχέση με το PBC. Οι κλίσεις Tafel για τα δείγματα PBCF ήταν γενικότερα χαμηλότερες από του PBC, συνιστώντας πιο δραστική κατάλυση του OER από το PBCF, ένα συμπέρασμα που επαληθεύτηκε από τα επόμενα πειράματα. Παρ’όλο που οι μπαταρίες με τους δυο περοβσκίτες απέδωσαν αρκετά μικρή Ειδική Χωρητικότητα, οι Μέγιστες Ισχείς από τις Καμπύλες Πόλωσης δείχνουν πως τα δυο υλικά θα μπορούσαν να διευκολύνουν την Αναγωγή του οξυγόνου. Ειδικά κατά τους γαλβανοδυναμικούς κύκλους το PBCF φαίνεται πολύ πιο αποτελεσματικό από το PBC καθώς διατηρεί μια πιο περιορισμένη Διαφορά Τάσης (ανάμεσα στην φόρτιση και εκφόρτιση) καθ΄όλη ην διάρκεια των κύκλων. Σημειώνεται ότι το PBCF άντεξε 130 κύκλους (των 20 λεπτών) σε 2.3-3mAcm^{-2} πυκνότητα ρεύματος χωρίς να ξεπεράσει τα 2V κατά την φόρτιση, εξακριβώνοντας την επιτυχημένη αναστολή της υπερβολικής πόλωσης κατά το OER, σε σχέση με καταλύτες που έχουν πρόσφατα αναφερθεί σε εφαρμογές συσσωρευτών ψευδαργύρου-αέρα. Μολονότι δεν μπορούν να διεξαχθούν άμεσες συγκρίσεις των δύο περοβσκιτών, λόγω έλλειψης μορφολογικών χαρακτηριστικών και χαρακτηριστικών πορώδους και πραγματικής επιφάνειας, η βελτιωμένη απόδοση του PBCF θα μπορούσε να αποδοθεί στην μερική υποκατάσταση της B-θέσης του PBCF από μόρια σιδήρου.

CONTENTS

LIST OF FIGURES x

LIST OF ABBREVIATIONS xiii

1. INTRODUCTION 1

2. ZINC-AIR BATTERY PRINCIPLES 2

  2.1 Configuration 3

    2.1.1 Anode – Zinc Electrode 6

    2.1.2 Electrolyte and Separator 7

    2.1.3 Cathode – Air electrode 10

3. PEROVSKITE-BASED CATALYSTS APPLIED IN ZABS 17

4. EXPERIMENTAL METHODS AND PROCEDURE 21

  4.1 Electrochemical characterization methods 21

    4.1.1 Electrochemical Half-Cell tests 21

    4.1.2 Electrochemical Full Cell- Tests 30

  4.2 Materials and Setups 35

5. RESULTS 39

  5.1 Half-Cell Tests – ORR/OER Evaluation 39

  5.2 Full-Cell tests – Battery Performance 53

6. DISCUSSION AND CONCLUSIONS 67

7. PUBLICATIONS 72

REFERENCES 73

LIST OF FIGURES

Figure 1 : Cubic perovskite unit cell. Blue spheres represent the A cations, yellow spheres represent the B cations, and red spheres represent oxygen anions forming an octahedron [103] 15

Figure 2: Crystal structures of LnBaCo_2O (Ln: lanthanide elements) with various oxygen contents [108].. 16

Figure 3 : Improving mechanisms of the catalytic activity toward ORR and OER of LaMnO_3 perovskite with A-site deficiency. [117] © 2019 Elsevier Ltd. All rights reserved..... 18

Figure 4: Impedance diagrams for electrodes under kinetic (a), diffusional (b), and combined (c; very simple case) control of electrode operation (numbers indicate the frequencies f in kHz), in a Nyquist format.. 22

Figure 5: Schematic idealized impedance complex plane plot for a multicomponent system together with its ideal equivalent electrical circuit [130].. 23

Figure 6: Typical Linear Sweep Voltammetry voltammograms [133] 25

Figure 7: Typical Cycling Voltammetry voltammogram [133].. 28

Figure 8: Half-Cell test configuration; (1) Working Electrode (Coated CC) (2) Counter Electrode (Platinum Mesh) (3) Reference Electrode (Ag/AgCl) 36

Figure 9: Assembling sequence of components in half-cell test configuration: (1) Cathode/WE matrix (2) Carbon cloth pieces (3) Electrolyte and reference electrode (RE) configuration (4) Platinum Counter Electrode.. 37

Figure 9: (a) Zinc- Air cell (b) Cathode oxygen entrance.. 38

Figure 11: Assembling sequence of components in zinc-air cell; (1) Cu Mesh/ Current Collector (2) Zinc polished plate / Anode (3),(5) Separator Membrane (4) Electrolyte entrance (6) Coated carbon paper/ Cathode (7) Ni Mesh/ Current Collector 38

Figure 12 : ORR polarization curves of clean carbon cloth: N_2 Saturated and O_2 saturated... 40

Figure 13 : ORR polarization of PBC catalyst on CC; N_2 Saturated and O_2 saturated............. 41

Figure 14 : ORR Polarization of PBCF catalyst coated on CC; N_2 Saturated and O_2 saturated 42

Figure 14: ORR Polarizations of CP/ PBCF and PBC 43

Figure 16: EIS spectra of (a) CC (b) PBC (c) PBCF in 0.1 M KOH solution 45

Figure 17: OER polarization Curves (a) PBC and (b) PBCF compared to OER Polarization of CC in 0.1 M KOH solution 47

Figure 18: Overpotential of PBC and PBCF samples at a current density of 4mAcm^{-2} 48

Figure 19: Tafel Plots of PBC and PBCF determined from the linear area in voltammetry responses 49

Figure 20: CV profiles of PBC catalyst recorded in 0.1 M KOH solution (a) Sample 1 (b) Sample 2 50

Figure 21: CV profiles of PBCF catalyst recorded in 0.1 M KOH solution (a) Sample 1 (b) Sample 2 51

Figure 22: 10th cyclic voltammogram of PBC and PBCF samples in 0.1 M KOH solution 52

Figure 22: (a) Reduction region of PBC and PBCF (b) Oxidation Region of PBC and PBCF 52

Figure 24: OCV recorded data for (a) CP (b) PBCF coated CP (c) PBC coated CP 53

Figure 25: EIS spectra of each cathode before battery testing 54

Figure 26: Polarization Curves of Zinc-Air cells with (a) CP (b) PBCF coated CP and (c) PBC coated CP cathodes 55

Figure 27: Power density curves of primary Zn–air batteries with (a) CP (b)PBCF coated CP and (c) PBC coated CP cathodes 56

Figure 27: Voltage Profile of Zn-Air Batteries CP(black), PBC coated CP(red) and PBCF coated CP cathodes(blue) 57

Figure 29: Discharge Voltage Profiles and Capacity Determination of Zinc- Air Cell with (a) PBC and (b) PBCF coated CP 59

Figure 29: Charge Voltage Profiles of Zinc- Air Cell with (a) PBCF and (b) PBC coated CP 60

Figure 31: Galvanostatic discharge-charge cycling test of a Zinc-Air cell with a clean CP cathode. 61

Figure 31: Galvanostatic discharge-charge cycling test of a Zinc-Air cell with a PBC coated CP cathode 62

Figure 33: Galvanostatic discharge-charge cycling test of a Zinc-Air cell with a PBCF coated CP cathode 63

Figure 33: Galvanostatic discharge-charge cycling test of a Zinc-Air cell with a (a) PBCF coated CP cathode 63

Figure 35: Voltage Gaps of PBC and PBCF catalysts at (a) 10 hours (b) 30 hours and (c) 40 hours of continuous galvanostatic cycling 64

Figure 36 : EIS spectra of the battery with the PBC coated cathode 65

Figure 37 : EIS spectra of the battery with the PBCF coated cathode 66

LIST OF ABBREVIATIONS

AES	Anion Exchange Membranes
C	Carbon
CC	Carbon Cloth
CE	Counter Electrode
CFP	Carbon Fiber Paper
CNT	Carbon Nanotube
CP	Carbon Paper
DOD	Depth of Discharge
FC	Fuel Cell
FEP	Fluorinated Ethylene Propylene
GDBL	Gas Diffusion Backing Layer
GDL	Gas Diffusion Layer
HER	Hydrogen Evolution Reaction
IL	Ionic Liquid
KOH	Potassium Hydroxide
MPL	Microporous Layer
NaOH	Sodium Hydroxide
NF	Nickel foam
NP	Nanoparticle
NSC	N-S doped carbon

OCV	Open Circuit Voltage
OER	Oxygen Evolution Reaction
ORR	Oxygen Reduction Reaction
PAN	Polyacrylonitrile
PBC	$PrBaCo_2O_{6-\delta}$
PBCF	$PrBaCo_{1.4}Fe_{0.6}O_{6-\delta}$
PEMFC	Proton-Exchange Membrane fuel cell
PTFE	Polytetrafluoroethylene
PVDF	Polyvinylidene fluoride
RDS	Rate-Determinant Step
RE	Reference Electrode
RGO	Reduced Graphene Oxide
SEI	Solid Electrolyte Interphase
SOC	State of Charge
TMO	Transition Metal Oxide
WE	Working Electrode
PPB	Triple-Phase Boundary
ZAB	Zinc - Air Battery

1. INTRODUCTION

The extensive exploitation of fossil fuels, to satisfy energy demands during the last century, had deteriorating consequences around the globe, particularly disrupting the balance of Earth's atmosphere with the release/existence/production of Green House Gases. Considering the perpetually growing energy requirements, worldwide regulators such as European Commission [1-3] and the United States Environmental Protection Agency (EPA) [4, 5], have already established specific targets and strategies to move towards renewable energy sources, in order to diminish GHG emissions. Along with these renewable, but fluctuating energy sources installations, like solar, wind and hydroelectric energy infrastructures, comes the urgent need of storing the intermittent energy produced [6].

Considering the above storage energy requirements, rechargeable batteries have received tremendous attention in the last decades, not only perceived as energy conversion systems, which can produce electricity from electrochemical reactions/material sources, but mostly as energy storage systems. Batteries offer a viable and efficient solution for storing energy on a large scale, but also in transport vehicles [6, 7]. Among a plethora of well-established technologies, like Li-ion batteries, aqueous metal-air batteries constitute a compelling candidate due to their prominent energy density characteristics, environmental compatibility, low cost, and undisputable safety [8-10]. Common state-of-art materials for metal-air batteries' anodes are Zn, Al, Mg and Li electrodes. Zinc represents an attractive candidate for "greener" battery anodes as it is environmentally friendly and the procedures of recycling it are widely used in Europe, due to the mature technological background of this material [10, 11]. Correspondingly to all metal-air batteries, the key to the attractiveness of liquid Zinc-Air Batteries (ZABs), lies mostly to the adoption of oxygen as a cathode active material **[**12**]**. The air-breathing architecture of ZABs, allows them to perform like a hybrid of traditional batteries and fuel cells. Utilizing oxygen from the environment as a reagent, instead of storing bulky cathode materials, permits ZABs to provide most of their space to anode materials leading to high capacities and high specific energy densities reaching theoretically 1353Whkg^{-1} [13].

To date, the main technological challenge considering electrically rechargeable liquid ZABs commercialization is to develop electrochemically active and cost-effective cathode materials, which overcome sluggish oxygen kinetics and withstand continuous cycling without being depleted [14-17]. Several exceptional reports have been published, highlighting and evaluating novel architectures of air electrodes and rational strategies to synthesize effective

Oxygen Reduction Reaction (ORR) and Oxygen Evolution Reaction (OER) electrocatalysts [18-23]. In the last decade a plethora of efforts have been conducted to investigate the performance of alternative bifunctional electrocatalysts, addressing mostly non-noble nanomaterials like carbonaceous materials [24, 25], single-atom compounds [26] and Transition Metal Oxides (TMOs) [27, 28] . Among them, perovskites have very recently started to gain attention because of the tunability of their composition, leading to oriented intrinsic catalytic activity.

This experimental thesis the oxygen electrocatalytic properties of certain perovskites as cathodes in Zinc-Air Batteries (ZABs) are evaluated. Firstly, a brief discussion of the functions, limitations, and potential developments of each component of the ZAB system is provided, emphasizing on the gas diffusion electrode. Then, recent developments of perovskite materials in ZABs are explored. Finally, this thesis focuses on the electrochemical properties and operation of PBC and PBCF, when applied as air electrodes in a rechargeable ZAB.

2. ZINC-AIR BATTERY PRINCIPLES

Zinc, being an abundant element on earth, since the first voltaic cell was invented, has been thoroughly studied as an anode material for primary batteries and acquired an essential share in commercialized primary batteries. There are many features that establish this material a beneficial and reliable alternative for the fabrication of negative electrodes.

Concerning the battery performance zinc is characterized by electrochemical reversibility, a notable negative standard potential and appears stable in liquid electrolytes. Furthermore, its low cost, accessibility and undisputed safety identify zinc as a scalable solution for electrodes manufacture [29, 30] . Finally, zinc constitutes an attractive candidate for “greener” batteries as it is environmentally friendly and the procedures of recycling it are widely used in Europe [11].

Correspondingly to all metal-air batteries the key to attractiveness of Zinc-Air Batteries (ZABs), besides the properties of zinc, lies to the adoption of oxygen as a cathode active material [12]. Oxygen is a powerful oxidizing reactant available almost everywhere. The air-breathing architecture of ZABs, allows them to perform like a hybrid of traditional batteries and fuel cells. Utilizing oxygen from the environment as a reagent, instead of storing bulky cathode materials, permits ZABs to provide most of their space to anode materials leading to high capacities and surprisingly high specific energy densities reaching theoretically 1086 Wh kg^{-1} [13].

Rechargeable ZABs can be divided to electrically rechargeable and mechanically (or refuelable) rechargeable batteries. In the last case, the charge of the battery is completed by physically replacing the zinc anode with a new one, while disposing off the undesired products like zinc oxides and zincates. On the contrary, electrically rechargeable ZABs have the ability to convert electrical energy back to chemical energy, a procedure which will be illustrated and described subsequently [29]. Both literature review and experimental section of this thesis will concentrate on electrically rechargeable ZABs.

2.1 Configuration

The typical structure of an aqueous electrically rechargeable Zinc – Air cell consists of a zinc electrode, an air electrode, allowing the constant supply of oxygen, and a membrane separator inside the liquid electrolyte (usually Potassium Hydroxide (KOH)) [13, 29]. The operation of this electrically rechargeable cell is based on the continuous exchange of oxygen ions and electrons between electrodes and the redox reactions of zinc and oxygen described briefly by the overall reaction below:

$$\mathrm{Zn} + \frac{1}{2}\,\mathrm{O_2} \leftrightarrow \mathrm{ZnO} \quad \mathrm{E^0} = 1.66\ \mathrm{V\ vs\ SHE} \tag{1}$$

When the cell is discharging, zinc ions are created on the zinc electrode due to reduction and the electrons produced are transferred through an external circuit to the air electrode. Meanwhile, atmospheric oxygen molecules are adsorbed to the permeable air cathode and reduced through the ORR to hydroxide ions. The key in this process is that ORR occurs at all the Triple-Phase Boundaries (TPBs) including interfaces between oxygen (gas), electrolyte (liquid), and electrocatalyst (solid). Instantly, the produced hydroxyl ions travel through the basic solution and the ion-conductive separator reaching the zinc anode and forming zincate ions $Zn(OH)_4^{2-}$. When these ions surpass a specific concentration they further decompose to insoluble zinc oxide (ZnO) [13]. This is the case, when the cell operates as a power generator and the reactions in the alkaline electrolyte are as follows:

Discharging

Zn Anode (Oxidation)

$$\mathrm{Zn} \rightarrow \mathrm{Zn}^{2+} + 2\mathrm{e}^{-} \tag{2}$$

$$\mathrm{Zn}^{2+} + 4\mathrm{OH}^{-} \rightarrow \mathrm{Zn(OH)}_4^{2-} \tag{3}$$

$$\mathrm{Zn(OH)}_4^{2-} \rightarrow \mathrm{ZnO} + \mathrm{H_2O} + 2\mathrm{OH}^{-} \tag{4}$$

<u>Overall:</u>

$$\mathrm{Zn} + 2\mathrm{OH}^{-} \Leftrightarrow \mathrm{ZnO} + \mathrm{H_2O} + 2\mathrm{e}^{-} \quad \mathrm{E}^{0} = -1.26\ \mathrm{V\ vs\ SHE} \tag{5}$$

<u>Air Cathode (Oxygen Reduction Reaction)</u>

$$\mathrm{O_2} + 2\mathrm{H_2O} + 4\mathrm{e}^{-} \rightarrow 4\mathrm{OH}^{-} \quad \mathrm{E}^{0} = 0.4\ \mathrm{V\ vs\ SHE} \tag{6}$$

When the cell is charging, electrical energy is converted to chemical as the OER is taking place on the air electrode and electrolyte interface. In the same time oxygen is released from the air electrode, zinc is deposited on the zinc electrode. The mentioned reactions are reversed:

Charging

Zn Anode (Reduction)

$$\mathrm{ZnO + H_2O + 2OH^- \rightarrow Zn(OH)_4^{2-}} \qquad (7)$$

$$\mathrm{Zn(OH)_4^{2-} \rightarrow Zn^{2+} + 4OH^-} \qquad (8)$$

$$\mathrm{Zn^{2+} + 2e^- \rightarrow Zn} \qquad (9)$$

Air Cathode (Oxygen Evolution Reaction)

$$\mathrm{4OH^- \rightarrow O_2 + 2H_2O + 4e^- \quad E^0 = -0.4\ V\ vs\ SHE} \qquad (10)$$

Overall:

$$\mathrm{ZnO + H_2O + 2e^- \rightarrow Zn + 2OH^- \quad E^{\,0} = 1.26\ V\ vs\ SHE} \qquad (11)$$

As outlined above, the theoretical voltage of a secondary Zinc-Air Cell reaches 1.66 V. However, it is observed that the open-circuit voltage of a cell is around 1.4 V and when the cell is being cycled in high current densities the voltage can range from 0.8 V to more than 2 V [31]. These variations of charge and discharge voltages can be measured by specific half-cell and full-cell electrochemical tests, and they depict the state of health and effectiveness of the battery. Current battery scale-up requirements are focusing mainly on high-rate charging without early degradation by extensive overpotentials. The above characteristics are highly driven by the cathode’s performance [9]. Catalysts appear to be needed in order to accelerate ORR and OER described above, while preventing voltage losses to occur in high charging rates.

Such catalysts are denoted as bifunctional, and the produced gas-diffusion electrodes which can endure charging and discharging cycles are denoted as bifunctional air electrodes [29, 31, 32]. Prior to carefully analyzing the vital functionalities of bifunctional catalysts, some typical features of the rest components of the cell will be inspected.

2.1.1 Anode – Zinc Electrode

Primary zinc-based cells have been excessively investigated and used through the globe for about 100 years and more. [29] Some basic characteristics that transformed zinc to such a popular material for batteries, concerning electrochemical performance, compatibility with electrolytes and accessibility, have been already underlined in the introduction. In the case of ZABs though, the requirements of the performance of zinc electrodes are extended, as zinc is the only responsible for the amount of capacity inside the battery and has to maintain this capacity for long-term duration and multiple cycles [33, 34].

There are many cases during the lifetime of the cell where the efficiency of zinc electrodes is restricted and often causes failure of the system, while respectively many solutions have been proposed through the years. The above facts have been described thoroughly by recent reviews [33, 35, 36] , however it would be beneficial to provide a brief examination of them.

Dendrites are one of the morphologies that may appear on a zinc electrode resulting from increased currents and are widely known for their destructive effects on the battery's capacity and efficiency. There are cases when zinc dendrites are able to penetrate the separator and cause failure of the whole cell system by internal short circuit [37]. These morphologies consist of leaf-like or tree like single zinc crystallites and are developed while the active material is redistributed on the zinc electrode [34]. Guo, L., et al. [37] explained precisely the mechanism of dendrites growth, underlining that the principle of this unlike redistribution of zinc particles is that zinc ions are more likely to be deposited on already formed nucleus rather than produce new ones due to lower energy needs. A variety of uneven local shape changes are observed on zinc electrodes depending mainly on the non-uniform current density distribution causing electrolyte concentration differences on the interface between the electrolyte and the electrode [34, 35] .

Passivation constitues another factor that eradicates the activity of a zinc electrode. When the cell is discharging, and zinc is oxidized, the amount of $Zn(OH)_4^{2-}$ ions may surpass their solubility limit leading to the formation of a compact layer of percipitated ZnO on the electrode surface. In this way active sites become limited and the total resistance is elevated leading to charge and discharge overpotentials, and thus low operating voltage and lifetime of the cell [35, 36].

When the cell is charging, a parasitic reaction often takes place near the zinc anode. Hydrogen evolution reaction (HER) is thermodynamically favored compared to zinc deposition (equ. 10) as the standard potential needed for HER to occur is $E^0 = 0.83\ V\ vs\ SHE$.

$$2H_2O + 2e^- \rightarrow 2OH^- + H_2 \qquad E^0 = -0.83\ V\ vs\ SHE \qquad (12)$$

$$Zn + H_2O \rightarrow Zn(OH)_2 + \uparrow H_2 \qquad (13)$$

While hydrogen is generated, the electroactive zinc material is decreased having a deteriorating impact on capacity retention and coulombic effiecincy of the battery. Furthermore internal pressure augments and pH disruptions are created in the electrolyte due to water depletion [34, 35, 38] .

In general, it is obvious that these limitation factors of zinc electrodes' performance are codependent with each other and fundamentally associated with the alkaline solution inside the cell. Hence, the strategies followed to tackle each factor are expanded not only to electrode modifications but also electrolyte adjustments and have to be examined in detail in order to ensure that they do not trigger other destructive mechanisms [34]. Modification of the electrode may include pretreatment methods, intrinsic structure adaptation in order to increase surface, incorporation additives, alloying or coating [33, 35]. On the other side, electrolytes can be reinforced by gelling agents and binders or organic and inorganic additives [36]. In some cases, even the separator is mentioned to help mitigate the above limitations, in ways that will be described in the next chapter.

2.1.2 Electrolyte and Separator

The electrolyte constitutes the intermediate between the anode and cathode, completing the electric circuit of the cell. It functions as the mean in which the ions are exchanged between the electrodes. Thus, the intrinsic properties an electrolyte should have are [29]:

- Sufficient ionic conductivity in order to diminish ohmic resistances. IR polarization has a crucial role in practical application of the cell
- Chemical stability concerning its contact with electrode materials to avoid chemical reactions
- Stable operation during temperature changes
- Electronic insulation to avoid short-circuiting
- Safety and environmental friendliness
- Low cost

Potassium Hydroxide (KOH) and sodium hydroxide (NaOH) have been dominant aqueous alkaline electrolytes for ZABs over the years and appear to have great influence on the processes during the operation of the cell [39]. Despite of their wide use and fundamental advantageous properties these electrolytes are closely related to reduced thermodynamic stability of the zinc electrode and other reasons of battery failure such as absorption of water, potential evaporation, precipitation of insoluble carbonates and limited usable potential window [10, 14, 37, 41]. Taking into consideration the above discussion about the importance of an efficient cooperation of the zinc anode and the electrolyte in order to avoid detrimental phenomena, it appears that the construction of the electrolyte possesses a crucial role regarding rechargeability and prominent cycle life of the battery.

In this context, plenty efforts from experimental studies have been devoted to developing appropriate additives to mitigate such limitations. Mainar, A.R., et al. [34] provide a detailed review of such additives and their activity concerning the cell performance. Authors conclude that ZnO saturation is always beneficial to prevent zinc dessolution but additives based on carbonates and/or fluoride are demanded to offer a synergetic improvement of the electrolyte system.

Moreover, the scientific community lately has started to address solutions different from alkaline aqueous electrolytes. A plethora of studies report the development of aqueous neutral electrolytes [40] acidic electrolytes and non-aqueous electrolytes in order to prevent some of the aforementioned problems occurring between zinc anodes and alkaline aqueous electrolytes [41]. Despite the progress in these studies and the advantages of these novel electrolytes, they still suffer from low ionic conductivity, toxicity, flammability and complicated or demanding manufacturing processes. In fact, according to a very recent review, [42] among solid polymers, gel polymers, ionic liquids (ILs) and deep eutectic solvents

(DES) the last category was found to be the most promising non-aqueous electrolyte solution. The reason is that, while they have similar benefits with ILs concerning conductivity, chemical and thermal stability, as well as potential window they are non-expensive, biodegradable, and simply synthesized.

The role of the electrolyte is supported by a permeable membrane, the separator. The central function of the separator is to physically separate the electrodes in order to prevent their electric contact [29]. Besides being electrochemically and chemically inactive the separator layer should have a specific pore size, porosity and sufficient ionic conductivity to allow selectively the rapid transfer of hydroxide ions and mitigate as much as possible the crossover of zinc cations $Zn(OH)_4^{2-}$ (3). Particularly, when zinc cations are produced from the anode electrode it is common that they are distributed through the electrolyte towards the air electrode where they are dispersed and they block the electroactivity of the catalyst. This phenomenon has a serious impact on the cycle life of the cell [43].

Currently, most of the commercially available separator membranes used in ZABs such as Celgard® 4560, Celgard® 5550 (Celgard LLC), Celgard 2500, Celgard 3501 and Celgard® 3401 [33, 43-45] were originally designed for lithium or nickel based batteries and fuel cells. These membranes are porous laminated polypropylene layers and their broadened use originates from their intrinsic low cost, high electrochemical stability in a wide potential window, low ionic resistance and their ability to withstand dendritic penetration. However, it has been proven that soluble zincate ions are able to crossover such porous membranes, resulting in extensive polarization and effecting durability during continuous cycling.

Numerous strategies have been developed to tackle zincate ions migration while attempting to balance the ionic conductivity of the separator. Most of the studies, concerning aqueous ZABs, concentrate on functionalizing or coating the conventional porous membranes [46-48]while studies regarding flexible designs of zinc air cells, propose novel polymer electrolyte membranes [49-52]. In the second category, alkaline anion exchange membranes (AES) can be highlighted, as they have been given much interest lately with commercial A201® membrane (Tokuyama Corporation, Japan) being dominant in experimental studies [44].

2.1.3 Cathode – Air electrode

2.1.3.1 Architecture

Oxygen, being a gas, will more easily reach the electrolyte through the air, rather than by diffusion through solid mass. Hence, regarding ORR, the optimum fabrication of an air electrode consists of creating as many pathways as possible to allow facile transport of oxygen towards the electrolyte. Such operation can be accomplished through abundant pores [53]. The surface of the material among the pores should be hydrophobic to avoid the invasion of the electrolyte and stabilize gas transport. The sites where oxygen (gas) contacts with the electrolyte (liquid) and the catalyst (solid) are called “triple - phase boundaries” (TPBs) and are the sites where ORR is completed. Correspondingly, regarding OER, hydroxyl ions reach the electrolyte – electrode interface, which is a two-phase zone, in order to produce and release oxygen. To maximize and balance the three-phase and two-phase interfaces, the catalytic surface interacting with the electrolyte has to be hydrophilic [54, 55].

The strategies to manufacture an air electrode, which combines the properties needed for both ORR and OER to occur efficiently, were described thoroughly by Jöerissen, L., [55] and contain concepts where the catalytic layers are separated and catalyze independently OER and ORR respectively. The most facile and cost-effective way, is to manufacture a bifunctional electrode for ZABs by coating one hydrophilic layer of an O_2 bifunctional electrocatalyst on a porous hydrophobic gas diffusion layer (GDL). Organic binders, such as Nafion or Polytetrafluoroethylene (PTFE), are usually mixed with the catalyst inc before the application on the GDL, so that the slurry is attached there tightly [56]. The application of the slurry on the GDL is usually completed by spraying, slurry-coating or drop casting. The electrode is completed with the addition of a current collector onto the electrode’s gas diffusion layer. Metal mesh, expanded metal, nickel foam (NF), carbon fiber (CF), carbon fiber paper (CFP) graphite or carbon cloth (CC) are the most widely used alternatives [54, 55].

2.1.3.2 Gas Diffusion Layer

The gas diffusion layer is a component of the air electrode, that has been extensively investigated regarding fuel cells (FCs) applications. Except for allowing oxygen inlet, physically supporting the catalyst, and forming a conducting mean for electrons to access the current collector, in metal-air batteries it possesses the role of being a barrier for electrolyte leakage or evaporation loss. It also has to endure its performance through strong alkaline media without being oxidized, as ZABs operate with alkaline aqueous electrolytes, unlike Proton-Exchange Membrane fuel cells (PEMFCs) which use polymer electrolytes [57]. In other words, materials for such application, have to be porous, chemically and mechanically resilient, conducting and hydrophobic.

Commercialized GDLs usually integrated on ZABs are made of carbon paper (CP), like SIGRACET® 39 BC [58] and Toray TGP-H-090 [59], while carbon cloth (CC), like PANEX 35 (Zoltek Corporation), have been tested in Li-Air Batteries [60, 61] . Those carbon structures are constructed by two different layers. The layer which will be in contact with the catalyst ink is a microporous layer (MPL) and is synthesized by carbon allotropes, while the gas diffusion backing layer (GDBL) is made of macropores and combines all the fundamental properties of the GDL [62].

In order to extend hydrophobicity of the GDL, and prevent electrolyte infiltration, certain hydrophobic agents (also denoted as binders or conducting polymers) such as PTFE [63, 64] , Polyvinylidene fluoride (PVDF) [65, 66] and fluorinated ethylene propylene (FEP) [67, 68] have been examined. It is proven that the percentage of the conducting polymer affects the performance of the air-breathing electrode, in particular, when the content is low there is high possibility that the electrolyte will enter the oxygen pathways, while when the content is high the active sites get blocked by the binder, leading to increased ohmic resistances and thus overpotentials [57, 69] . However, few studies have been dedicated to optimize the content percentage and fabrication parameters of these agents, when applied to metal-air batteries, in order to balance polarization overpotentials and prolong lifetime of the metal-air battery [57].

There are still challenges to overcome regarding deterioration of the GDL. Most articles that discuss corrosion and endurance of the GDL refer mainly to PEMFCs. To be more precise, more than 40 researches have been publishing since 2006 and are very supportive in understanding the GDL mechanical and chemical degradation processes and the synthesis or environmental factors involved. Researches regarding mechanical erosion and chemical degradation study mainly the effects of compression, temperature, humidity dissolution or continuous gas flow while others outline carbon corrosion mechanisms, in other words chemical degradation [62, 70] .

In the case of metal-air batteries though, reduced charging time is a critical issue, so the operation of the GDL in high current densities should be taken into serious consideration. Furthermore, strong alkaline media and elevated polarization in the ZAB may accelerate or intensify the failure mechanisms of the carbon GDL [71]. Moreover, as aforementioned, there are cases when atmospheric CO_2 reacts with the electrolyte and carbonate precipitates are created, which can travel through the catalytic layer and clog the oxygen-transfer channels. Lastly, in contrast to PEMFCs, the electrolyte in ZABs is liquid, so there are cases where failure, especially due to carbon corrosion, results from electrolyte penetration in the GDL, blocking the pores and often leading to deformation of PTFE [72, 73].

The last decades, most of the studies about development of ZABs' cathodes address issues directly relevant to the reaction, specifically the synthesis and function of effective bifunctional electrocatalysts. There are, though, few references lately about alternative strategies for the construction of prominent GDLs, while many studies report total exclusion of conventional GDLs from the battery and their replacement with a catalyst directly grown on a current collector.

A novel silicon-based material was synthesized by Moni, P., et al. and was tested on a ZAB competing the performance of a conventional commercial CP (SIGRACET® 39 BC). The PTFE-enriched material not only delivered satisfying mechanical and porosity properties, but also was found to enhance the ZAB's cyclability by decreasing charging-discharging potential gaps through more than 200 cycles [58]. In addition, there are researches where PTFE treated carbon is replaced with a combination of PTFE-nickel powder layer on a nickel foam (NF), which possesses the role of the current collector and constitutes the matrix where the electrocatalyst is deposited by dip coating [69] [74]. Both gas diffusion electrodes proved to endure multiple cycles at promising current densities (20 & 50 mA cm^{-2}).

Recently, an electrode composed of CO_3O_4 nanoparticles (NPs) on PTFE-Carbon nanotubes (CNTs) treated NF (denoted as Co_3O_4/Ni/GDL1) outperformed the respective electrode made by commercial CP. The electrode, as well as the constructed aqueous and solid state ZAB, were fully characterized, giving encouraging results concerning particularly cycling durability. The authors highlight that in-situ growth of catalytic NPs, especially after binder treatment, is an effective manner to increase active interfaces between the electrocatalyst and the electrolyte [75],

Besides all the efforts regarding GDL development, some scientists support that the ancillary materials used for conventional electrode preparation add internal resistances to the system and suffer from early degradation, while the binding processes lead to capacity loss [76] [77]. Thus, there have been attempts to directly grow transition metal oxide catalysts on current collectors composed of either NF [76, 78] or stainless steel mesh [77]. In the same context, Zeng, et al. [79] confirm that a self-standing mesoporous $NiCo_2O_4$@N-OCNT film can outperform a conventional electrode without the support of binders, a GDL or a current collector.

2.1.3.3 Catalyst

ORR and OER

When the cell is discharging, the oxygen from the environment is reduced in order to liberate hydroxyl ions OH^- into the electrolyte, while when the cell is charging hydroxide ions are oxidized forming oxygen. These operations correspond to ORR and OER, which are widely known to be complicated and kinetically slow multi-step reactions, whose mechanisms depend on the fundamental features and structure of the electrocatalyst, experimental conditions, like the pH of the solution and concentration of active ions [80, 81] .

Up to date, plentiful mechanisms have been proposed describing ORR and are mainly referring to platinum, platinum-based alloys, gold, and carbon [81]. However, ORR is typically considered to occur in two alternative pathways in alkaline solvents, either a "two electron pathway" or a "four electron pathway" [82]. The first pathway includes primarily generation of hydrogen hydroperoxyl radical HO_2^- and subsequently the production of hydroxyl ions (OH^-) via the transmission of two electrons, as illustrated below:

$$O_2 + H_2O + 2e^- \leftrightarrow HO_2^- + OH^- \quad E^0 = -0.076\,V\ vs\ SHE \tag{14}$$

$$HO_2^- + H_2O + 2e^- \leftrightarrow 3OH^- \quad E^0 = 0.878\,V\ vs\ SHE \tag{15}$$

The "four electron pathway" is widely accepted as more favorable because the reagent is directly transformed to hydroxyl ions (OH^-), without the creation of intermediates, as illustrated in Equation (6) [82, 83].

Even if there is no typical mechanism for ORR applying to all catalysts and the rate-determining step of the reaction has not been recognized, some principal stages that affect the dynamics of ORR can be identified. Firstly, oxygen approaches the transfer channels and potentially undergoes physical adsorption or reaches the three-boundary interface. Secondly, a first electron transfer from the catalyst to oxygen occurs. Subsequently, O-O bonds break and hydroxide ions are produced. Finally, hydroxide ions are liberated through desorption into the electrolyte [81, 84]. Especially when referring to battery applications, ORR is highly dependent on the rate of transfer of oxygen molecules towards the TPBs.

OER is also a complex procedure containing the reverse potential steps, being facilitated more efficiently by metal oxides rather than metals. Correspondingly to ORR due to the presence of alternative intermediates many mechanisms can be assumed to appear depending on the electrocatalyst's geometry and composition [81]. As noted previously OER includes a four-electron transfer as described by the reaction in Eq (10).

The majority of OER mechanisms reported include mainly the following steps [85-87]:

Primarily, a hydroxide anion (OH^-) from the alkaline electrolyte is adsorbed on a metal active site (M) and accepts one electron (formation of M-OH). Afterwards, M-OH is further oxidized to M-O intermediate by the reaction with another hydroxyl radical OH^-. Then, two pathways can be observed to produce molecular O_2. The first one is when two M-O intermediates are immediately combined to generate free O_2 and a metal site. In the second case, hydroperoxide (M-OOH) is formed via one electron oxidation and further interacts with a hydroxyl group to create O_2.

The development of large overpotentials does not allow ORR and OER to be reversible, as the processes are taking place far from the equilibrium, so that the demands on the catalysts in each reaction are different [23]. Platinum (Pt) is denoted as a state-of-art electrode promoting the "four electron pathway", although it delivers poor results regarding OER, while its application is hindered by its high cost and low accessibility. Correspondingly, Ruthenium/Iridium dioxide (RuO_2/IrO_2) is a well-established OER catalyst among various pH ranges but is limited for similar reasons. The above materials are mostly combined in a two-layer electrode to form a typical bifunctional reference electrode for cell performance measurements.

Towards eliminating dependence on precious metal electrodes, carbonaceous materials and transition metals have had a principal role in the research of oxygen electrocatalytic materials in alkaline media the last decade [88-90]. Particularly, towards enhancing intrinsic activity and conductivity, perovskites, among TMOs offer many prospects [23].

The strategies to further refine the electrochemical performance of catalysts vary and are addressed either to activate more surface sites or to modulate their intrinsic activity [23]. In order to establish full availability of active sites (TPBs) and create further active sites, many groups develop unique morphologies (1D, 2D, 3D) and geometric structures (nanorods, nanoplates, nanosheets, nanotubes, nanospheres) of TMOs and perovskites full of edge sites, usually combined with a carbon matrix to achieve maximum dispersity and avoid aggregation [91-98]. Special attention is given to the pore size and pores distribution to allow oxygen transfer, while coupling with carbonaceous nanostructures can also tailor electronic conductivity by introducing more available electron pathways through appropriate interfaces [99-101].

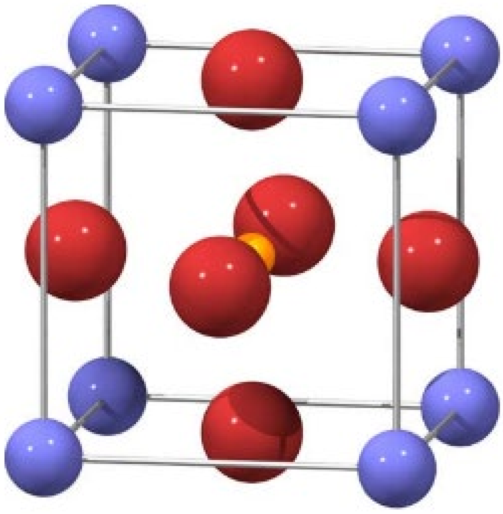

Figure 1 : Cubic perovskite unit cell. Blue spheres represent the B cations, yellow spheres represent the A cations, and red spheres represent oxygen anions forming an octahedron [102]

Moving to tailoring intrinsic activity, perovskites possess an interesting versatility towards promoting electronic and ionic transport through facile and scalable modification of their structure. Perovskites (ABO_3) typically consist of A rare earth metal cations and B transition metal cations forming a cubic structure connecting to oxygen molecules as seen in Figure 1.

Regulating the composition of crystal A and B-sites by doping with different cations can lead to alternative crystalline structures and oxygen vacancies, triggering enhanced electrochemical properties. It is cited that double perovskite materials ($AA'B_2O_{5+\delta}$) exhibit accelerated oxygen diffusion rate than typical ABO_3 perovskites [103]. Furthermore, modifying B-site offers the possibility to create oxygen deficiencies [Figure 2] or to dope with a cation that triggers the existence of higher chemical valences of transition metals. Modulating the optimum cation size and substitution of dopants is a key practice to trigger to promote electronic and ionic transport. [104-106].

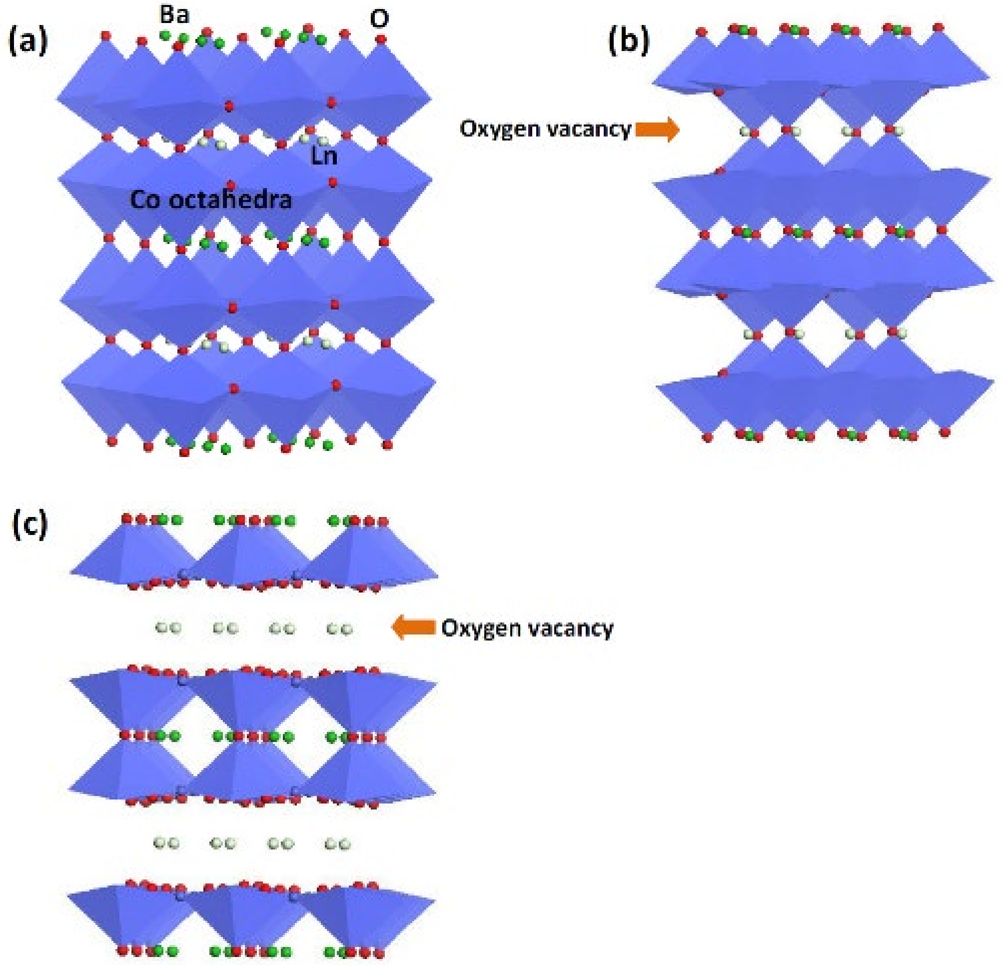

Figure 2: Crystal structures of LnBaCo$_2$O (Ln: lanthanide elements) with various oxygen contents [107]

3. PEROVSKITE-BASED CATALYSTS APPLIED IN ZABS

As aforementioned, perovskites provide the opportunity to modify their A-site or their B-site by partial substituting with another atom in order to modulate the saturated oxygen inside the perovskite. It has been reported that tuning the A-site of the perovskite affects the ionic conductivity of the compound, while tuning the B-site, where the transition metal obtains many oxidation states, affects its electrical conductivity [108-110]. Apparently, besides experimenting on different substitutions, researchers have explored and other strategies to improve electrochemical properties of perovskites, like design of nanofibers through electrospinning, decorating them with precious or non-noble materials and combining them with conductive carbon structures [91, 111-113]. In this section a brief overview of the latest advances in perovskites applied in ZABs is provided.

$LaMnO_3$ is widely used and researched among perovskites for ORR in alkaline media, especially for fuel cells [114]. According to Kuai, L., et al. [115] the synthesis route and the corresponding morphology of $LaMnO_{3-\delta}$ is of critical importance regarding its ORR properties. The same type of perovskite was prepared by a sol gel method by Miao, H., et al. [116] who investigated thoroughly the effects of tuning A-site stoichiometry of La_xMnO_3 on its electrochemical properties [*Figure 3*] . It was proved that adding defective amount of A-site cation in the catalyst could improve all ORR and OER values and stabilize the catalyst comparing to noble commercial catalysts. These bifunctional properties were elucidated by the performance of the in-situ prepared experimental ZAB, while the group clarified the specific mechanisms that contributed to such enhanced activity.

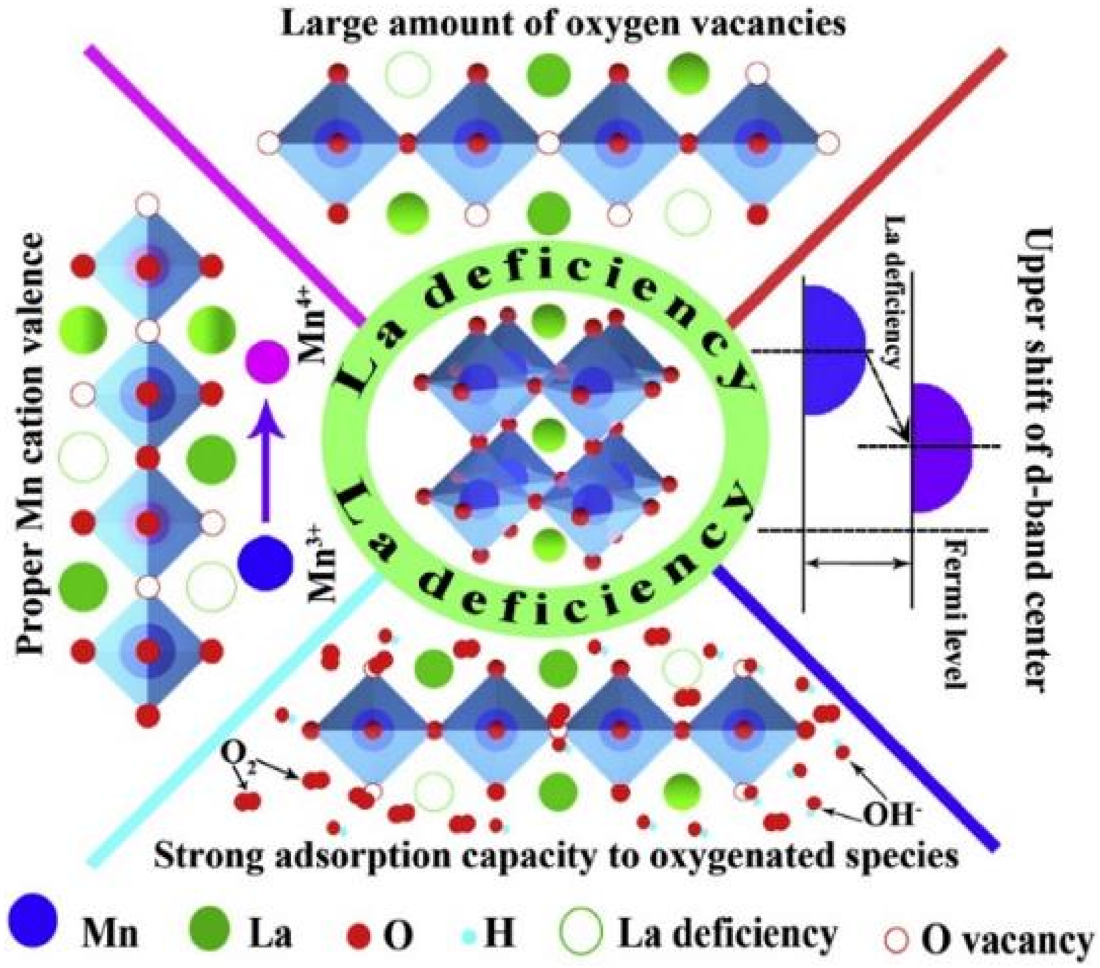

Figure 3 : Improving mechanisms of the catalytic activity toward ORR and OER of LaMnO$_3$ perovskite with A-site deficiency. [116]

In the same direction, researches have been made towards substituting the A-site of perovskite lanthanum cobaltite with calcium, while exploring different morphologies of the corresponding perovskite [117, 118]. Particularly, a silica assisted template method was proposed, resulting to mesoporous La$_{0.6}$Ca$_{0.4}$CoO$_3$ nanosheets that exhibited higher durability than a commercial Pt/C air cathode on ORR and OER tests and delivered remarkable stability when applied to a fabricated ZAB (1000 (20min) cycles at a current density of 10mA cm^{-2}. The voltage gap during the first 900 cycles was stable and limited from 1 -2V [118]. Qian, J., et al. used a typical sol gel process to prepare samples of LaCoO$_3$ derived perovskites, where Ce molecules substituted certain La sites. Among different percentages of Ce doping (0%, 4.2%, 5.6%, and 7.5%) 5.6% was found the most beneficial, with its electronic structure and interactions fully justifying accelerated oxygen transfer and thus good ORR/OER performance [119].

Modifying the B-site of a perovskite is another strategy to experiment on the electronic and ionic conductivity of the perovskite and thus certain experiments have been performed on doping the Co sites of perovskite $PrBa_{0.5}Sr_{0.5}CoO_{5+\delta}$. Lee, H., et al. [120] optimized the Ni doping content of PBSCN particles synthesized through the Pechini method aiming to lower ORR and OER overpotentials and abundant oxygen vacancies. Bu, Y., et al. [111] conducted a similar research, by substituting the B-site of PBSC with Fe, forming $PrBa_{0.5}Sr_{0.5}Co_{1.5}Fe_{0.5}O_{5+\delta}$, although in this case the morphology of the particles were mesoporous nanofibers, prepared by electrospinning. The doped perovskite outperformed both pristine perovskite and a commercial noble air electrode regarding electrochemical activity and stability. The performance of the manufactured ZAB is noteworthy, as it delivered a high peak power density ($128mWcm^{-2}$) and demonstrated the bifunctionality of the catalyst. Electrospinning is a an environmentally benign procedure to produce nanofibers with advantageous highly porous morphologies enriched with exposed active sites, promoting ORR [121]. Zhang, Y., et al. [91] prepared PBSCF nanofibers via a similar electrospinning process and activated further the nanofibers by growing CoP NPS on them through an exsolution approach. The multifunctional catalyst appears to have better ORR and OER characteristics, while delivering better voltage profiles in high polarizations and extended discharge cycles.

In the same year, electrospinning was used to prepare LaNiO3 and 15% Mg2+ doped LaNiO3 (La- Ni0.85 Mg0.15 O3) nanofibers. The two samples adopt very similar dimensions and morphology, although the Mg doped sample exhibits clearly higher oxygen electrode activity, which is verified by its performance in the rechargeable ZAB cathode too. The lab scale ZAB system integrating the corresponding catalyst attained 220 cycles at a current density of $10mAcm^{-2}$ surpassing the durability of the ZAB with the pristine LaNiO3 [122].

In the same direction, Wang, Q., et al. suggested Mn doping in the B-site of $La_{0.8}Sr_{0.2}CoO_3$ perovskite oxide [123]. The catalyst with the optimal Mn/Co ratio was LSCM-60 (60% Mn-40% Co) delivered a high peak power density (around $160mWcm^{-2}$) and endured a remarkably decreased voltage gap for 100 galvanostatic cycles, surpassing the performance of a conventional electrode. The excellent bifunctional features were attributed to abundant Mn3+ /Mn4+ redox couples and raised oxygen absorption/desorption ability.

Doping both A-site and B-site of $La_2NiO_{4+\delta}$ was evaluated by Li, P., et al., by preparing both $La_2NiO_{4+\delta}$ and $La_{1.7}Sr_{0.3}Co_{0.5}Ni_{0.5}O_{4+\delta}$ through a sol-gel method [124]. The higher valence of Co (Co^{3+}) and larger surface area contributed to higher ORR and OER efficiencies of the doped material. The catalyst maintained great stability through long-term cycles of the homemade ZAB, which was charge and discharge cycles in the extensive depth (30min charge & 30min discharge).

Besides tuning the intrinsic properties and morphology of perovskites, researchers have made many attempts to combine perovskites' features with other materials, in order to benefit from their heterostructure and interfaces. Introducing simple molecules, such as noble metals (Ag and Pt), into $SrCoO_{3-\delta}$ (SC)-derived perovskites has been proved to upgrade electrocatalytic properties of these perovskites and enhance the performance of the corresponding assembled ZAB [57, 112].

An approach to functionalize perovskites, as previously mentioned [91], is to incorporate compounds with appropriate features on the surface of the perovskite. $Ce_{0.9}Gd_{0.1}O_{2-\delta}$ (GDC) was used to decorate a $(Pr_{0.5}Ba_{0.5})CoO_{3-\delta}$ (PBC) perovskite, attributing to the composite favorable ORR and OER activity, resulting from the synergistic effect of the ample oxygen vacancies of GDC and catalytic properties of PBC [64]. The durability of the fabricated ZAB for 100 (20min) cycles at a current density of 10 $mAcm^{-2}$ and the limited voltage gap through those cycles strongly signifies the enhanced bifunctionality of the catalyst.

Others developed hybrids with perovskite materials and carbonaceous compounds, such as MWCNTs [101] and Vulcan XC-72 [113]. In both reports, the presence of carbon appears to enrich charge-transporting channels. Particularly, Yan, Z., et al. [113] proposed a environmentally and economically feasible synthesis route, to create a $La_xMnO3_{\pm\delta}$/C hybrid that exhibits promising ORR properties, although its rechargeability was not tested. Majee, R., S. Mondal [101] composed a unique structure of ($BaPrMn_{1.75}Co_{0.25}O_{5+\delta}$, BPMC) nanosheets with *n*-type nitrogen-doped multi-walled carbon nanotubes (NCNT) comprised of functional surface area and interfaces. The collaborative advantages of the perovskite and the CNTs are profoundly displayed from the performance of the ZAB system they were integrated. The catalyst with the optimized CNT content could attain around 80 (1h) cycles at a current density of 5$mAcm^{-2}$.

4. EXPERIMENTAL METHODS AND PROCEDURE

4.1 Electrochemical characterization methods

All electrochemical techniques were applied using a potentiostat (Biologic SP-150, Biologic, and EC- Lab software) under ambient conditions.

All potentials were originally measured vs Ag/AgCl (saturated) electrode and afterwards converted to reversible hydrogen electrode (RHE).

Nernst Equation:

$$E_{\{RHE)} = E_{Ag/AgCl} + 0.059pH + E^0_{Ag/AgCl} \tag{16}$$

Where: $E^0_{Ag/AgCl} = 0.1976\ V$ and for the alkaline solution (0.1M KOH) $pH = 13$. Thus, the final equation to convert potentials is:

$$E_{\{RHE)} = E_{Ag/AgCl} + 0.9646 \tag{17}$$

Current density was calculated referring to the geometric area of the electrode.

4.1.1 Electrochemical Half-Cell tests

4.1.1.1 Electrochemical Impedance Spectroscopy (EIS)

Electrochemical Impedance Spectroscopy is a non-destructive technique usually used to evaluate the internal resistance of the cell over a different range of frequencies, and often used to describe the State of Health and State of Charge of the battery [29]. Instead of driving the system far from the equilibrium, EIS uses small voltage or current sinusoidal perturbations that are assumed to have a linear response. If EIS is used in a potentiostatic mode, the current resulting from a voltage applied in each frequency is measured. Recently, instrumentations can attain frequencies ranging from 10^{-4} to 10^{8} Hz, while the voltage amplitude $V_{m,x}$ must not exceed about 10 mV to ensure that impedance measurements are performed in linear conditions. The wide range of frequency measurements allow us to observe both fast kinetic and slow transport processes as seen in [Figure 4] [125-127] .The response of the system can be displayed in a Bode or a Nyquist format. In this thesis Nyquist format is used, which includes the data from each frequency, plotted by the imaginary part on the y-axis and the real part on the x-axis. A common way to symbolize the axis are -Z_{im} or -Z'' on the y- axis and Z_{re} or Z' on the x-axis.

To depict the system responses in a more comprehensible way, usually models including Equivalent Electrical Circuit Elements are used, with each element representing a source of resistance in the battery system, sourcing from a physical process [128]. Middlemiss, L.A., et al. [129] give a very useful figure including an ideal Nyquist plot of a battery cell and the equicalent circuit [*Figure 5*]

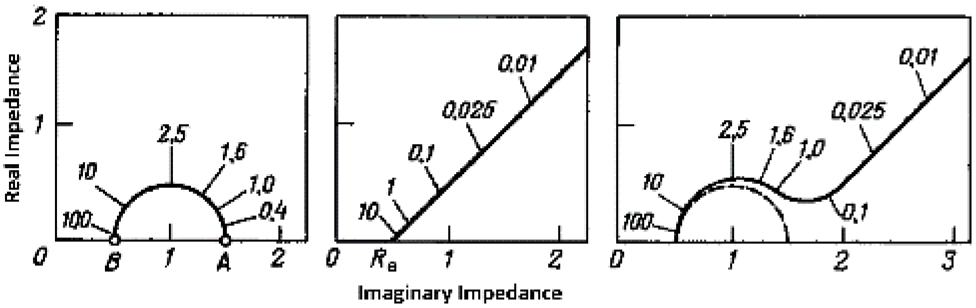

(a) (b) (c)

Figure 4: Impedance diagrams for electrodes under kinetic (a), diffusional (b), and combined (c; very simple case) control of electrode operation (numbers indicate the frequencies f in kHz), in a Nyquist format

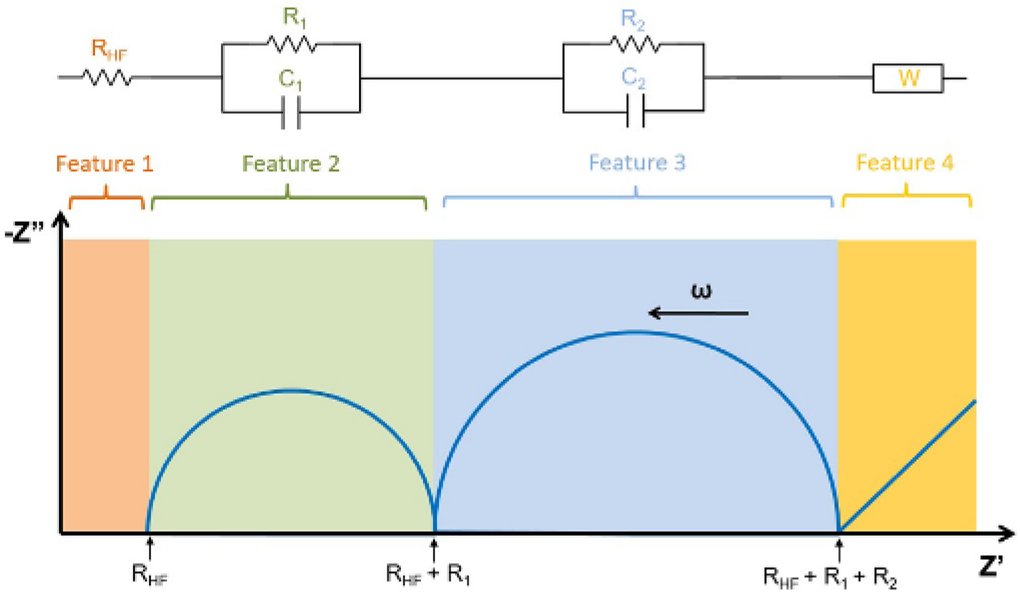

Figure 5: Schematic idealized impedance complex plane plot for a multicomponent system together with its ideal equivalent electrical circuit [129]

The ohmic resistance or electrolyte resistance is found in the bibliography as R_{HF} ("HF" from High Frequency) [129], R_s("s" from solution) [126] or R_E ("E" from electrolyte) and in Nyquist plot is represented by the intersect on the real Z' axis at high frequencies [130] [128]. The representative element of RHF is a resistor. If the electrochemical cell was ideal RHF would be the only impedance, however besides the electrolyte, the overall impedance is influenced by the active material's resistance, the contact between the current collector and active material, the formation of the double layer, as well as ion diffusion. Semi-circles are represented by a resistor (R_{ct}) and capacitor (C_{dl}) in parallel and represent a kinetically controlled charge-transfer process. R_1 and R_2 (often denoted as R_{ct} from charge transfer) are referred to as charge transfer resistances. The impedance derived from diffusion processes (mass transfer resistance), has a form of inclined spike in the Nyquist plot and is often expressed as "Warburg impedance", while it is represented by a non-ideal capacitor, a Warburg element. In Nyquist plots, at high starting frequencies, a "tail" can be found below the real Z' axis, which derives from inductive effects due to experimental setup [29, 129].

In the experimental section, EIS was used in both three-electrode and battery evaluation, in Potentiostatic Mode.

In half-cell tests EIS was used to calculate the ohmic resistance of the cell when measured under OCV. Observing the Nyquist plot of the Impedance done on a three-electrode configuration, the point where the spectrum intersects the real Z’ axis at high frequency, provides an accurate value of the uncompensated ohmic resistance (or solution resistance). In an equivalent circuit R_{HF} or R_s (HF from high frequencies or s from solution) is represented by a resistor [129, 131]. The value R_{HF} was utilized to calculate IR drop, that was compensated to the measured Ewe in OER measurements during Linear Sweep Voltammetry, as it will be explained in section 4.1.1.2.

In full-cell tests, PEIS was used initially to confirm a viable connection of battery components and examine the source of fundamental resistances in the prepared system. Then, after each electrochemical characterization method, PEIS was applied as a non-destructive method to detect potential changes of the resistances inside the battery and inspect their source.

4.1.1.2 Linear Sweep Voltammetry

Linear Sweep Voltammetry (LSV) is a voltametric technique used to analyze the oxidation and reduction processes occurring between a stationary working electrode (WE) and a counter electrode (CE) while using a supporting reference electrode (RE) in a three-electrode configuration. In LSV the potential scan is applied linearly versus time, in a single direction, starting from a potential where no electrode reaction is happening, to either positive potentials (oxidation) or negative potentials (reduction), while measuring the current response [132]. The polarization curves obtained show the relationship between Current (i) and Potential (E) and have usually the following shape:

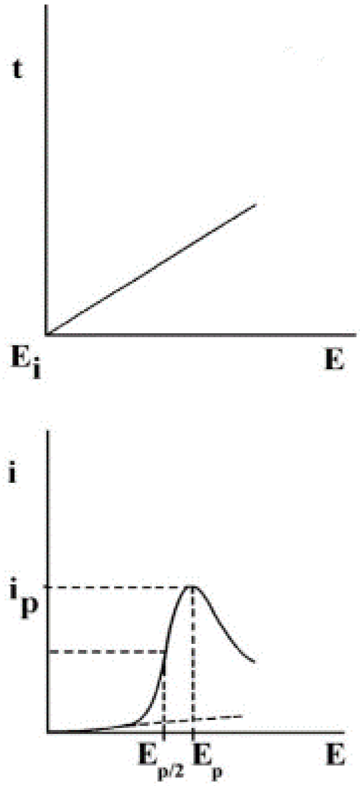

Figure 6: Typical Linear Sweep Voltammetry voltammograms [132]

E is the changing potential and can be calculated:

$$E = E_i \pm vt \tag{18}$$

Where:
t: Time (s)
v: = Scan Rate (Vs^{-1})
E_i: Initial Potential(V)
I_p: Peak Current (A)
E_p: Peak Potential(V)

The reason LSV was performed was to determine the existence and evaluate OER separately, as oxygen reduction is a reaction highly dependent on ion diffusion towards the electrode, thus no kinetic parameters were defined using a stationary electrode.

Considering OER, the LSVs were conducted to compare the performance of the two catalysts throughout the evolution of OH$^-$. This process is not limited by diffusion, as hydroxyl ions can be found abundant throughout the electrolyte and on the surface of the catalyst, even when a stationary electrode is used. In order to preserve near quasi-steady state measurements, the scan rate was low enough around 1mVs^{-1} and in the area of interest, it can be assumed that the system's kinetics can be described by the Butler-Volmer equation, as the concentration of reactants near the electrode is the same with the concentration in the electrolyte.

The Butler-Volmer equation provides a quantitative relationship between an electrode's reaction rate and the applied potential. If the reaction is conducted in one step and can be described by first-order kinetics the B-V equation is formed as shown below [133, 134] :

$$i = i_0 \exp\left(\frac{(1-a)nF}{RT}\eta\right) - \ i_0 \exp(\frac{-\alpha nF}{RT}\eta) \tag{19}$$

Where:

a: charge/discharge transfer coefficient

i_0*: exchange current density (A m^{-2})*

R: gas constant (J K^{-1} mol^{-1})

n: number or transferred electrodes (V)

η: overpotential (E-E^0)(V)

F: Faraday constant (C mol^{-})

T: Temperature (K)

Assuming that:

$$b_a = \frac{2.303RT}{(1-a)nF} \ and \ b_c = \frac{2.303RT}{anF} \tag{20}$$

It can be written:

$$i = \ i_o(10^{\frac{\eta}{ba}} - \ 10^{-\frac{\eta}{bc}}) \tag{21}$$

And for high anodic overpotentials, as in the case for OER exploration, the B-V can be converted to the Tafel Equation as described in Equation 22. The Tafel equation is widely used as an equation describing adequately electron transfer reactions, connecting the rate of a reaction with the overpotential [133, 134].

:

$$\eta = -b_a \log(i^0) + b_a \log(i) \quad \eta >> 0 \tag{22}$$

However, OER is a reaction which is conducted in multiple steps, as mentioned again in 2.1.3.3 Catalyst, whose potential mechanisms have been thoroughly investigated through the years. The rate-determinant step (RDS) of each mechanism can differ depending on the catalyst studied and experimental conditions. The form of B-V equation of course changes when referring to more complex mechanisms and can provide information about the mechanism and RDS. Recently a mechanism involving the participation of lattice oxygen has been proposed for perovskites, however the investigation of the mechanism in the studies system is out of the scope of this thesis[135-137].

In order to give an overview of the overall OER activity and compare the catalyst samples Tafel Equation in a simplified form will be used as shown in Equation 23:

Empirical Tafel Equation:

$$\eta = a + b\log(i) \tag{23}$$

Where: b is the Tafel slope

When studying OER activity of oxygen electrocatalysts, reduced Tafel slope b, indicates accelerated OER dynamics.

To evaluate kinetically the catalysts, special consideration was given to the fact that the measured potential between the working and reference electrode is:

$$E_{measured} = E_{applied} - \Delta E_{Ohmic}$$

Where $\Delta E_{Ohmic} = iR$ (over-potential derived from electron flow)

R: Uncompensated resistance of the electrolyte (Ohm)

Particularly when measuring voltage responses at high current densities, the total ohmic resistance arises. Considering this, before conducting each OER Polarization, PEIS was firstly conducted to determine the solution resistance (Rs), in order to compensate the values of overpotentials.

4.1.1.3 Cyclic Voltammetry

Cyclic Voltammetry (CV) is conducted in the same three-electrode arrangement and framework as LSV, with the difference that the WE is scanned circularly between an upper positive voltage limit and a lower negative voltage limit. CV is a commonly used tool to explore which potential regions stimulate electrochemical activity of a material. A typical cyclic voltammogram trace usually has the following form:

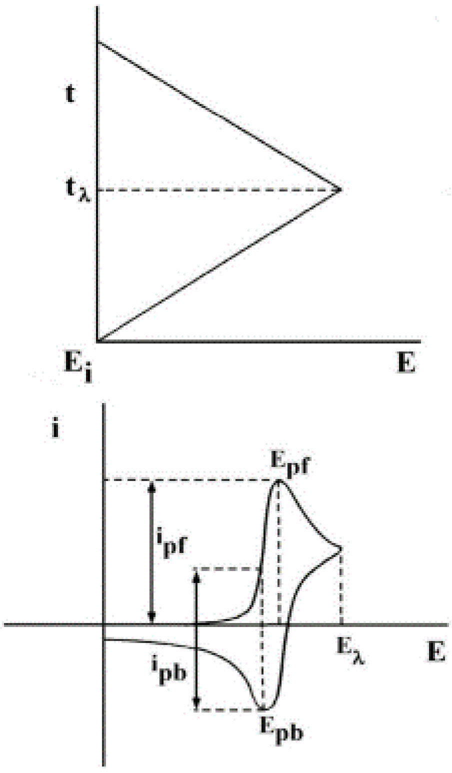

Figure 7: Typical Cycling Voltammetry voltammogram [132]

Where:

t: Time(s)

t_λ : Switching time(s)

E_i: Initial Potential(V)

E_p: Forward peak potential (V)

E_{pb}: Backward peak potential(V)

E_λ: Switching potential (V)

I_{pf}: *Forward Peak Current (A)*

i_{pb}: *Backward Peak Current(A)*

Similarly, with LSV, when an oxidation reaction occurs at the electrodes surface, a positive current is risen, whereas when a reduction reaction occurs, a negative current is observed. The described process is called a “Faradaic process” where the electrons and ions that enter the electrode undergo an electrode reaction and afterwards are liberated again as product species to enter the bulk electrolyte phase. There are also cases when current flow is observed, deriving from “non-Faradaic processes”, where ions are progressively charged on the electrodes surface, without any electron transfer. CVs depicting such processes are out of the scope of this thesis and have a more rectangular form with no distinctive peaks [138].

CV was firstly used to determine the existence of ORR separately. In order confirm this ORR activity the potential range applied was reductive from E_{oc} to -1.5V vs E_{oc} and the scan rate $5mVs^{-1}$. The experiments for both catalysts were qualitative, particularly conducted in order to validate that the activity observed was due to oxygen redox reactions and to discover potential trigger of undesired reactions. Towards this, the three-electrode system was firstly purged 30 min with N_2, while vigorously stirring the electrolyte, to ensure the absence of oxygen in the alkaline media. 2 CVs were performed to clean and activate the sample and one cycle to obtain redox data with absence of oxygen. Then, oxygen was purged in the same system and a second CV was obtained to be compared to the first one and ensure the existence of oxygen electrochemical reactions.

Cycling Voltammetry was also conducted in a potential range -2V to +2V and a current rate $5mVs^{-1}$ in order to observe the overall electrochemical activity of the perovskites in oxidizing and reductive potentials and the reproducibility of these responses in different samples of perovskites. Before recording the main data, 4 cycles were conducted to clean and activate the surface of the electrode. It was also valuable to check if the potential range of activity (peaks attributed to oxygen reactions) changes throughout many cycles. It is not accurate to come into conclusions concerning the overpotential demanded for each reaction to occur observing the voltage gap between the anodic and cathodic reaction as the electrode was stationary and ORR is highly dependent to oxygen molecules diffusion. However, it is possible to make a comparison of the voltage responses of the two catalysts. Finally, it was desirable to detect any other co-existing reactions that may occur during the voltage scan.

4.1.2 Electrochemical Full Cell- Tests

The performance of a battery is a multidimensional subject that can be described by many characteristic metrics. Some metrics such as Open Circuit Voltage (OCV) (V), Working (Operating) Voltage (V), Voltage or Potential Gap (V), Peak Power Density (W/kg), Capacity (Ah), Energy Density Wh/L or Wh/cm^2 refer to Primary battery testing, meaning both non-rechargeable and rechargeable batteries can be characterized by these metrics. Metrics such as Capacity Retention or Coulombic Efficiency refer to rechargeable batteries. The complexity of the performance of a battery lies on the fact that it depends not only on the components of the system but also on the working conditions (e.g., applied current or rate of charge and discharge) and antecedent operation (e.g., cycles, state of charge). Thus, in order to compare materials' performance in a battery system it is of great importance to secure that operational conditions and history are the same.

It is furthermore important to notice that, when testing air cathode materials, researchers tend to compare them with precious catalysts. In this way, firstly the material is directly compared to state-of-art electrodes and secondly authors avoid making misconceptions about the reasons of failure of the battery. In most cases combination of Pt/C and IrO_2 electrode materials are used to construct a comparable cell with the same preparation process.

Similarly with electrochemical methods, the main quantities utilized for battery characterization are Current (A) and Voltage(V). When referring to battery evaluation techniques, there are two main categories of tests that can provide valuable information: Galvanostatic / Potentiostatic techniques and Galvanodynamic/Potentiodynamic techniques. In the first group of techniques, a specific constant current (Galvanostatic) or voltage (Potentiostatic) is applied for a period of time and the response of the other value (voltage or current) is recorded. In the second group of techniques current or voltage are gradually altered (usually linearly) through time and the influence on the other quantity is recorded.

Even if the general direction of evaluation tests is the same, the techniques and parameters used vary according to which component of the cell the experiment focuses on or even the future application of the battery tested. For instance, if a battery is tested for a future EV application, a high rate of charge is of great practical importance, thus *cycling test should be performed with a high charge rate*. However, if a battery is designed for large-scale energy storage, even though high-capacity retention is significant, there is not demand for such high charge rate. Another example could be that, when studying the efficiency of the zinc anode in a ZAB, researchers focus on capacity retention while performing galvanostatic cycles with Depth of Discharge (DOD) > 80%, as the zinc electrode is responsible for the capacity of the cell. Contrarily, when studying electrocatalysts for air cathodes, researchers concentrate on the number of galvanostatic cycles a catalyst can attain, while being cycled in limited DOD <50%. The reason is that in the last case, the subject of interest is the durability and bifunctionality of the catalyst, not the total capacity retention of the battery.

In this study a series of electrochemical tests were conducted to evaluate the cell, focusing on the performance of the catalyst coated on the cathode electrode. The electrochemical tests are thoroughly described in the following pages.

4.1.2.1 Preconditioning of the Battery

The first performance metric of a battery cell is the *Open-Circuit Voltage (OCV)* of the cell. OCV depicts the voltage difference between the anode and the cathode when no current is applied. The theoretical voltage a ZAB can provide is around 1.65 V, but experimental ZABs usually exhibit an OCV around 1.4V. This slight voltage decrease results from the difference between the theoretical and practical concentration of reactants and the fact that the equations calculating the theoretical voltage cannot fully describe the deviations from the real system. Thus, when each Zinc Air cell is constructed the OCV is recorded for 30-60min until it is stabilized, in order to confirm good electrical connection between the components of the ZAB.

After recording the OCV, a low amount of current (around ~1mAcm^{-2}) is applied inside the circuit in order to trigger the gradual formation of the solid electrolyte interphase (SEI) layer. The first step was to galvanostatically discharge the cell for 2 hours, and the second to galvanostatically charge the cell for 2 hours.

PEIS was also conducted, before any operation of the battery had started, so as to ensure good connection between the elements of the cell and obtain information about the main sources of resistances.

4.1.2.2 Primary Battery Testing

In order to evaluate the performance of the cell as a primary battery the first step conducted aims to reveal voltage losses in relation to current variations. This current scan is known as Galvanodynamic Polarization and is commonly used in batteries testing, in order to estimate voltage polarization from the OCV when current is swept linearly towards anodic and cathodic currents. The voltage responses are depicted in a V-I diagram and are called discharge and charge polarization curves. Particularly from the discharge polarization curve valuable information can be obtained, concerning the source of the main voltage losses which can be divided in activation losses, deriving from catalyst activity and Ohmic losses, deriving from electrolyte's resistance and concentration polarization losses.

The *Voltage Gap* between the two polarization curves gives a brief image of the intensity of voltage losses and ideally needs to be as limited as possible. Another characteristic metric that can be recovered from these diagrams is the *Peak Power Density (W/kg)*, which is determined as the maximum value of the Power Density curve constructed from the product of Voltage (V) * Current Density (A/kg). Peak Power Density is a measurement that offers an evident and understandable comparison between different battery cells' performances.

After defining the Current-Voltage profile of the cell the real *Battery Capacity (Ah)*, *Specific Capacity (Ah/kg),* Specific Energy (*Wh/kg), Energy Density (Wh* L^{-1}*, or Wh* cm^{-2}*)* and *Operating (working) Voltage (V)* of the cell need to be determined.

The *Capacity* of a Zinc-Air cell, as the oxidizing material is constantly refilled, is depended to the zinc electrode. It is worth mentioning that typically in ZABs research, Specific Capacity and Specific Energy are preferred to be calculated using the mass or volume of the Zinc Electrode rather than the one of the complete cell probably for comparison reasons. The theoretical capacity (C_T) of a zinc electrode is 819.73 mAhgZn^{-1} and can be calculated by Faraday's law [139]:

$$C_T = \frac{n\,F}{3.6\,(\frac{C}{Ah})MW} = \frac{2 \cdot 96485.3\,\frac{C}{mol}}{3.6\,\frac{C}{Ah} \cdot 65\frac{g}{mol}} \tag{24}$$

Where:

n: number of electrons participating in the redox reaction
F: Faraday's constant (96,485 C mol^{-1}*)*
M.W: molecular weight in $gmol^{-1}$

The practical Capacity (C_p) and Specific Capacity ($C_{p,s}$) of the Cell can be calculated:

$$C_p = I\ (A)t(h) \tag{25}$$

$$C_{p,s} = \frac{I\,(A)t(h)}{M_{Zn}(kg)} \qquad (26)$$

Correspondingly *Specific Energy (Wh/kg)* and *Energy Density (Wh L^{-1}, or Wh cm^{-2})* are also crucial metrics regarding metal-air batteries, describing the quantity of energy storage the device can deliver per unit mass or volume/area of the battery. Literature refers to theoretical Specific Energy ranging from 1,084 $WhkgZn^{-1}$ [140] to 1353 Wh/kg [141] depending on the theoretical or nominal voltage assumed for the calculation. Considering the theoretical voltage 1.65 V and the theoretical capacity 819.73 $mAhgZn^{-1}$ the Energy Density can be calculated:

$$\mathrm{E} = 1.65\ \mathrm{V} \cdot\ 819.73\ \mathrm{mAhg}Zn^{-1} = 1{,}352.55\ \mathrm{mWhgZn}^{-1} \qquad (27)$$

The practical Specific Energy and Energy Density of the cell are calculated:

$$E_S = C_{p,s}(\frac{Ah}{kg})V(V) \qquad (28)$$

$$E_D = \frac{C_p(Ah)}{A(cm^2)}V(V) \qquad (29)$$

When the discharging occurs, the voltage starts dropping from the OCV to a lower value, where it reaches a plateau. This value of Voltage is denoted as the *Working Voltage* (V_w). In Zinc-Air batteries V_w is around 1.2 V and it is desirable that this value remains stable until a high DOD (%). DOD is the percentage of the battery capacity being discharged relatively to the maximum capacity of the battery. After this plateau, the Voltage starts declining again until the battery cannot supply any more power. It is therefore understandable that the value of the Voltage is dependable to the State of Charge (SOC%) of the battery. SOC expressed the remaining capacity of the cell as a percentage of the maximum capacity it can supply.

From the above information it is concluded that when calculating E_S and E_D special consideration should be driven to which value of Voltage will be used.

Those characteristic metrics of the battery are driven from a single plot of galvanostatic discharge. The single parameter decided to galvanostatically discharge a cell is the current demanded, thus the mentioned metrics are highly dependent on the value of fixed discharge current. As much the current rate is elevated the capacity and working voltage that the cell can provide decreases. This phenomenon may be attributed to both facilitation of dendrites formation or early passivation of zinc electrode areas through ZnO precipitates and augmented overpotentials derived from ORR and OER. Consequently, information about the durability of electrodes and voltage losses can be driven from determining the capacity of the cell while discharging with different currents. In any case, when referring to a calculated C_p it is necessary to specify the discharge current of this calculation.

4.1.2.3 Rechargeability Battery Testing

After evaluating the performance of the cell as a primary battery, the catalyst should be tested regarding its bifunctionality. Typically, *Rechargeability* in batteries is tested through galvanostatic charge discharge cycles, from which conclusions can be driven about *Capacity Retention* and *Coulombic Efficiency*.

Capacity Retention is the percentage of discharge capacity of a cycle versus the discharge capacity of a previous cycle (most of the times it refers to the first cycle), while Coulombic Efficiency is the percentage of discharge capacity of a cycle versus the charge capacity of the same cycle [142]. More clearly the equations can be found:

$$\text{Capacity retention} = \frac{C_{discharge\ (n)}}{C_{discharge\ (n-1)}} \tag{30}$$

$$\text{Coulombic Efficiency} = \frac{C_{discharge(n)}}{C_{charge(n)}} \tag{31}$$

The above metrics constitute valuable measurements when comparing batteries' durability, however when researching cathode materials for ZABs they are not often used. The durability of bifunctional catalysts is usually evaluated by shorter cycles (DOD<80%), particularly long-term short cycles of 10-20 min. When conducting those cycling tests, there are more parameters affecting the performance of the cell which are: charge and discharge current, cycle length and cycling number. Regardless the parameters, important information can be driven from voltage profile plots (V-t) of continuous cycling.

Apparently, the number of hours and cycles of continuous cycling can give an overview of the stability of the catalyst. When referring to hours of continuous cycling it is significant to mention the type of cycles conducted and the charge-discharge current. Most importantly, when evaluating a cycling plot, the Voltage gap between the Charging-Discharging voltage gives information about the durability of the bifunctional catalyst.

The initial voltage gap of the first cycles, is preferable to have a value below 1V and as limited it is, the polarization of the catalyst is lower, leading to better performance. It is also desirable that the extend of the voltage gap remains stable throughout all the cycling stability test. Commonly the catalyst can be cycled until the Voltage Gap is prolonged enough to claim that the catalyst is not performing adequately.

4.2 Materials and Setups

Catalyst Preparation

In this work two different perovskite catalysts were examined:

$PrBaCo_2O_{6-\delta}$ (PBC)
$PrBaCo_{1.4}Fe_{0.6}O_{6-\delta}$ (PBCF)

PBC and PBCF were provided as coarse-grained powders, so they been manually grinded in an agate mortar. For the catalyst-ink preparation pure Ethanol was used as a solvent and 5 wt% Nafion^{TM} solution was used as a binder. For every 1mg of catalyst powder, around 3μL Nafion and 100μL Ethanol were added in the solution and sonicated for 40 minutes to achieve better dispersion of the perovskite. For both half and full cell experiments the catalyst loading on the carbon support was done by drop casting. In the half cell configuration, carbon cloth was used as a carbon support for practical reasons, while in the zinc-air cell the conductive gas diffusion layer was CP(d: 190μm). The coating loading of the CC in half-cell tests was 0.6 mgcm^{-2}, while the catalyst loading on CP for battery tests was 1mgcm^{-2}. After coating the corresponding carbon support, the electrodes were either left overnight so Ethanol evaporates, or dried in 80-90℃ for 30min.

Half Cell Tests Configuration

All electrochemical characterizations were carried out in a 320 ml electrochemical cell with two main ports as seen in [*Figure 8*]. The components and their assembling sequence in the system can be found in [*Figure 9*]. The working electrode (WE), reference electrode (RE) and counter electrode (CE) have fixed distances between them, while oxygen or nitrogen could be purged from one entrance of 3 entrances (*Figure 8*). The reference electrode was saturated Ag/AgCl and the counter electrode was commercial Platinum mesh The electrolyte was aqueous solution of 0.1M KOH and 0.05M Sodium Sulfate (Na_2SO_4) which promotes ionic conductivity in the circuit. The exposed surface of the working electrode to the electrolyte is 0.899 cm^{-2}.

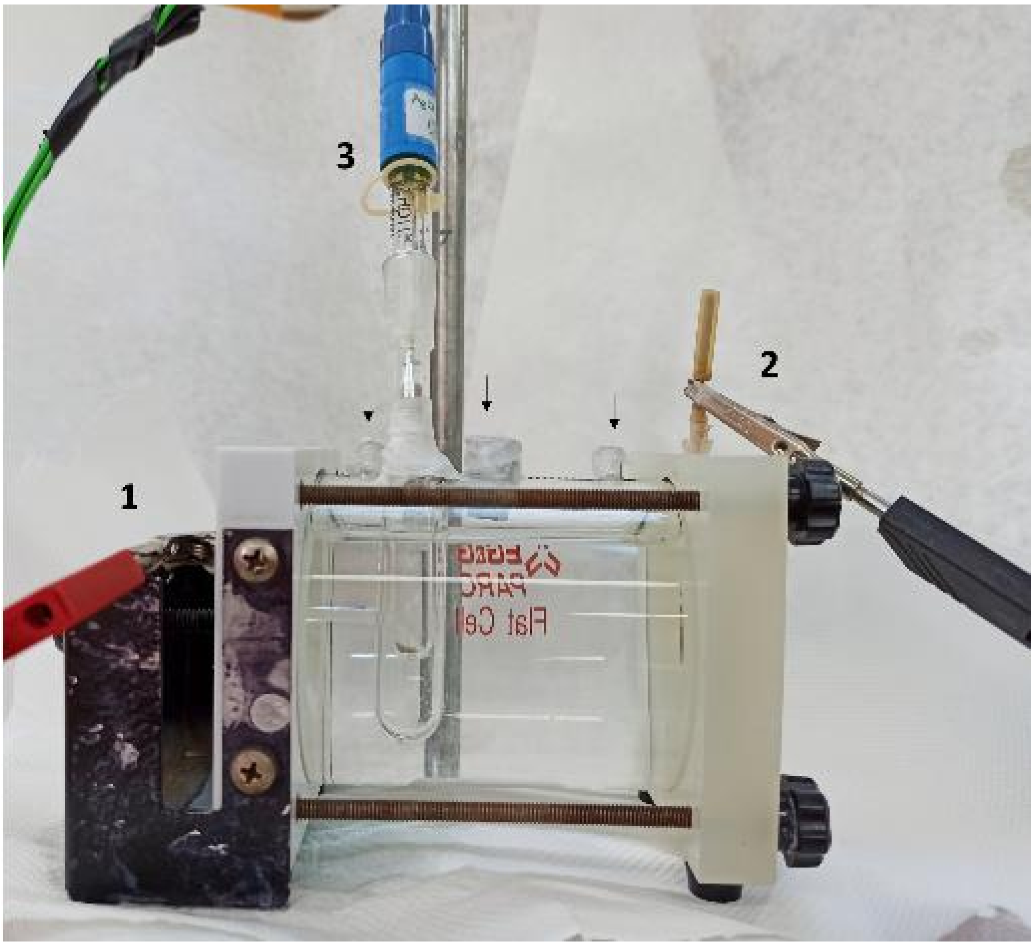

Figure 8: Half-Cell test configuration; (1) Working Electrode (Coated CC) (2) Counter Electrode (Platinum Mesh) (3) Reference Electrode (Ag/AgCl)

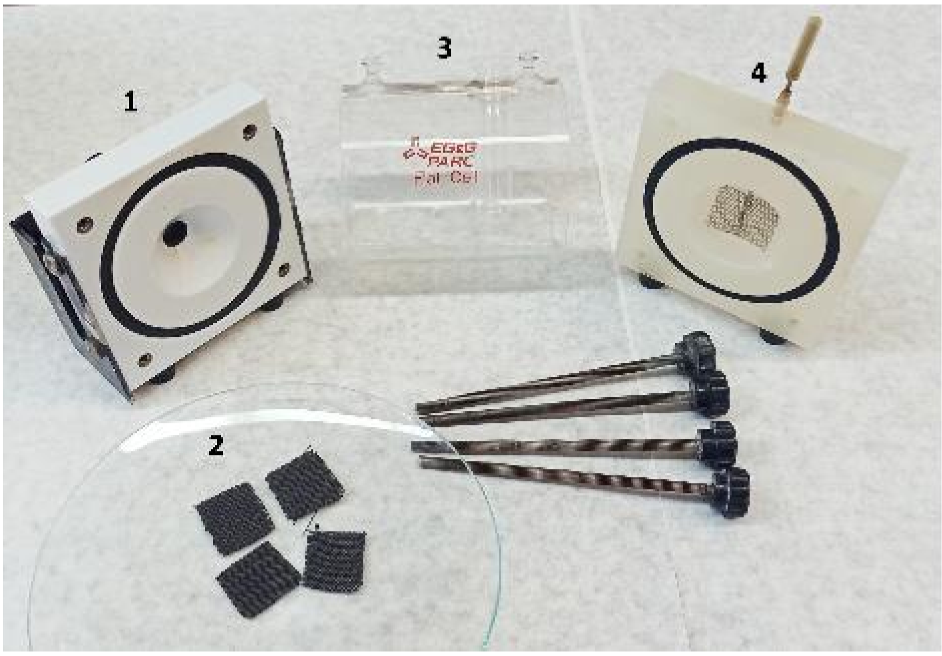

Figure 9: Assembling sequence of components in half-cell test configuration: (1) Cathode/WE matrix (2) Carbon cloth pieces (3) Electrolyte and reference electrode (RE) configuration (4) Platinum Counter Electrode

Full-Cell Tests Configuration (Battery Tests Setup)

A zinc plate and a piece of catalyst-coated gas diffusion layer (carbon paper) were positioned in the anode and cathode, respectively. The exposed surface of the electrodes to the electrolyte is 8.5 cm^{-2}. Two layers a microporous membrane (Celgard 3401) were used in both sides of the electrolyte as separators. A Nickel mesh was the current collector of the cathode and a Cu mesh the respective collector of the anode, while highest ionic conductivity was reached 6M KOH solution was used as an electrolyte. Both the Zinc – air cell and assembling sequence of components can be found in [Figure 10 and Figure 11]

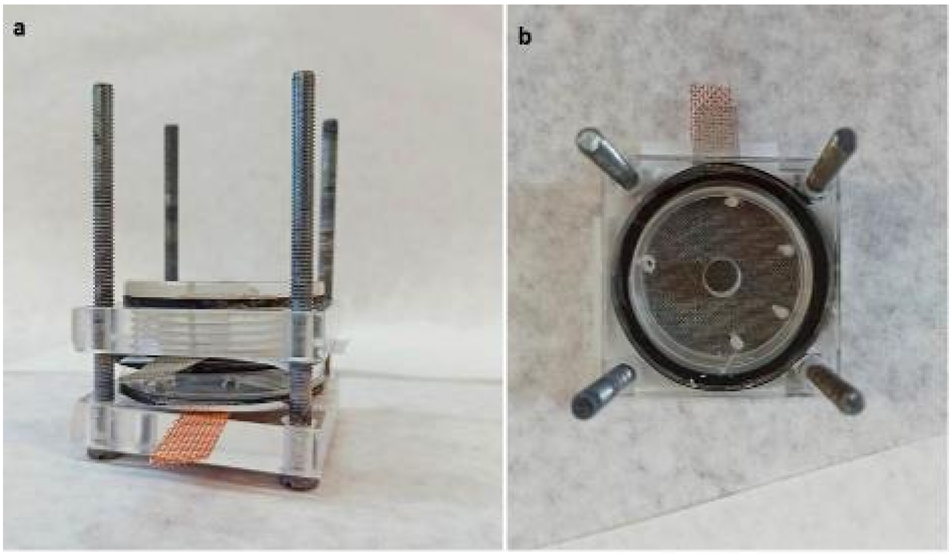

Figure 10: (a) Zinc- Air cell (b) Cathode oxygen entrance

Figure 11: Assembling sequence of components in zinc-air cell; (1) Cu Mesh/ Current Collector (2) Zinc polished plate / Anode (3),(5) Separator Membrane (4) Electrolyte entrance (6) Coated CP/ Cathode (7) Ni Mesh/ Current Collector

5. RESULTS

5.1 Half-Cell Tests – ORR/OER Evaluation

As aforementioned, each catalyst was separately evaluated towards its activity regarding facilitating Oxygen Reduction Reaction and Oxygen Evolution Reaction.

Cyclic Voltammetry was conducted to get a footprint of the activity of the catalyst in reductive potentials. As mentioned in the introduction, the desirable 4-electron pathway of ORR is expressed:

$$\mathrm{O_2 + 2H_2O + 4e^- \rightarrow\ 4OH^-\quad E^0 = 0.4\ V\ vs\ SHE} \tag{32}$$

In order to convert this standard value to Reversible Hydrogen Electrode potential, Nernst Equation (16) is used applying a pH value of 13 (0.1M KOH):

$$E_{\{RHE)} = E_{SHE} + 0.767 \tag{33}$$

In this way equation (30) can be written as:

$$\mathrm{O_2 + 2H_2O + 4e^- \rightarrow\ 4OH^-\quad E^0 = 1{,}167\ V\ vs\ RHE} \tag{34}$$

Thus, it is expected to observe a peak below 1,167 to get a first impression of the overpotential needed for ORR to occur, while based on previous works catalysts prepared exhibit an E_{onset} overpotential ranging from 200mV – 400mV. However, mass transport in stationary electrodes is governed by diffusion and ORR is a process highly depending on diffusion, so it is not possible to come to particular conclusions about ORR kinetics.

Firstly, clean carbon cloth was tested for comparison reasons, as found in *Figure 12*.

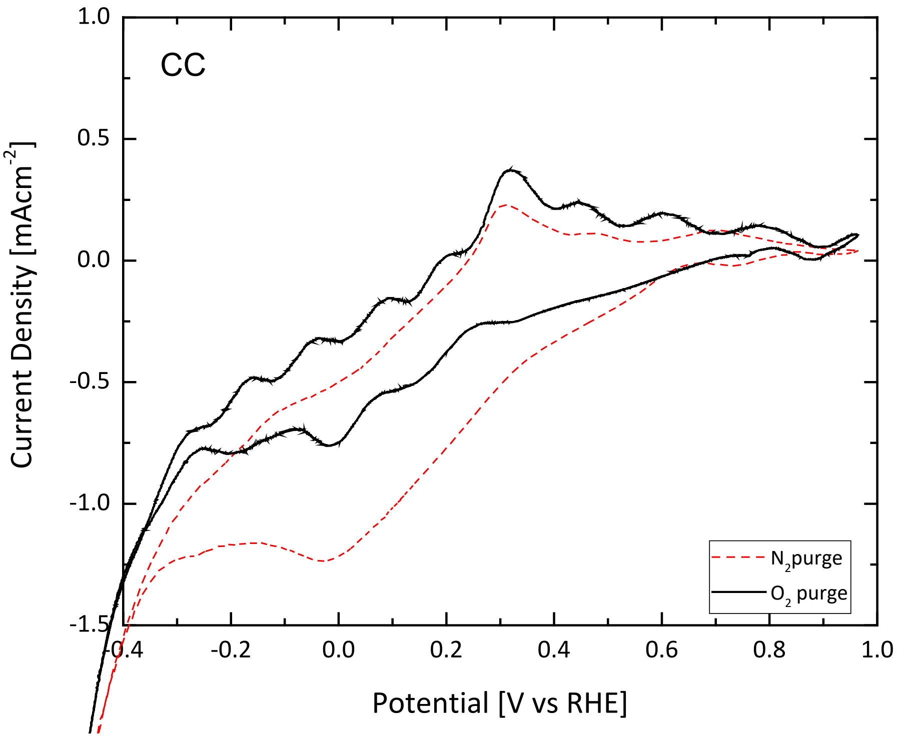

Figure 12 : ORR polarization curves of clean carbon cloth: N_2 Saturated and O_2 saturated

Correspondingly the same ORR polarization was conducted when PBC and PBCF catalyst was coated on carbon cloth. Below the results for N_2 and O_2 saturation can be found separately, as four experiments were conducted for each material. [*Figure 14* and *Figure 13*]:

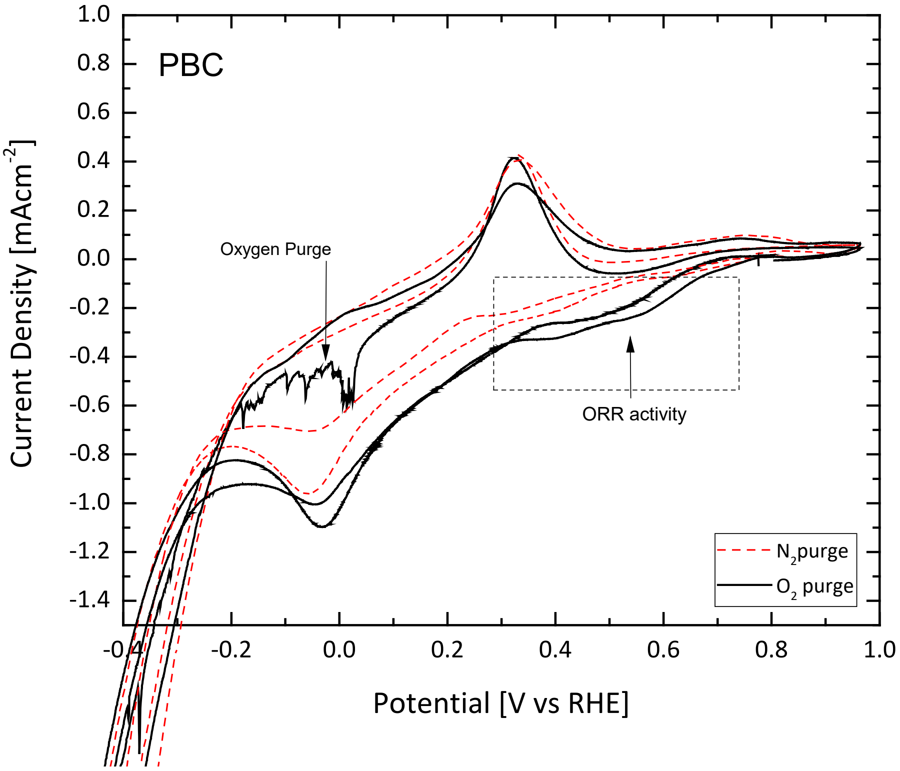

Figure 13 : ORR polarization of PBC catalyst on CC; N_2 Saturated and O_2 saturated

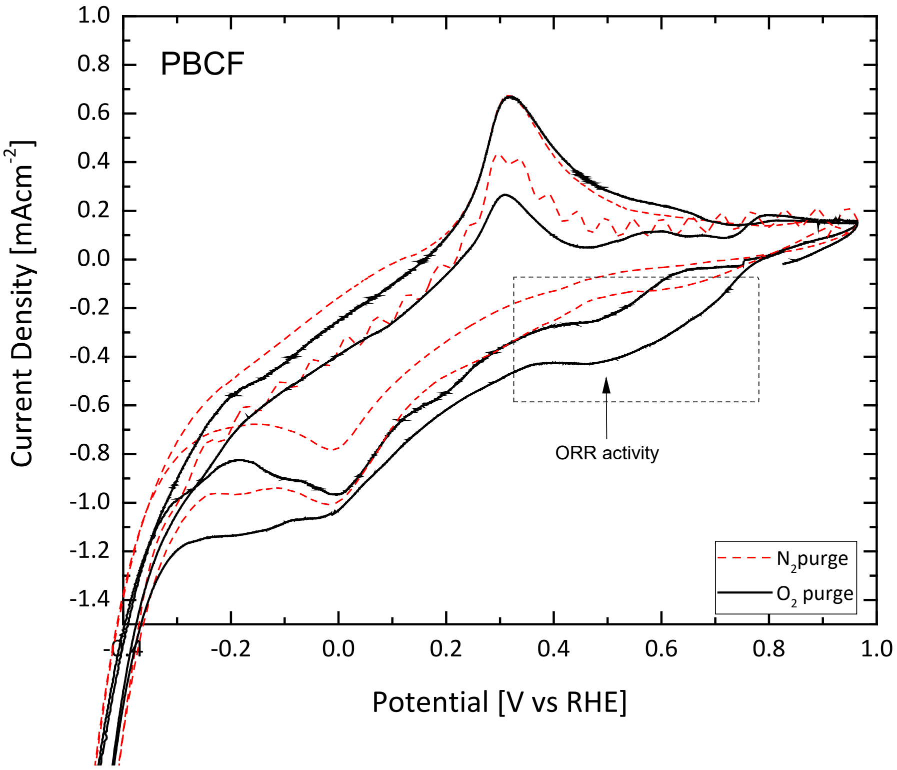

Figure 14 : ORR Polarization of PBCF catalyst coated on CC; N_2 Saturated and O_2 saturated

As predicted, clean CC does not exhibit any activity in the region of 4-electron transfer towards ORR, contrarily to PBC and PBCF. In *Figure 13* and *Figure 14* it is obvious that when oxygen purged, between a region of 0.6 - 0.8 V vs RHE during the cathodic scan, catalysts start to show an activity due to oxygen natural dissolution. Contrarily, in the same plots, when the electrolyte was N_2 saturated, the peaks are suppressed. This noticeable difference in the potential region of interest gives validation of the existence of ORR with an onset overpotential around 500 mV.

Furthermore, it appears that PBC and PBCF have very similar performance towards the facilitation of ORR, as the activity observed is found in the same potential region as seen in [Figure 15] where the performance of all samples in oxygen saturated electrolyte are depicted:

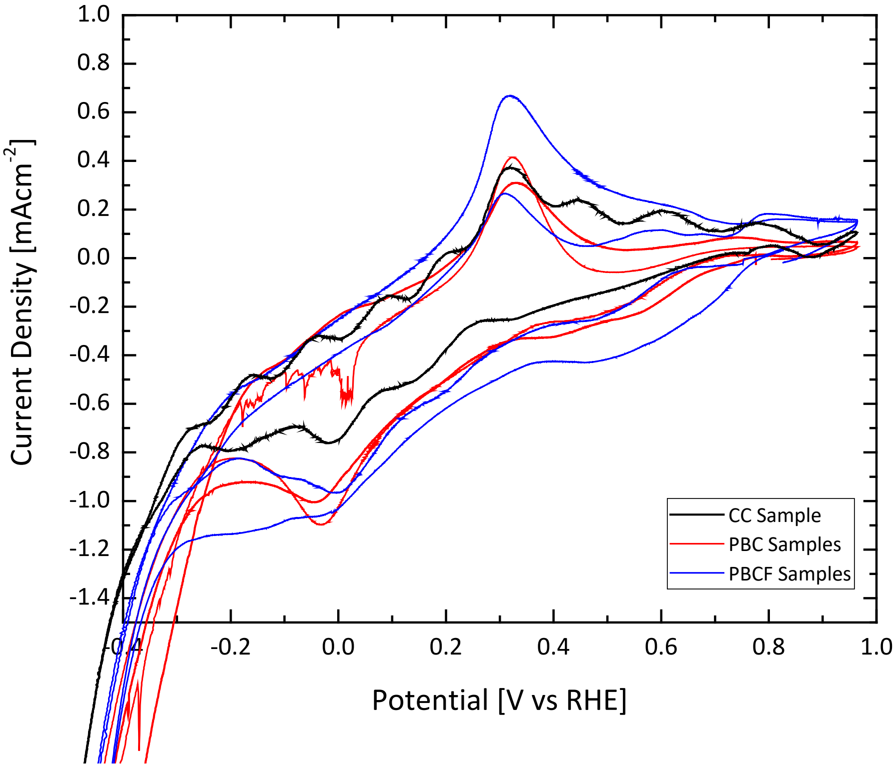

Figure 15: ORR Polarizations of CP/ PBCF and PBC

Besides the reduction of interest, the above plots reveal the presence of more redox species that during cathodic scan exhibit an activity around -0.05 V vs RHE and during anodic scan around 0.3 V vs RHE. These species are not dependent to the existence of a catalyst, as they arise also in CVs conducted with clean CC.

Taking into consideration the plot of clean CC, it is assumed that the molecules reduced and oxidized are derived either from CC or the existence of active species inside the electrolyte. A possible explanation would be that the cathodic peak observed derives from the beginning of water splitting. The cathodic reaction of water splitting is the following:

$$2H_2\mathrm{O} + 2e^- \leftrightarrow H_2(\mathrm{g}) + OH^- \ \mathrm{E}^0 = -0.827 \text{ V vs SHE or } \mathrm{E}^0 = -0.06 \text{ V vs RHE} \tag{35}$$

Another possible explanation would be the formation of Hydrogen Peroxide radicals (H_2O_2 intermediates) through the 2-electron reduction of existing oxygen molecules of the surface of carbon cloth. The main implication for this assumption is that literature states that carbon surfaces usually promote undesirable 2-electron transfer in ORR [143-145].

$$O_2 + H_2O + 2e^- \leftrightarrow HO_2^- + OH^- \quad E^0 = -0.076\, V\, vs\, SHE\, or\, E^0 = 0{,}691\, V\, vs\, RHE \tag{36}$$

However, the decomposition of hydrogen peroxide cannot be responsible for the anodic peak at 0.3 V. The anodic peak can be attributed to possible slight oxidation of the carbon surface of carbon cloth.

Continuing with the Oxygen Evolution Reaction investigation, LSV was conducted towards oxidizing potentials for each catalyst. In contrast with ORR, OER in this system is not limited by diffusion, as OH^- anions are abundant inside the electrolyte and can easily access the TPBs. Considering this, it is acceptable to come to some conclusions regarding kinetics of the reaction on each catalyst. In order to make precise calculations of current responses to applied potentials, it was beneficial to calculate IR drop in each half-cell setup, as explained in the experimental section.

After having explained this, the PEIS spectra and OER polarization curves for CC alone and for CC coated with each catalyst can be presented.

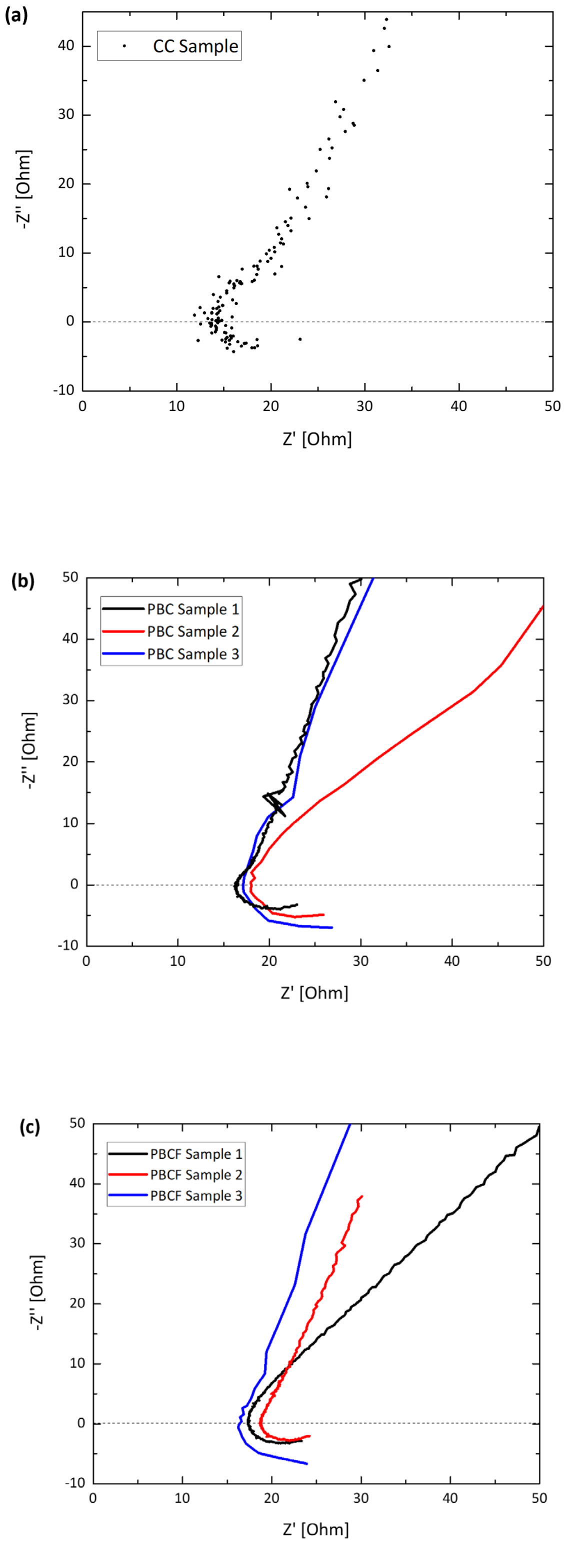

Figure 16: EIS spectra of (a) CC (b) PBC (c) PBCF in 0.1 M KOH solution

EIS spectra was obtained from 1MHz – 1 Hz, although no semicircles were observed, as the data formed an ascending line representing the impedance driven from mass diffusion. Thus, the diagrams presented are focused on the high frequencies area where the RHF can be distinguished. As expected, due to same three-electrode configuration and electrolyte concentration, there is a similarity between the values of solution impedance in each experiment, while these values are in an acceptable range, confirming sufficient connection between the cell components.

From the above results, the appropriate maximum frequency that RHF could be detected, was measured and through "IR Compensation-ZIR" technique in EC-Lab each solution resistance was precisely calculated.

Catalyst	**RHF (Ohm)**
Carbon Cloth (Blank)	15.441043
PBC Sample 1	16.383505
PBC Sample 2	15.25474
PBC Sample 3	14.64411
PBCF Sample 1	17.366667
PBCF Sample 2	18.775368
PBCF Sample 3	13.97425

In *Figure 17*, OER Polarization curves are presented, where potentials are IR compensated:

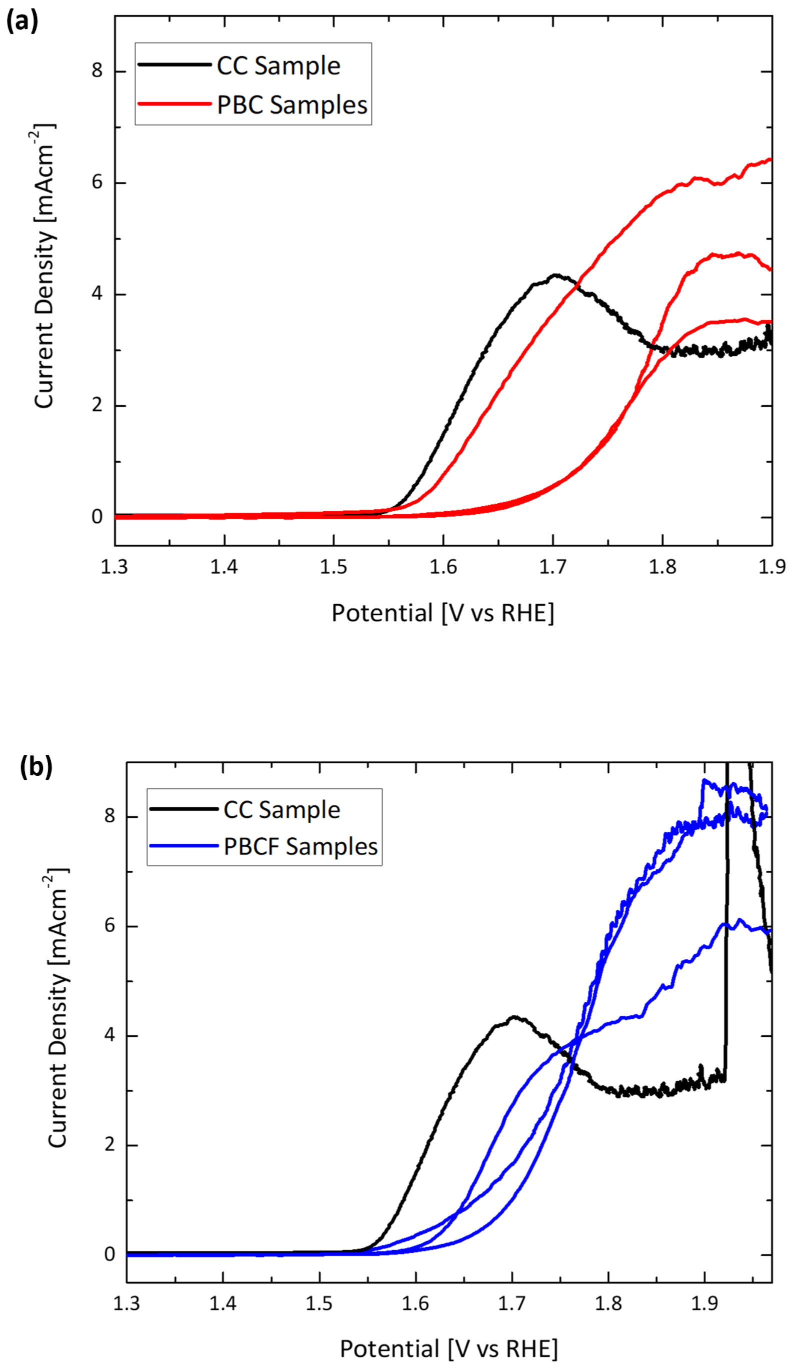

Figure 17: OER polarization Curves (a) PBC and (b) PBCF compared to OER Polarization of CC in 0.1 M KOH solution

The existence of evolution of oxygen is verified, while all catalysts exhibit an onset potential E_{onset} above 1.5V, in other words they have an activation overpotential higher than 300mV. Ideally, catalysts are expected to reach a current density above 10mAcm^{-2} in order to present comparable overpotential metrics with current reports. However, the overpotential needed to reach a current density of 4 mAcm^{-2} can be compared between the catalysts as seen in *Figure 18*. For carbon cloth there will be no quantitative characterization, as the OER polarization reveals a performance that cannot be assumed as near steady-state. Moreover, for PBC sample 3 the overpotential to reach 3.5 mAcm^{-2} is presented.

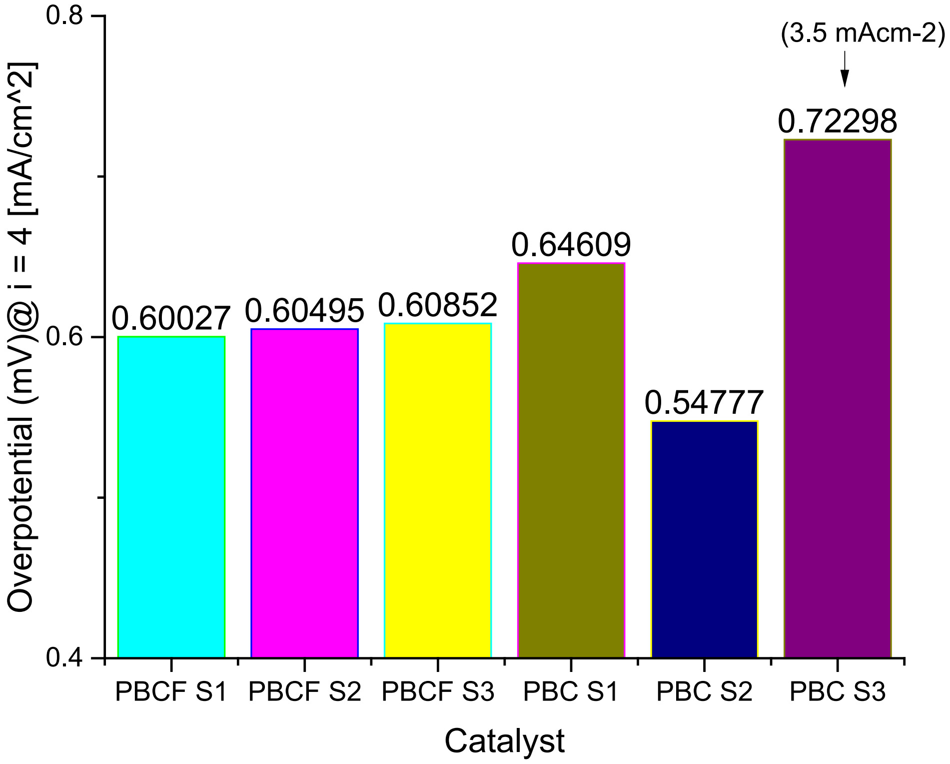

Figure 18: Overpotential of PBC and PBCF samples at a current density of 4mAcm^{-2}

Tafel plots (V-logi) were constructed in order to define the linear area of the diagram which obeys in the Tafel equation and determine the Tafel slope b for each catalyst. The kinetically controlled region of each catalyst and Tafel Slopes are presented in *Figure 19*.

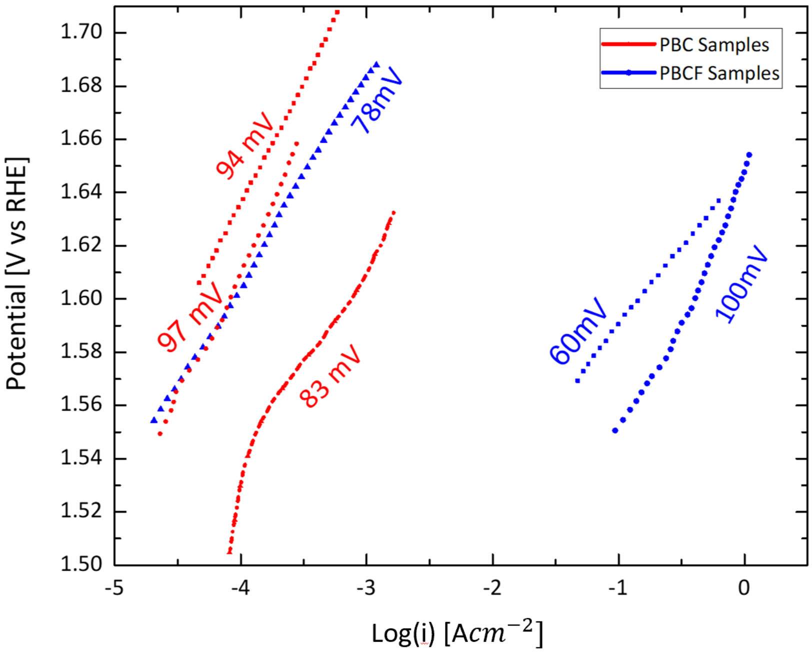

Figure 19: Tafel Plots of PBC and PBCF determined from the linear area in voltammetry responses

The overall results signify that PBCF exhibits better OER properties than PBC. Firstly, in Figure 17 it is apparent that the three samples of PBCF have similar activation potentials (~1.55V), implying reliable OER results, that are closer to standard potential of OER/ORR compared to (1.55-1.65 V) PBC. Furthermore, the plots of PBCF reach higher current densities than the plots of PBC, while it is observable that the current rise of PBCF is steeper. The steep current rise is illustrated also in Tafel plots, where Tafel slopes of PBCF are found relatively lower.

After these evaluations, Cyclic Voltammetry was conducted to give an overall image of the reactions occurring in oxidizing and reductive potentials. Each catalyst was firstly cycled 4 times to become electrochemically stabilized. In Figure 20 and Figure 21 the continuous CVs of two prepared samples of PBC and PBCF electrodes are available:

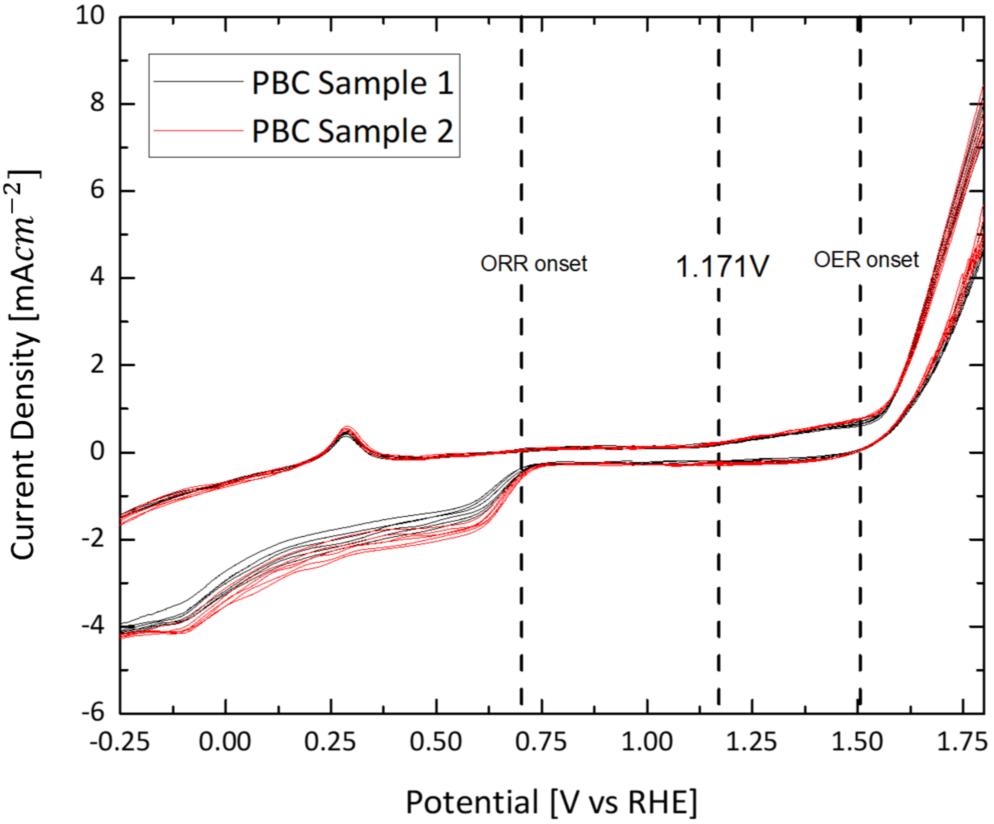

Figure 20: CV profiles of PBC catalyst recorded in 0.1 M KOH solution (a) Sample 1 (b) Sample 2

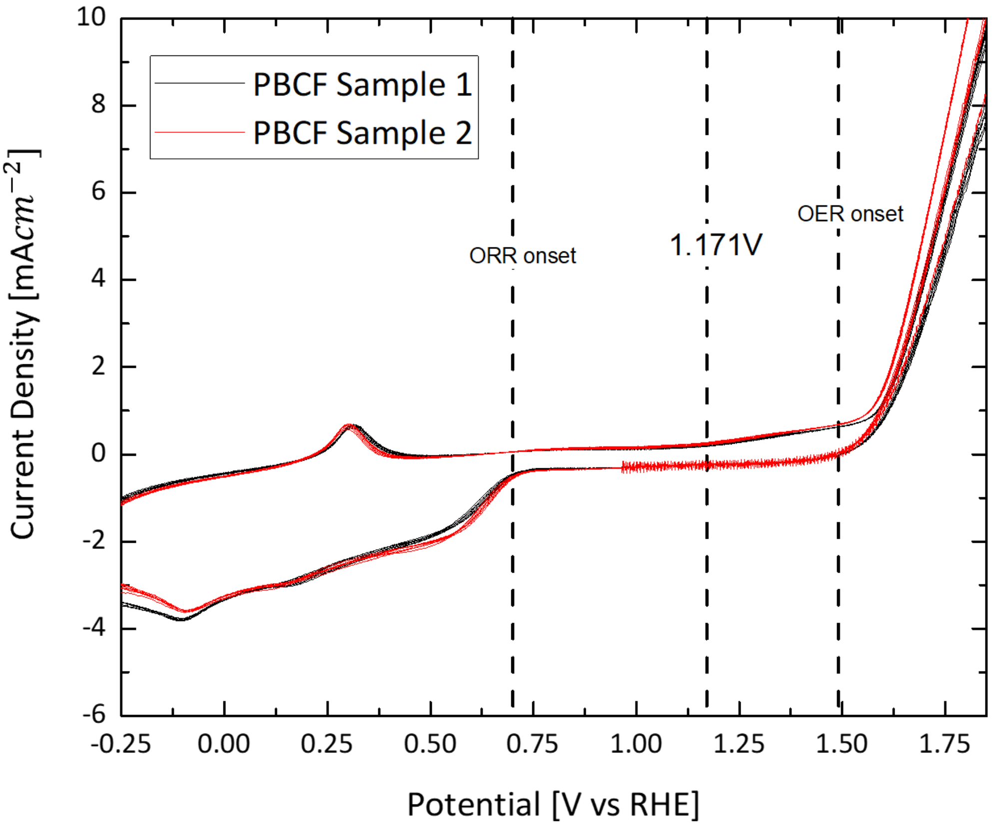

Figure 21: CV profiles of PBCF catalyst recorded in 0.1 M KOH solution (a) Sample 1 (b) Sample 2

The two samples of PBC and the two samples of PBCF exhibit reproducible behavior in reductive and oxidizing polarizations while the CV plots maintain the same shape throughout all cycles, indicating stable ORR/OER activity. From the figures it is apparent that reactions occur far from the equilibrium, specifically ORR overpotential appears more extended, probably due to diffusion limitations.

In the following diagram the 10th cycle of each catalyst is provided for comparison reasons:

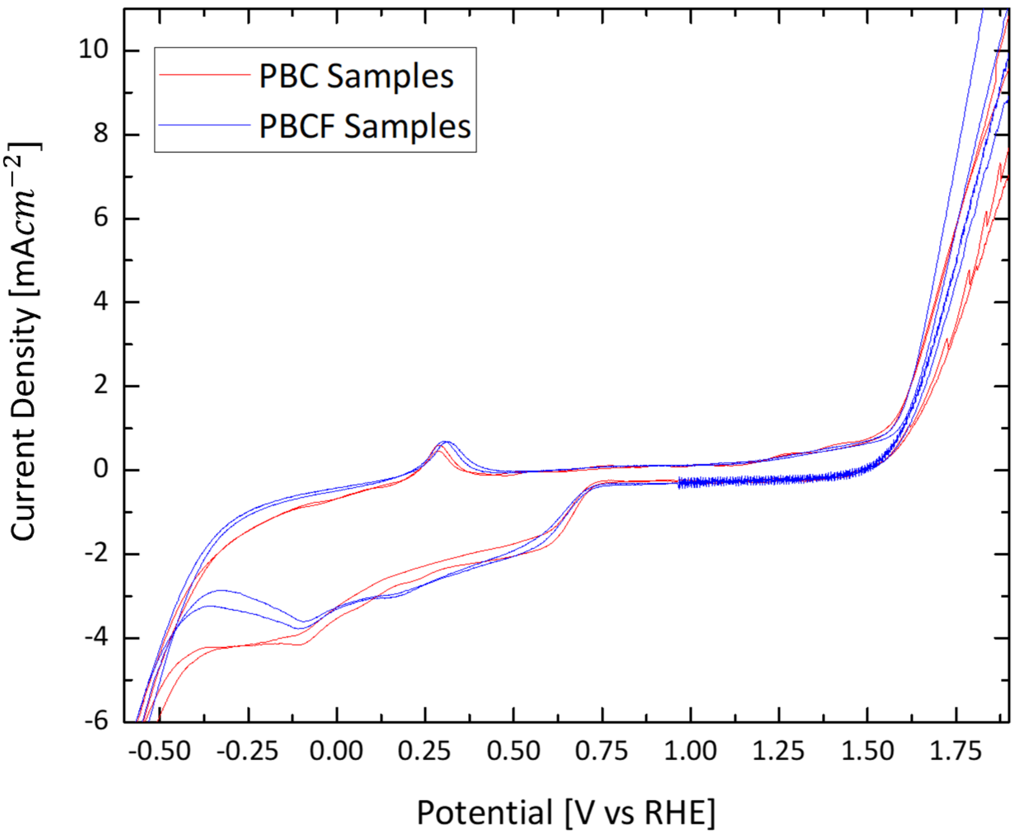

Figure 22: 10th cyclic voltammogram of PBC and PBCF samples in 0.1 M KOH solution

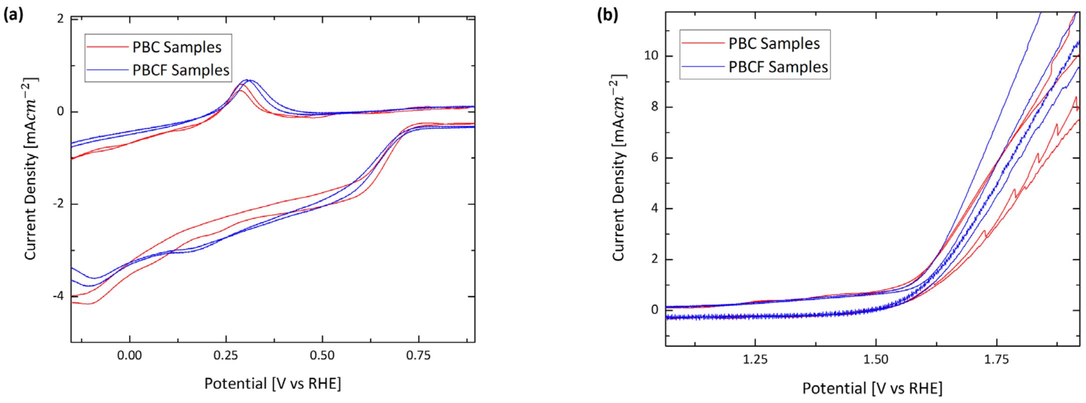

Figure 23: (a) Reduction region of PBC and PBCF (b) Oxidation Region of PBC and PBCF

From the above Figures it can be derived that ORR activity of the two catalysts seems almost identical while PBCF shows slightly more sharp activation towards OER.

5.2 Full-Cell tests – Battery Performance

Each catalyst was applied in the Zinc- Air cell as presented in *Figure 10* and then tested with the procedure described in 4.1.2.

When each ZAB was assembled, the Open Circuit Voltage was recorder for 1h until it was stabilized. The recorded data for Clean CP, PBC and PBCF coated CP can be found in *Figure 24*.

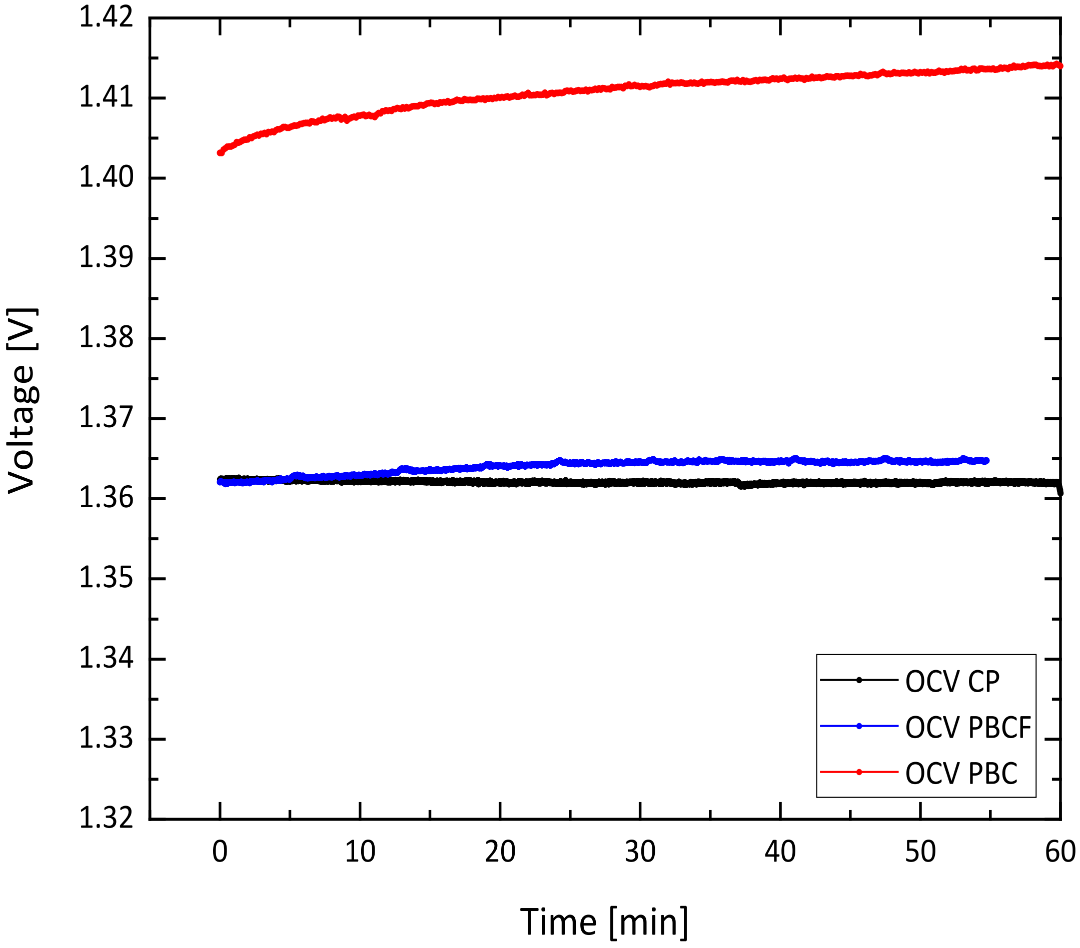

Figure 24: OCV recorded data for (a) CP (b) PBCF coated CP (c) PBC coated CP

Afterwards, PEIS spectra was obtained in order to get a first idea of the connections and impedance sources inside the cell system, before any redox reactions occur, as seen in Figure 25.

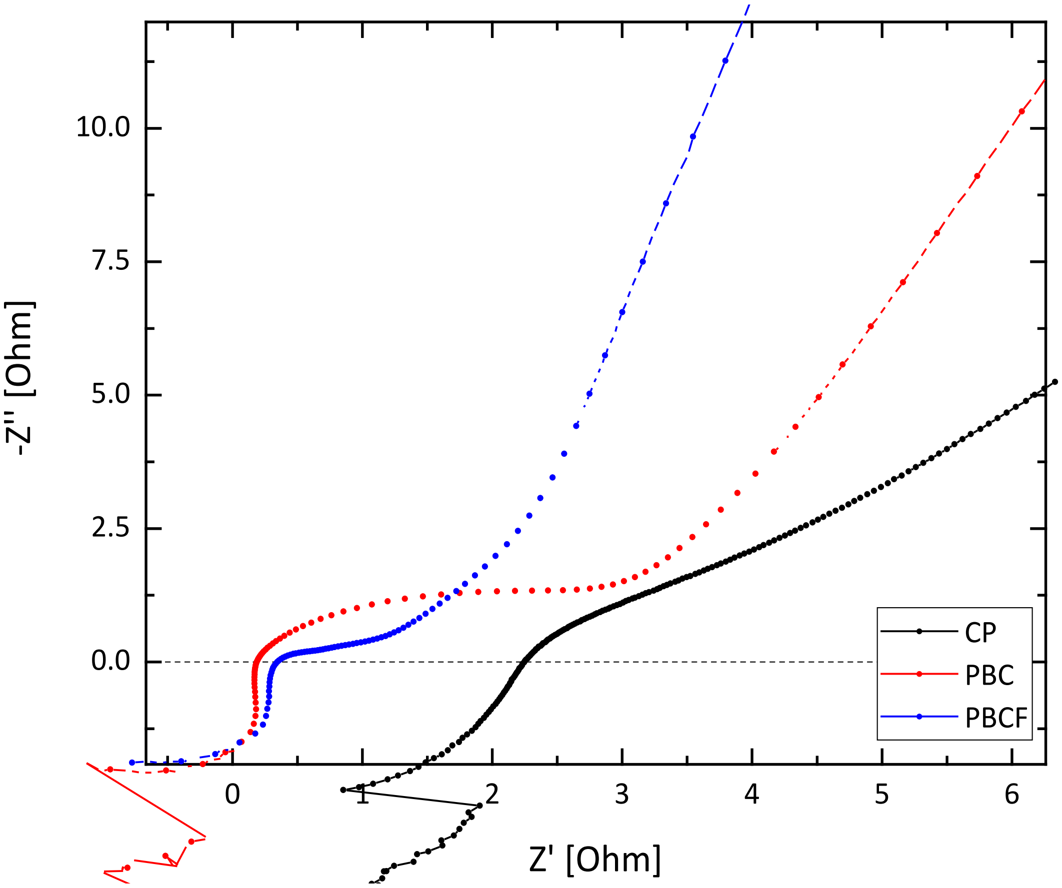

Figure 25: EIS spectra of each cathode before battery testing

Sufficient connection between the components of the battery cell was verified, as all OCV values approach while the theoretical voltage of 1.65 V and the resistance of the electrolyte (RHF) has a negligible height.

After subjecting the battery to an activation process by simply discharging and charging at a very low rate (0.5- 10mA) for 2 hours, the cell was tested as a primary battery at first.

Galvanodynamic polarization curves of each primary battery cell are presented in Figure 26.

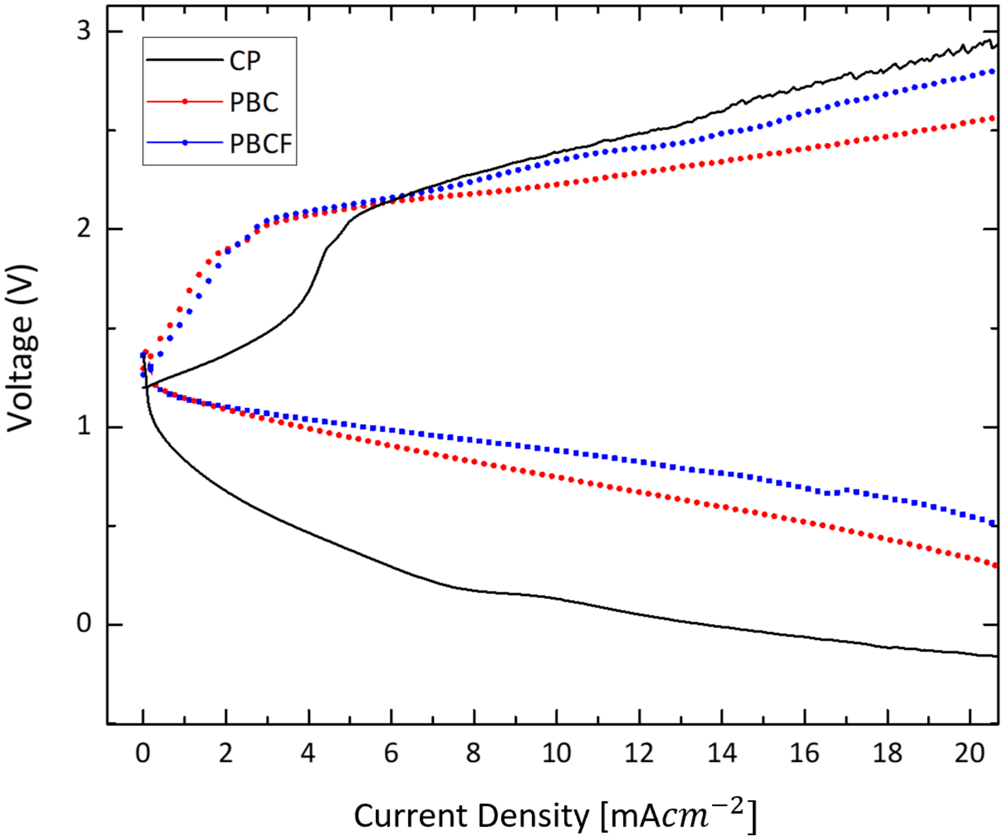

Figure 26: Polarization Curves of Zinc-Air cells with (a) CP (b) PBCF coated CP and (c) PBC coated CP cathodes

Furthermore, Power Densities were calculated, and the corresponding Discharge Polarization/ Power plots were constructed in order to detect the Peak Power Density of each cell as shown in Figure 27.

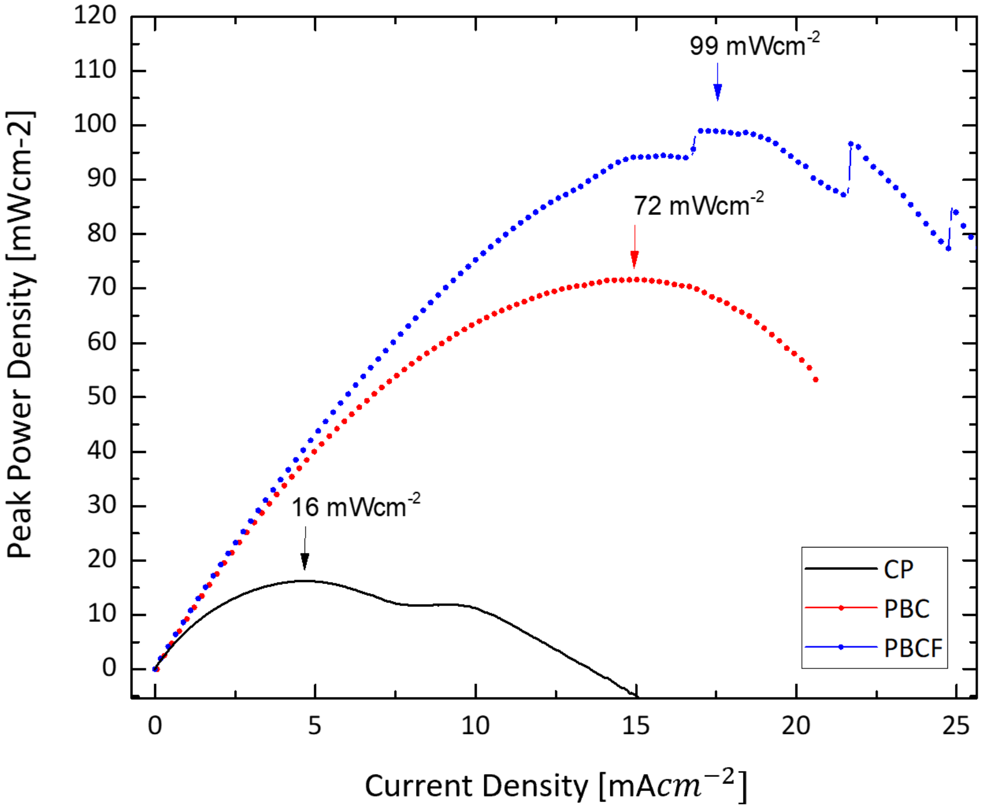

Figure 27: Power density curves of primary Zn–air batteries with (a) CP (b)PBCF coated CP and (c) PBC coated CP cathodes

Polarization Curves reveal valuable information about the catalysts. Clean CP, as expected is polarized considerably more than the catalyst coated CP samples. Particularly when discharging the voltage drops below 1V at 1 mAcm^{-2}, which means the cell with a CP cathode when discharged with a current density 1 mAcm^{-2} cannot supply energy with more than 1V.

The two catalysts proved to facilitate both ORR and OER as the departure from OCV in both reactions is limited compared to tested CP, especially when discharging and in higher currents, while the voltage gap is increasing in an acceptable form as ohmic resistances are growing. PBC and PBCF exhibit in general similar properties. Regarding ORR the activation losses are present in a limited region, while ohmic losses are governing the departure from OCV. Contrarily, in oxidizing currents the activation losses, which result from the catalysts' electrochemical properties, possess a more extended region.

Until polarizing at 7 mAcm^{-2} PBCF exhibits slighter better performance, maintaining decreased voltage gap and better ORR properties. When applying higher current densities, the voltage gap of charging and discharging polarization curves is almost identical for the two catalysts, although PBC exhibits slightly lower polarization when charging and PBCF when discharging.

The above observations are validated furthermore by the Power Density Plots where it is apparent that PBCF can attain higher current rates with lower voltage losses and the corresponding cell can supply a decent Peak Power Density of 99 mWcm^{-2}.

Following the current scan, a voltage profile of each cell was obtained [*Figure 28*], by discharging the cell in ascending current values for a short period of time (5-10min):

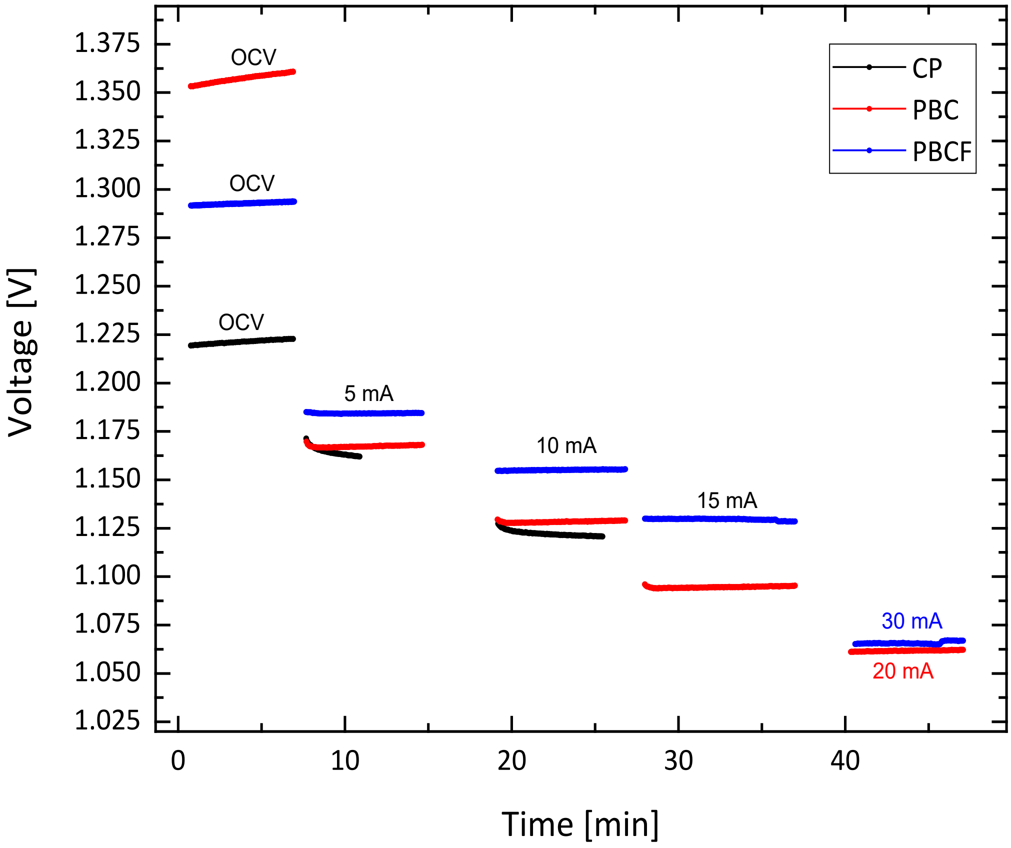

Figure 28: Voltage Profile of Zn-Air Batteries CP(black), PBC coated CP(red) and PBCF coated CP cathodes(blue)

The conclusions derived from galvanodynamic polarization are verified also by the discharge voltage profiles of PBC and PBCF. PBCF appears to prevent more successfully severe voltage losses showing enhanced ORR features.

The above Voltage Profile is highly useful, not only to compare voltage losses among the catalysts, but mostly to decide the discharge current to be used for the battery capacity determination.

Having explained the conditions affecting the capacity performance of the cell, it is significant to determine the appropriate discharge current before moving to determining the capacity. The first requirement, as there is no specific protocol for ZABs' testing, is that the data obtained can be comparable to other recent researches. Literature review reveals that most bifunctional catalysts are tested at 5 or 10 $mAcm^{-2}$. However, it should be considered that in order for the results to be meaningful the discharging current should have a value allowing the ZAB to supply a voltage above 1V, otherwise there is limited potential for future use of the results in real applications. In this context, it was decided to fully discharge the PBCF battery at 30mA and the PBC battery at 20mA.

Furthermore, when fully discharging a cell, it was decided to stop the discharging of the cell at a cut-off voltage of 0.8 V in order to prevent possible degradation of any component of the cell.

The voltage profiles and specific capacities of the two catalysts are available in Figure 29.

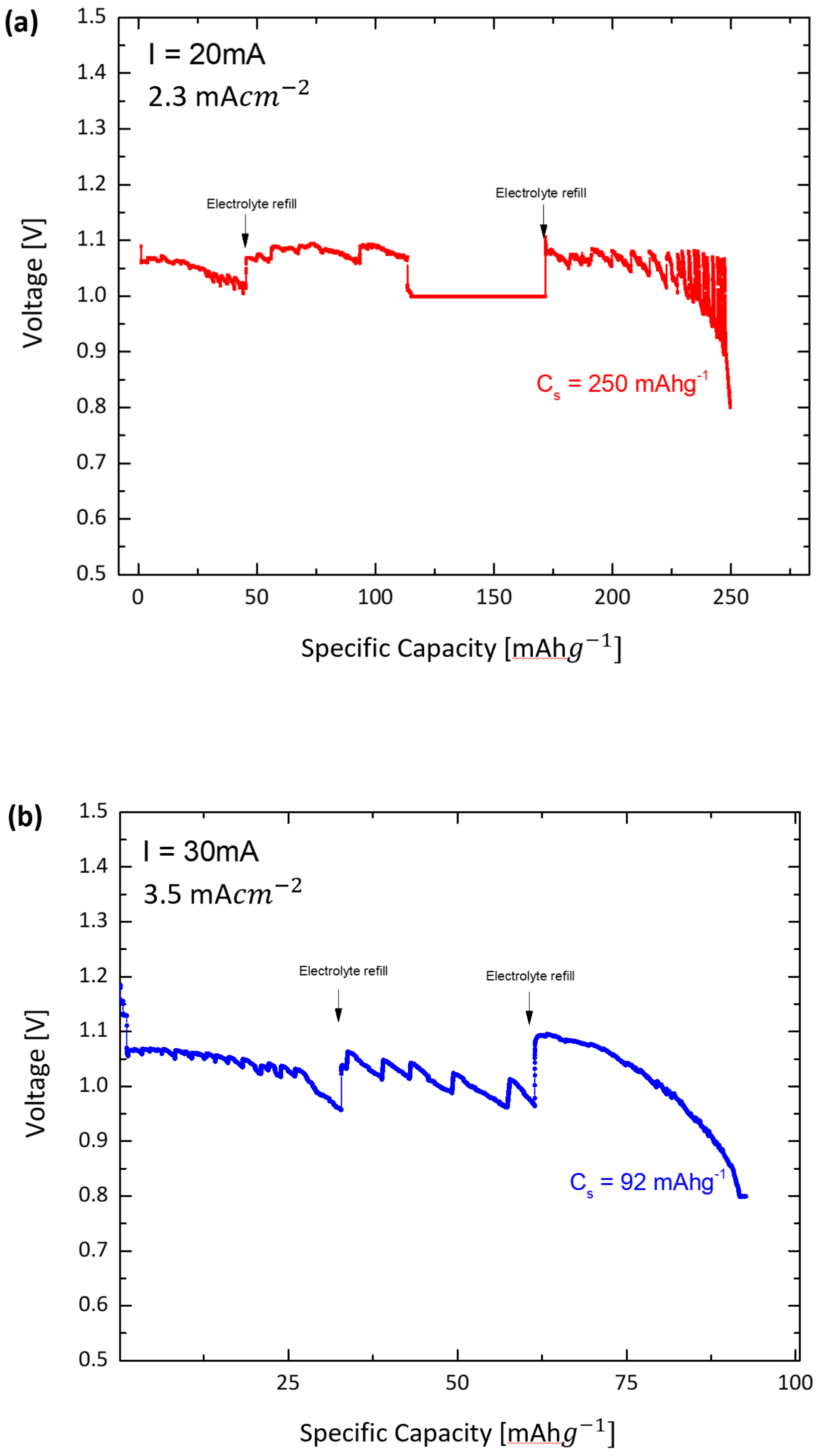

Figure 29: Discharge Voltage Profiles and Capacity Determination of Zinc-Air Cell with (a) PBC and (b) PBCF coated CP

From the above diagrams it can be driven that the Working Voltage of both cell containing PBC and PCF catalysts is around 1.05 V, implying better performance of PBCF that could supply the same voltage at a more challenging current rate. Nevertheless, PBCF delivered a severely reduced Specific Capacity of 92 $mAhg^{-1}$ that corresponds only to 10% of the theoretical specific capacity of a zinc electrode. As it will be figured in the following investigation of the batteries, the higher capacity supplied by PBC is not due to better features of the catalysts, but because of severe overpotentials developed in PBCF battery because of high demanded current supply.

After testing the Zinc- Air cell as a primary battery, rechargeability tests were conducted. Firstly, the batteries were charged until around 50% Depth of Charge with a lower rate of 15 mA in order to avoid as much as possible dendrite formation in the anode or cathode corrosion. The charge of the batteries is conducted firstly in order to define the voltage profile of charging and most importantly so as to have representative data recorder when conducting the continuous cycling afterwards. To illustrate this, the cycling profile of an empty battery is totally different from the cycling profile of a fully charged battery, consequently it was decided that the galvanostatic cycling tests will be conducted while the battery is at 50% State of Charge.

The voltage profiles when charging with a constant current are available in *Figure 30*.

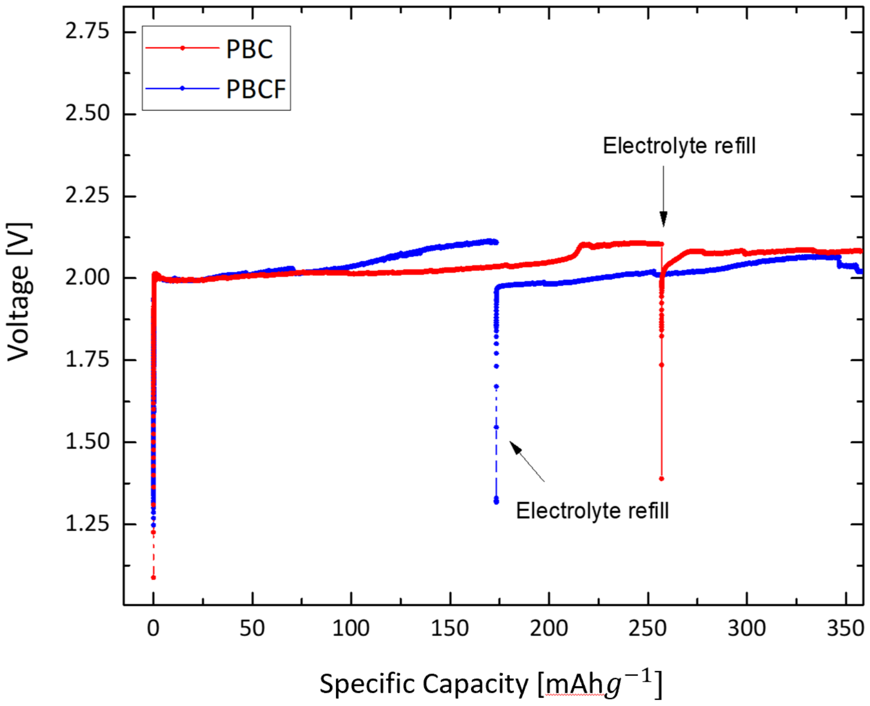

Figure 30: Charge Voltage Profiles of Zinc- Air Cell with (a) PBCF and (b) PBC coated CP

The prominent OER durability of PBCF comparing to PBC is verified also by the charging profile of the two catalysts. Besides the fact that, when being charged 100 mAhg^{-1}, the PBCF battery is starting to be polarized higher than 2V , it appears that it was due to loss of the electrolyte (through evaporation and leakage), because as soon as the electrolyte was refilled the battery preserved a voltage lower than 2V.

Cycling stability of catalysts was tested throughout continuous galvanostatic cycles (10 min charging / 10 in discharging). Clean CP when applied as cathode material was also cycled for less cycles and different current densities, for comparison reasons.

The corresponding charge and discharge cycling curves of the rechargeable Zn–air batteries are available in the following Figures.

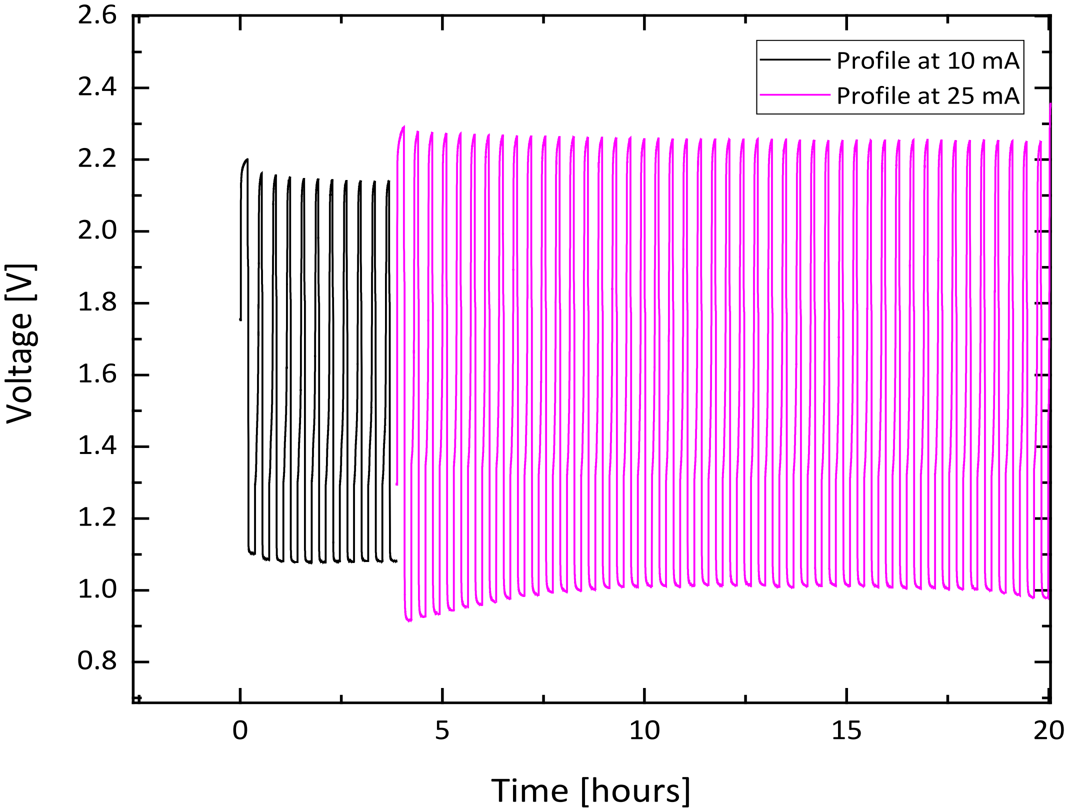

Figure 31: Galvanostatic discharge-charge cycling test of a Zinc-Air cell with a clean CP cathode.

The CP used (GDL) is reinforced with intrinsic electronic conductivity and two separate layers (microporous and microporous), consequently when no catalyst is coated, the transport of oxygen towards TPBs is very easy, leading to seemingly good ORR activity. However this limited polarization when discharging is due to limited polarization and degradation of CP from previous tests, as the CP Battery was not fully discharged or charged.

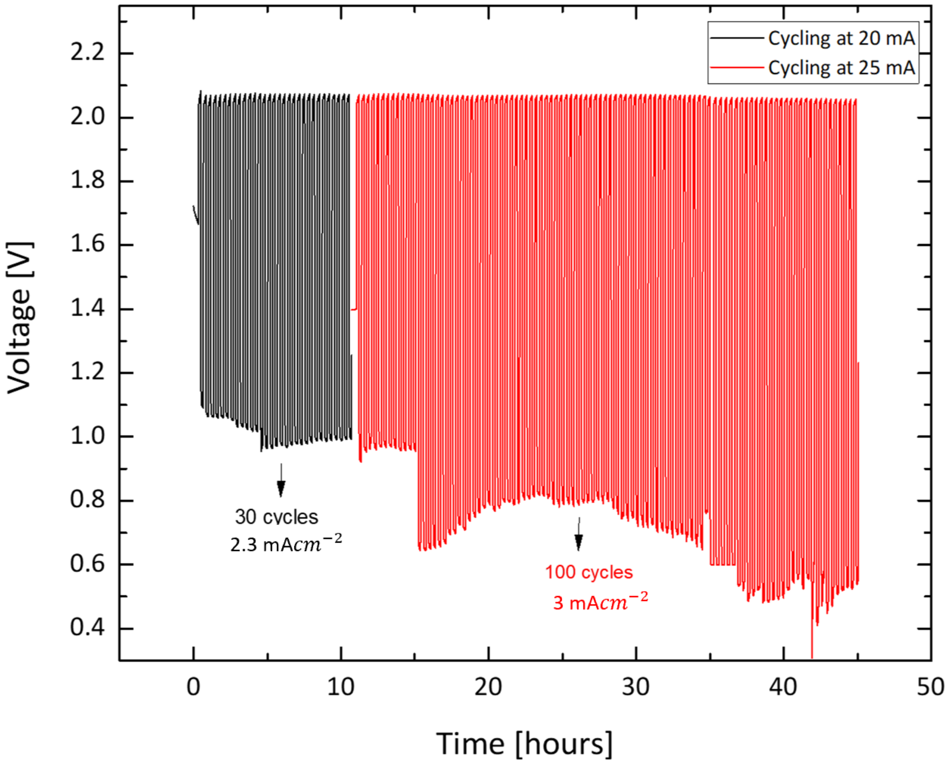

Figure 32: Galvanostatic discharge-charge cycling test of a Zinc-Air cell with a PBC coated CP cathode

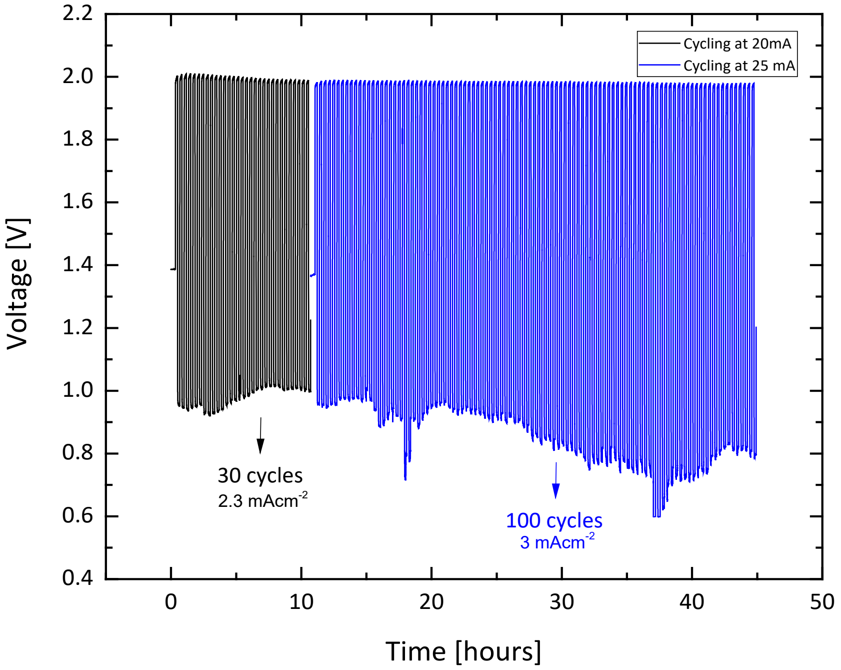

Figure 33: Galvanostatic discharge-charge cycling test of a Zinc-Air cell with a PBCF coated CP cathode

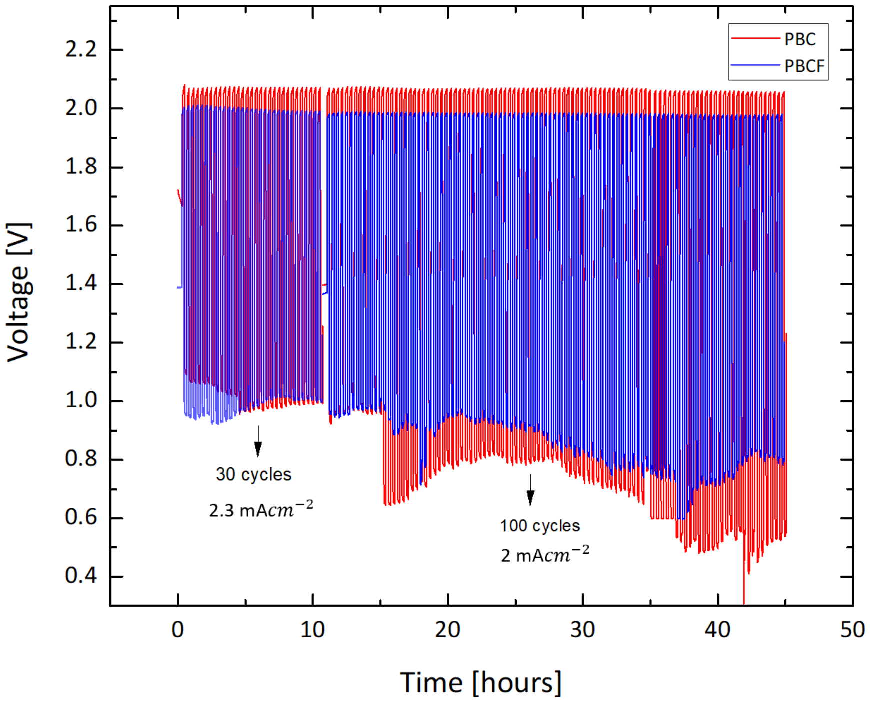

Figure 34: Galvanostatic discharge-charge cycling test of a Zinc-Air cell with a (a) PBCF coated CP cathode

The final galvanostatic charge-discharge cycles validate the bifunctionality towards ORR/OER of both catalysts when applied in a ZAB system. The outcomes of previous electrochemical and battery tests implying better catalytic activity of PBCF are confirmed by the prominent Voltage Profile of the catalyst when cycled.

To illustrate better the differences in developed Voltage Gaps between charge and discharge processes throughout the cycles, in *Figure 35* the voltage profiles at 10, 30 and 40 hours of cycling can be found.

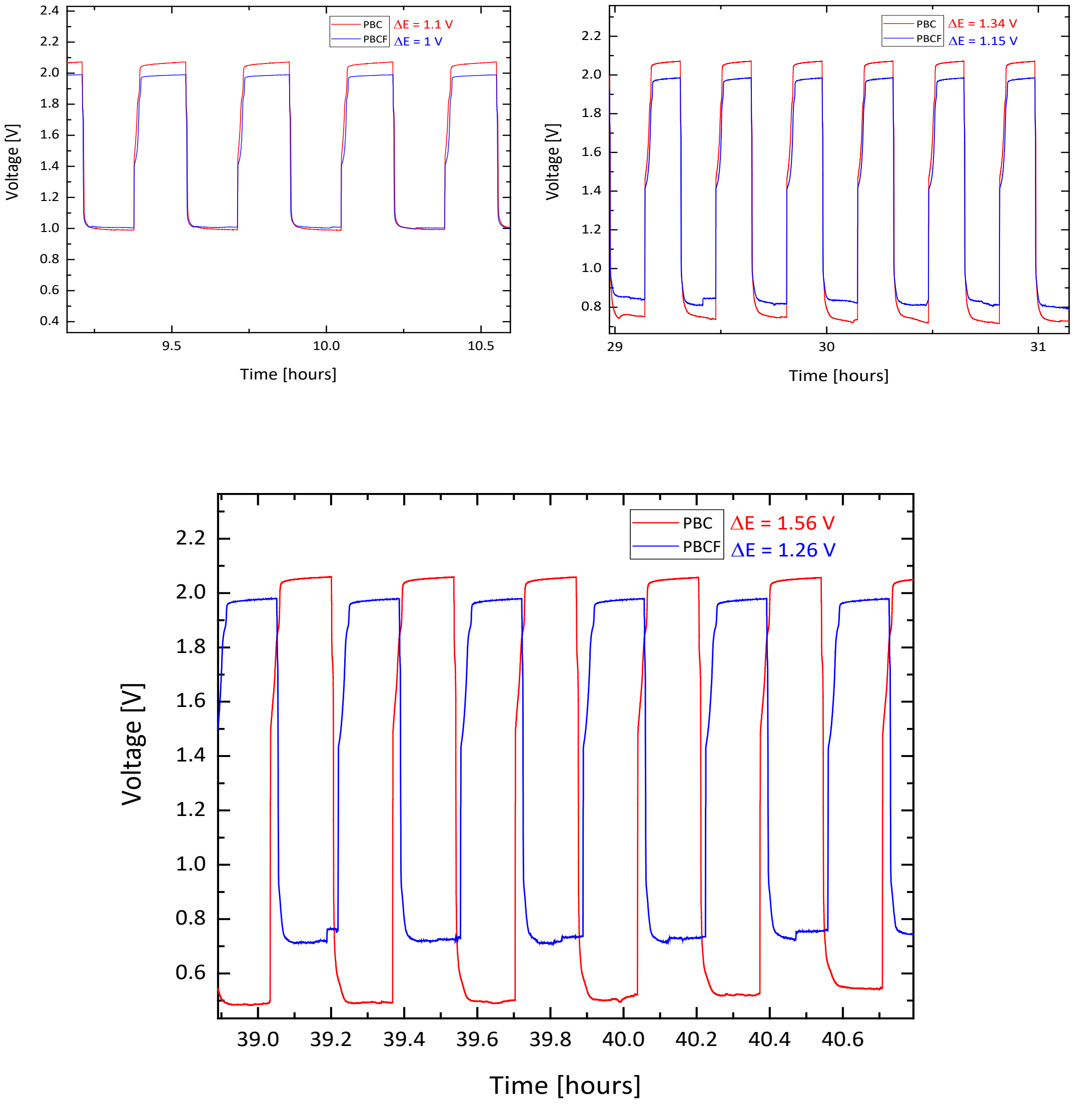

Figure 35: Voltage Gaps of PBC and PBCF catalysts at (a) 10 hours (b) 30 hours and (c) 40 hours of continuous galvanostatic cycling

Finally, EIS spectra was obtained before and after each electrochemical testing stage as seen in *Figure 36* and *Figure 37* :

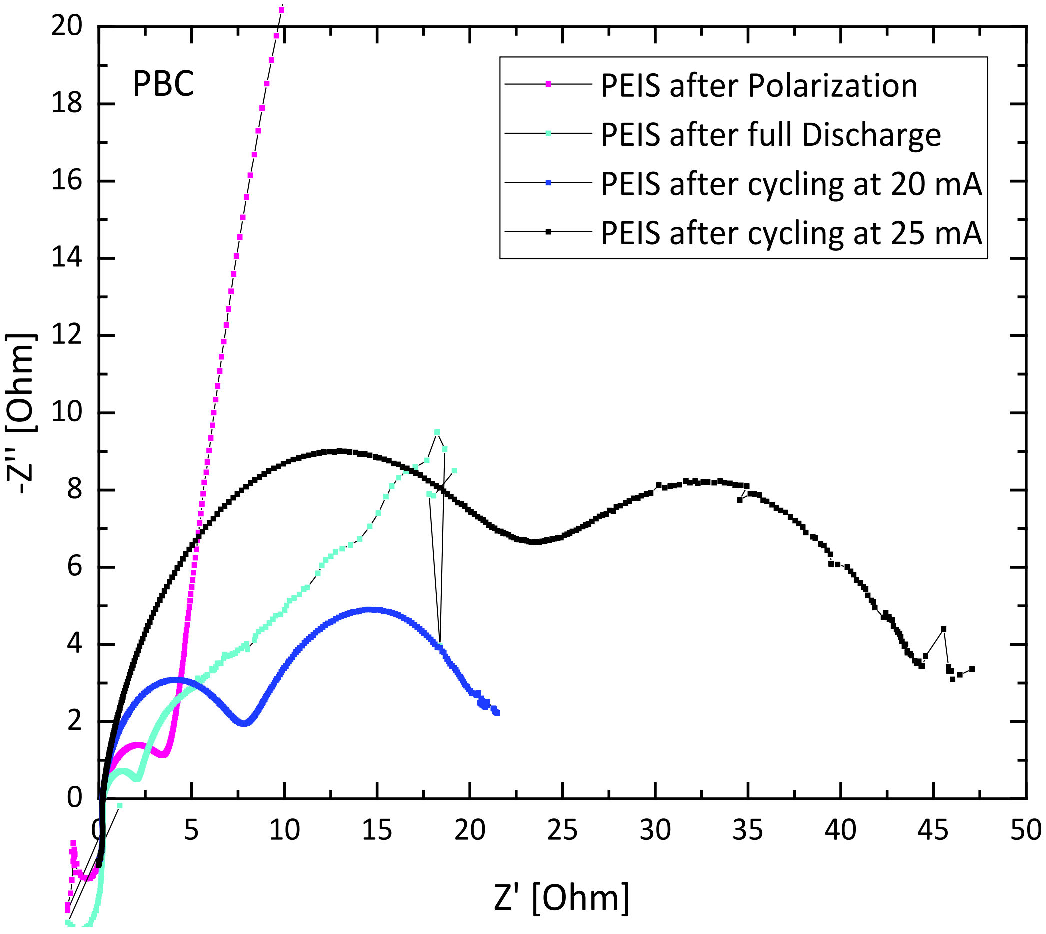

Figure 36 : EIS spectra of the battery with the PBC coated cathode

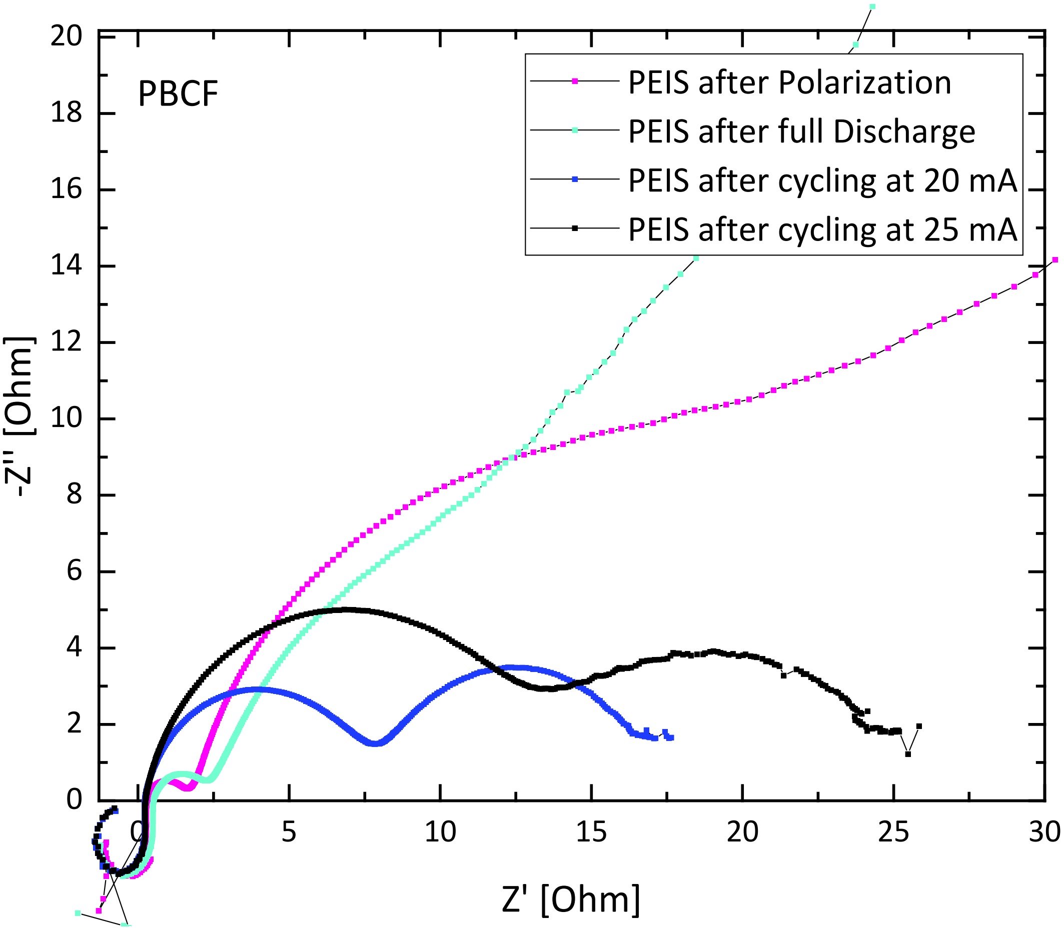

Figure 37 : EIS spectra of the battery with the PBCF coated cathode

6. DISCUSSION AND CONCLUSIONS

Rechargeable liquid ZABs meet certain critical demands considering next generation energy storage and conversion systems. ZABs display ultrahigh theoretical specific and volumetric energy density while they are composed mostly of accessible and inexpensive materials which do not exhibit any operation risk. Despite these promising features it is commonly recognized that the rechargeability and efficiency of these batteries are hindered mostly by poor reversibility of the air electrode, resulting from unresolved ORR and OER restrictions. Nanosized transition metal oxides and their composites are governing current references attempting to find scalable strategies to produce efficient bifunctional electrocatalysts for ZABs application. Perovskites have recently started to attract attention as catalysts towards balancing high electrochemical activity, stability, and low cost, while enhancing the environmental profile of the battery.

PBC and PBCF have been investigated by researchers as potential OER or ORR catalysts, however, according to author's knowledge there is no recent report studying the bifunctionality of those catalysts towards both reactions. In this thesis bulk powders PBC and PBCF were electrochemically characterized regarding their bifunctionality and applied in a rechargeable liquid ZAB. Electrochemical tests verify that both catalysts facilitate ORR, although PBCF exhibits enhanced OER properties compared to PBC. PBCF samples exhibit a lower onset overpotential (E_{onset}) and to reach higher current densities compared to the majority of PBC samples. Tafel plots also reveal improved activity of the Fe-Doped PBC. Cycling Voltammetries imply the bifunctional features of both perovskites. The results of electrocatalytic characterization were further confirmed by assembling and testing a laboratory ZAB with each catalyst applied as a cathode material. PBCF displayed better performance than PBC in both primary tests and rechargeability tests. The ZAB enriched with PBCF delivered a Peak Power Density of 99mWcm^{-2} while attained 30 galvanostatic continuous (20min) cycles at 2.3mAcm^{-2} preserving a Voltage Gap below 1V. After further 100 cycles at 3 mAcm^{-2} the cathode maintained stable polarization towards OER, while delivered a discharge voltage 0.8V. Moreover, EIS spectra of the cell with PBC develops higher resistances as soon as current is applied, while those resistances are vigorously increased comparing to the cell with the PBCF cathode.

As the perovskites were not in situ-synthesized, no information is available considering the morphology and size of particles, the micro-macro porosity or the specific surface area. These structure characteristics of materials are governing their catalytic properties. Moreover, cathodes were prepared by manual drop casting with a pipette, so the distribution of the catalyst ink in each experiment, besides the efforts, cannot be completely comparable. Thus, no confident comparison conclusions can be driven referring to the differences of the performance of PBC and PBCF. However, according to current knowledge regarding B-site doping, there is high possibility that Fe-doping cobalt sites of PBC is partially responsible for its enhanced OER and ORR activity. The first implication for such an assumption is that the B-site of the perovskite, consisting of a metal which can change valences, constitutes the “active site” of the perovskite which is mainly responsible for its electronic conductivity. Doping with a transition metal can alter the metal valence of the other B-metal into favorable valences which facilitate charge transfer between the transition metal cation and the reaction intermediates of OER [146] [147]. Furthermore, doping can lead to general crystal lattice modification due to A-site and B-site ionic radii mismatch generating oxygen vacancies [147]. Fe doping of cobalt sites inside the double perovskite $PrBa_{0.8}Ca_{0.2}Co_2O_{5+\delta}$, was also reported to promote oxygen transfer kinetics, while attributing to the catalyst durability towards ORR. Authors claim that stronger Fe-O bonds promote oxygen mobility towards and from the oxygen lattice in Pr-O layer [148]. Oxygen vacancies are of great importance in OER kinetics, as they function as ion donor-acceptor sites and provide mass transfer channels that can facilitate efficiently ORR, which is deeply dependent to ORR diffusion towards active sites [149]. Besides general examinations regarding B-site doping, Kim, B.-J., et al. [150] [151] also reported improved activity and resiliance of Fe-doped PBC perovskites towards OER. All the above considerations, give significant suggestions that Fe-doping of cobalt sites in PBC is probably principaly in charge of favorable performance of the catalyst when applied in the laboratory ZAB.

After investigating the performance of the two experimental cathodes in laboraroty ZABs, it is beneficial to provide some comparable results of recently applied catalysts in ZABs. In order to compare the performance of PBC and PBCF with other reports, catalysts that were evaluated in same current densities are cited in Table 1:

Table 1: Recently reported bifunctional catalysts’ performance when applied in ZAB systems

Catalyst	**OCV (V)**	**Peak Power Density (mWcm^{-2})**	**Cycling Life (cycles/min per cycle/charge & discharge current density mAcm^{-2})**	**Voltage Gap ($V_{discharge}$-V_{charge})**	**Reference**
Ce-doped $LaCoO_3$	1.426	60	160h ~20 min per cycle/2	1.2 V – 2V	**[119]**
$CoFe_2O_4$	1.47	142.2	15/20/3	1.25-2.4V	**[152]**
α-MnO_2	1.52	176	40/30/2	1.3 V -2V	**[153]**
MnO_2-MWCNTs	1.48	92	375/20/2	1.2V-2.1V	**[154]**
CoO-NSC	1.40	62	360/10/2	1.2V – 2V	**[155]**
$PrBa_{0.5}Sr_{0.5}Co_{1.9}Ni_{0.1}O_{5+\delta}$			20/- /1	1.3 V -2 V (cycle 20)	**[156]**
$Pr_{0.5}Ba_{0.5}CoO_{3-\delta}$		175	600/20/10	1.2 V -2V	**[64]**
$PrBaCo_{1.4}Fe_{0.6}O_{6-\delta}$	1.363	99	30/20/2.3 100/20/3	0.8-2V	**This work**
$PrBaCo_2O_{6-\delta}$	1.41	77	30/20/2.3 100/20/3	0.5-2.05V	**This work**

From the above data, it is clear that PBCF has comparable results towards OER facilitation and resiliance. PBCF could attain continious cycling at 2-3 mAcm^{-2} for 130 cycles with a stable polarization while charging at 2V. Although the Peak Power Density of PBCF reveals decent ORR promotion, its durability throughtout full disharge and polarization when cycling remains restricted. There are a number of explanations for this inadequate behavior. Firstly, PBCF was provided in bulk powders, where, despite manual grinding, the particles were likely to be highly agglomerated. The reports mentioned above refer to constructing nanosized catalysts with specific morphologies that provide very large surface area and porosity. These features offer high exposure to the electrolyte and thus offer active sites, but most importantly contain desirable oxygen transfer pathways which are of critical importance for ORR dynamics. On the contrary, PBCF being in bulk form did not possess the advantageous properties of unique nanostructures and relied only on its intrinsic catalytic activity.

Secondly, it is observed that some of the mentioned catalysts in Table and in the Introduction, exploit the synergistic effects of heterostructures consisting of different chemical species. This is a way to combine profitable ORR/OER properties of composites' contents and prevent aggregation of nanoparticles.

Finally, when conducting the battery tests, electrolyte leakage was detected in the cathode side after some hours of operation. Particularly after full discharge tests, in both PBC and PBCF tests, the "window" for ambient air entrance was observed wet from the electrolyte. This may be attributed to either inadequate practical assembly of the ZAB configuration, or insufficient content of a strongly a hydrophobic binder when preparing the cathode electrode. Electrolyte leakage is a general problem that can be arised during battery operation and is considered as a crucial factor leading to deterioration of ORR kinetics. When electrolyte blocks the entrance of oxygen molecules the oxidizing agent of the redox system cannot enter all the mass diffusion routes towards the TPBs and ORR activity is severely reduced, leading to damaging overpotentials.

In general, simultaneously decreasing overpotentials in cathodic ORR and anodic OER procedures remains a challenging subject challenge for metal-air batteries. Taking into consideration all the above data, PBCF appears to have promising performance towards OER and a potential use as an ORR catalyst if enhanced via some strategies. Future researches are encouraged firstly to experiment on different contents of partial substitution of Fe particles in the crystal lattice. There is a wide range of potential interactions between the components of doped PBC morphologies due to different content of Fe. Rational partial substitution of B-sites of its crystal lattice can promote a favorable synergism of tuned oxidation states or oxygen vacancies offering encouraging perspectives that may lead to more favorable ORR/OER kinetics. Secondly, it is suggested to explore appropriate procedures to synthesize unique nano-sized morphologies of PBCF particles. 3D hierarchical structures, ample with edges to perform as active sites and 1D structures, such as nanorods and nanofibers, usually show considerably prominent performance in catalysis. Electrospinning, as mentioned again in Chapter 0, proved to be a suitable route to synthesize perovskite nanofibers which profit from their enlarged active surface area. Finally, a combination of PBCF particles decorating carbonaceous highly porous structures could solve some of the problems derived from agglomerated PBCF particles. Porous carbon constitutes a conductive matrix with abundant with oxygen mobility pathways and could act like a stabilizing agent for active catalytic sites of PBCF.

7. PUBLICATIONS

In the frame of the present work the following publications have been prepared. Despite their diverse appearance they are all related to the topic of the present work, as all deal with materials suitable for electrode materials. Especially MOFs have been considered as potential materials for the present work but due to the limitations of the COVID-19 we were not able to investigate them.

1. Christos Vaitsis, Maria Mechili, Nikolaos Argirusis, Eirini Kanellou, Pavlos K. Pandis, Georgia Sourkouni, Antonis Zorpas and Christos Argirusis (July 13th 2020). Ultrasound-Assisted Preparation Methods of Nanoparticles for Energy-Related Applications, Nanotechnology and the Environment, Mousumi Sen, IntechOpen
2. Maria Mechili, Christos Vaitsis, Nikolaos Argirusis, Pavlos P. Pandis, Georgia Sourkouni, Christos Argirusis, (April 30th, 2021) “Research progress in transition metal oxide based bifunctional electrocatalysts for aqueous electrically rechargeable Zinc-Air Batteries” submitted to: Renewable and Sustainable Energy Reviews
3. Christos Vaitsis, Maria Mechili, Nikolaos Argirusis, Pavlos K. Pandis, Georgia Sourkouni, Christos Argirusis, (June 2021), MOF Nanomaterials for Cathodes, Chapter in book “Metal-Organic Framework-based Nanomaterials for Energy Applications” Elsevier
4. Maria Mechili, Christos Vaitsis, Nikolaos Argirusis, Pavlos K. Pandis, Georgia Sourkouni, Christos Argirusis, (June 2021), MOFs Nanocomposites for Cathodes, Chapter in book “Metal Organic Framework-based Nanomaterials for Energy Applications”, Elsevier

REFERENCES

1. European Commission, National Energy and Climate Plans: Member State contributions to the EU's 2030 climate ambition, September 2020.

2. European Commission, Communication from the Commission to the European Parliament, the Council, the European Economic and Social Committee and the Committee of the Regions: The European Green Deal, 2019.

3. European Commission, Communication from the Commission to the European Parliament, the Council, the European Economic and Social Committee and the Committee of the Regions : Annex to the Communication on the European Green Deal Roadmap - Key actions, 2019.

4. U.S. Environmental Protection Agency, . Landfill Gas Energy: A Guide to Developing and Implementing Greenhouse Gas Reduction Programs, 2012.

5. U.S. Environmental Protection Agency, On-Site Renewable Energy Generation: A Guide to Developing and Implementing Greenhouse Gas Reduction Programs, 2014.

6. Fathima, A.H. and K. Palanisamy, *8 - Renewable systems and energy storages for hybrid systems*, in *Hybrid-Renewable Energy Systems in Microgrids*, A.H. Fathima, et al., Editors. 2018, Woodhead Publishing. p. 147-164.

7. Revankar, S.T., *Chapter Six - Chemical Energy Storage*, in *Storage and Hybridization of Nuclear Energy*, H. Bindra and S. Revankar, Editors. 2019, Academic Press. p. 177-227.

8. Costa, C.M., et al., *Recycling and environmental issues of lithium-ion batteries: Advances, challenges and opportunities.* Energy Storage Materials, 2021. **37**: p. 433-465.

9. Lee, J.-s., et al., *Metal–Air Batteries with High Energy Density: Li–Air versus Zn–Air.* Advanced Energy Materials, 2011. **1**: p. 34-50.

10. Tahil, W. *The Zinc Air Battery and the Zinc Economy: A Virtuous Circle*. 2007.

11. Harting, K., U. Kunz, and T. Turek, *Zinc-air Batteries: Prospects and Challenges for Future Improvement.* Zeitschrift für Physikalische Chemie, 2012. **226**(2): p. 151-166.

12. Arai, H. and M. Hayashi, *PRIMARY BATTERIES – AQUEOUS SYSTEMS | Zinc–Air*, in *Encyclopedia of Electrochemical Power Sources*, J. Garche, Editor. 2009, Elsevier: Amsterdam. p. 55-61.

13. *Zn–Air Batteries*, in *Metal-Air Batteries*. 2018. p. 265-291.

14. Gilligan, G.E. and D. Qu, *Chapter 12 - Zinc-air and other types of metal-air batteries*, in *Advances in Batteries for Medium and Large-Scale Energy Storage*, C. Menictas, M. Skyllas-Kazacos, and T.M. Lim, Editors. 2015, Woodhead Publishing. p. 441-461.

15. Dobley, A., *Chapter 1 - Catalytic Batteries*, in *New and Future Developments in Catalysis: Batteries, Hydrogen Storage and Fuel Cells*, S.L. Suib, Editor. 2013, Elsevier: Amsterdam. p. 1-16.

16. Zhang, J., et al., *Zinc–air batteries: are they ready for prime time?* Chemical Science, 2019. **10**(39): p. 8924-8929.

17. Li, H., et al., *Advanced rechargeable zinc-based batteries: Recent progress and future perspectives.* Nano Energy, 2019. **62**: p. 550-587.

18. Zhou, T., et al., *Surface/interface nanoengineering for rechargeable Zn–air batteries.* Energy & Environmental Science, 2020. **13**(4): p. 1132-1153.

19. Chao, H., et al., *Design Strategy of Non-precious Metal Based Bi-functional Catalysts for the Alkaline based Zinc-Air Battery.* Materials Horizons, 2019. **6**.

20. Pan, J., et al., *Advanced Architectures and Relatives of Air Electrodes in Zn–Air Batteries.* Advanced Science, 2018. **5**(4): p. 1700691.

21. Meng, F.-L., et al., *Recent Advances toward the Rational Design of Efficient Bifunctional Air Electrodes for Rechargeable Zn–Air Batteries.* Small Methods, 2018. **14**(32): p. 1703843.

22. Yan, X., Y. Ha, and R. Wu, *Binder-Free Air Electrodes for Rechargeable Zinc-Air Batteries: Recent Progress and Future Perspectives.* Small Methods: p. 2000827.

23. Seh, Z.W., et al., *Combining theory and experiment in electrocatalysis: Insights into materials design.* Science, 2017. **355**(6321): p. eaad4998.

24. Wang, R., et al., *Nanocarbon-Based Electrocatalysts for Rechargeable Aqueous Li/Zn-Air Batteries.* ChemElectroChem, 2018. **5**(14): p. 1745-1763.

25. Wei, Q., et al., *Rational design of carbon-based oxygen electrocatalysts for zinc–air batteries.* Current Opinion in Electrochemistry, 2017. **4**(1): p. 45-59.

26. Zhang, W., et al., *Recent Advances in Isolated Single-Atom Catalysts for Zinc Air Batteries: A Focus Review.* Nanomaterials, 2019. **9**: p. 1402.

27. Davari, E. and D.G. Ivey, *Bifunctional electrocatalysts for Zn–air batteries.* Sustainable Energy & Fuels, 2018. **2**(1): p. 39-67.

28. Yi, J., et al., *Non-noble Iron Group (Fe, Co, Ni)-Based Oxide Electrocatalysts for Aqueous Zinc–Air Batteries: Recent Progress, Challenges, and Perspectives.* Organometallics, 2018. **38**.

29. Linden, D. and T. Reddy, *Handbook of Batteries*. 2001: McGraw-Hill Education.

30. Jain, P., et al., *History and Development of Zinc Batteries*, in *Zinc Batteries*. 2020. p. 167-186.

31. Li, Y. and H. Dai, *Recent advances in Zinc-air batteries.* Chemical Society reviews, 2014. **43**.

32. Jain, P., et al., *History and Development of Zinc Batteries*. 2020.

33. Fu, J., et al., *Electrically Rechargeable Zinc-Air Batteries: Progress, Challenges, and Perspectives.* Advanced Materials, 2016. **29**.

34. Mainar, A.R., et al., *Alkaline aqueous electrolytes for secondary zinc-air batteries: an overview.* International Journal of Energy Research, 2016. **40**: p. n/a-n/a.

35. Mainar, A.R., et al., *A brief overview of secondary zinc anode development: The key of improving zinc-based energy storage systems.* International Journal of Energy Research, 2017. **42**.

36. Yi, J., et al., *Challenges, Mitigation Strategies and Perspectives in Development of Zinc-electrode Materials/Fabrications for Rechargeable Zinc-air Batteries.* Energy & Environmental Science, 2018. **11**.

37. Guo, L., et al., *Inhibition of Zinc Dendrites in Zinc-Based Flow Batteries.* Frontiers in Chemistry, 2020. **8**(557).

38. Lao-atiman, W., et al., *Model-Based Analysis of an Integrated Zinc-Air Flow Battery/Zinc Electrolyzer System.* Frontiers in Energy Research, 2019. **7**(15).

39. Jin, W., et al., *Comparison of the oxygen reduction reaction between NaOH and KOH solutions on a Pt electrode: the electrolyte-dependent effect.* J Phys Chem B, 2010. **114**(19): p. 6542-8.

40. Clark, S., et al., *Towards Rechargeable Zinc-Air Batteries with Aqueous Chloride Electrolytes.* Journal of Materials Chemistry A, 2019. **7**.

41. Chen, P., et al., *Recent Progress in Electrolytes for Zn–Air Batteries.* Frontiers in Chemistry, 2020. **8**(372).

42. Mainar, A.R., et al., *An overview of progress in electrolytes for secondary zinc-air batteries and other storage systems based on zinc.* Journal of Energy Storage, 2018. **15**: p. 304-328.

43. Tsehaye, M.T., et al., *Membranes for zinc-air batteries: Recent progress, challenges and perspectives.* Journal of Power Sources, 2020. **475**: p. 228689.

44. Tsehaye, M.T., F. Alloin, and C. Iojoiu, *Prospects for Anion-Exchange Membranes in Alkali Metal–Air Batteries.* Energies, 2019. **12**: p. 4702.

45. Arora, P. and Z. Zhang, *Battery Separators.* Chemical Reviews, 2004. **104**(10): p. 4419-4462.

46. Kiros, Y., *Separation and permeability of zincate ions through membranes.* Journal of Power Sources, 1996. **62**(1): p. 117-119.

47. Hwang, H.J., et al., *Selective Ion Transporting Polymerized Ionic Liquid Membrane Separator for Enhancing Cycle Stability and Durability in Secondary Zinc–Air Battery Systems.* ACS Applied Materials & Interfaces, 2016. **8**(39): p. 26298-26308.

48. Wu, G.M., et al., *Study of high-anionic conducting sulfonated microporous membranes for zinc-air electrochemical cells.* Materials Chemistry and Physics, 2008. **112**: p. 798-804.

49. Lee, H.-J., et al., *Electrospun polyetherimide nanofiber mat-reinforced, permselective polyvinyl alcohol composite separator membranes: A membrane-driven step closer toward rechargeable zinc–air batteries.* Journal of Membrane Science, 2016. **499**: p. 526-537.

50. Nanthapong, S., S. Kheawhom, and C. Klaysom, *MCM-41/PVA Composite as a Separator for Zinc–Air Batteries.* International Journal of Molecular Sciences, 2020. **21**: p. 7052.

51. Kim, H.-W., et al., *Artificially-engineered, bicontinuous anion-conducting/-repelling polymeric phases as a selective ion transport channel for rechargeable zinc-air battery separator membranes.* Journal of Materials Chemistry A, 2016. **4**.

52. Vaitsis, C., et al., *Ultrasound-Assisted Preparation Methods of Nanoparticles for Energy-Related Applications*, in *Nanotechnology and the Environment*. 2020, IntechOpen. p. 77-103.

53. Wragg, A.A., A. Einarsson, and J.L. Dawson, *Oxygen transport at porous air electrodes: Experimental.* Electrochimica Acta, 1974. **19**(8): p. 503-510.

54. Haas, O., et al., *Metal/Air Batteries: the Zinc Air Case*. 2010.

55. Jöerissen, L., *SECONDARY BATTERIES – METAL-AIR SYSTEMS | Bifunctional Oxygen Electrodes*. 2009. p. 356-371.

56. Wu, M., et al., *Rational design of multifunctional air electrodes for rechargeable Zn–Air batteries: Recent progress and future perspectives.* Energy Storage Materials, 2019. **21**: p. 253-286.

57. Wang, X., et al., *High-Performance Platinum-Perovskite Composite Bifunctional Oxygen Electrocatalyst for Rechargeable Zn–Air Battery.* Advanced Energy Materials, 2020. **10**(5): p. 1903271.

58. Moni, P., et al., *A new silicon oxycarbide based gas diffusion layer for zinc-air batteries.* Journal of Colloid and Interface Science, 2020. **577**: p. 494-502.

59. Xu, N., et al., *Self-assembly formation of Bi-functional Co3O4/MnO2-CNTs hybrid catalysts for achieving both high energy/power density and cyclic ability of rechargeable zinc-air battery.* Scientific Reports, 2016. **6**(1): p. 33590.

60. Ó'Laoire, C., *Investigations of oxygen reduction reactions in non-aqueous electrolytes and the lithium-air battery.* Chemistry Dissertations, 2010.

61. Laoire, C.O., et al., *Rechargeable Lithium/TEGDME- LiPF6 O2 Battery.* Journal of The Electrochemical Society, 2011. **158**.

62. Park, J., et al., *A review of the gas diffusion layer in proton exchange membrane fuel cells: Durability and degradation.* Applied Energy, 2015. **155**: p. 866-880.

63. Park, G.-G., et al., *Effect of PTFE contents in the gas diffusion media on the performance of PEMFC.* Journal of Power Sources, 2004. **131**(1): p. 182-187.

64. Gui, L., et al., *Oxygen vacancies-rich Ce0.9Gd0.1O2-δ decorated Pr0.5Ba0.5CoO3-δ bifunctional catalyst for efficient and long-lasting rechargeable Zn-air batteries.* Applied Catalysis B: Environmental, 2020. **266**: p. 118656.

65. Park, S., et al., *Fabrication of GDL microporous layer using PVDF for PEMFCs.* Journal of Physics: Conference Series, 2009. **165**: p. 012046.

66. *Israel Cabasso; Youxin Yuan and Xiao Xu, GAS DIFFUSiON ELECTRODES BASED ON POLYOVINYLIDENE FLUORIDE) CARBON BLENDS, United States Patent 5,783,325*. 1996 The Research Foundation of State of New York. Albany, N.Y. .

67. Yan, W.-M., et al., *Effects of fabrication processes and material parameters of GDL on cell performance of PEM fuel cell.* International Journal of Hydrogen Energy, 2007. **32**(17): p. 4452-4458.

68. Park, S. and Y. Park, *Fabrication of gas diffusion layer (GDL) containing microporous layer using flourinated ethylene prophylene (FEP) for proton exchange membrane fuel cell (PEMFC).* International Journal of Precision Engineering and Manufacturing, 2012. **13**.

69. Price, S.W.T., et al., *The fabrication of a bifunctional oxygen electrode without carbon components for alkaline secondary batteries.* Journal of Power Sources, 2014. **259**: p. 43-49.

70. Ha, T., et al., *Experimental study on carbon corrosion of the gas diffusion layer in polymer electrolyte membrane fuel cells.* International Journal of Hydrogen Energy, 2011. **36**(19): p. 12436-12443.

71. Perry, M., T. Patterson, and T. Madden, *GDL degradation in PEFC*. Vol. 33. 2010. 1081-1087.

72. Schröder, D., et al., *Analyzing transport paths in the air electrode of a zinc air battery using X-ray tomography.* Electrochemistry Communications, 2014. **40**: p. 88-91.

73. Clark, M.P., et al., *High Performance Oxygen Reduction/Evolution Electrodes for Zinc–Air Batteries Prepared by Atomic Layer Deposition of MnOx.* ACS Applied Energy Materials, 2020. **3**(1): p. 603-613.

74. Li, X., et al., *A novel bifunctional oxygen GDE for alkaline secondary batteries.* Electrochemistry Communications, 2013. **34**: p. 228-230.

75. Wang, P., et al., *Construction of mass-transfer channel in air electrode with bifunctional catalyst for rechargeable zinc-air battery.* Electrochimica Acta, 2019. **320**: p. 134564.

76. Xu, N., et al., *Flexible self-supported bi-metal electrode as a highly stable carbon- and binder-free cathode for large-scale solid-state zinc-air batteries.* Applied Catalysis B: Environmental, 2020. **272**: p. 118953.

77. Lee, D.U., et al., *Advanced Extremely Durable 3D Bifunctional Air Electrodes for Rechargeable Zinc-Air Batteries.* Advanced Energy Materials, 2014. **4**(6): p. 1301389.

78. Wan, L., et al., *Janus-Typed Integrated Bifunctional Air Electrode with MnOx-NiFe LDH/Ni Foam for Rechargeable Zinc-Air Batteries.* Journal of The Electrochemical Society, 2019. **166**(14): p. A3409-A3415.

79. Zeng, S., et al., *All-in-One Bifunctional Oxygen Electrode Films for Flexible Zn-Air Batteries.* Small, 2018. **14**.

80. Shi, F., X. Zhu, and W. Yang, *Micro-nanostructural designs of bifunctional electrocatalysts for metal-air batteries.* Chinese Journal of Catalysis, 2020. **41**(3): p. 390-403.

81. Gattrell, M. and B. MacDougall, *Reaction mechanisms of the O2 reduction/evolution reaction*, in *Handbook of Fuel Cells*.

82. Spendelow, J.S. and A. Wieckowski, *Electrocatalysis of oxygen reduction and small alcohol oxidation in alkaline media.* Physical Chemistry Chemical Physics, 2007. **9**(21): p. 2654-2675.

83. Ge, X., et al., *Oxygen Reduction in Alkaline Media: From Mechanisms to Recent Advances of Catalysts.* ACS Catalysis, 2015. **5**(8): p. 4643-4667.

84. Wang, X., et al., *Review of Metal Catalysts for Oxygen Reduction Reaction: From Nanoscale Engineering to Atomic Design.* Chem, 2019. **5**(6): p. 1486-1511.

85. Badruzzaman, A., et al., *Recent advances in cobalt based heterogeneous catalysts for oxygen evolution reaction.* Inorganica Chimica Acta, 2020. **511**: p. 119854.

86. Pan, Q. and L. Wang, *Recent perspectives on the structure and oxygen evolution activity for non-noble metal-based catalysts.* Journal of Power Sources, 2021. **485**: p. 229335.

87. Jamesh, M.-I. and M. Harb, *Tuning the electronic structure of the earth-abundant electrocatalysts for oxygen evolution reaction (OER) to achieve efficient alkaline water splitting – A review.* Journal of Energy Chemistry, 2021. **56**: p. 299-342.

88. Wu, G., et al., *Carbon nanocomposite catalysts for oxygen reduction and evolution reactions: From nitrogen doping to transition-metal addition.* Nano Energy, 2016. **29**: p. 83-110.

89. Osgood, H., et al., *Transition metal (Fe, Co, Ni, and Mn) oxides for oxygen reduction and evolution bifunctional catalysts in alkaline media.* Nano Today, 2016. **11**(5): p. 601-625.

90. Li, S., et al., *Chapter 6 - Advanced nanomaterials for efficient oxygen electrodes in metal–air batteries*, in *Advanced Nanomaterials for Electrochemical-Based Energy Conversion and Storage*, F. Ran and S. Chen, Editors. 2020, Elsevier. p. 191-222.

91. Zhang, Y., et al., *In situ grown cobalt phosphide (CoP) on perovskite nanofibers as an optimized trifunctional electrocatalyst for Zn–air batteries and overall water splitting.* Journal of Materials Chemistry A, 2019. **7**.

92. Li, Y.J., et al., *Multiscale Structural Engineering of Ni-Doped CoO Nanosheets for Zinc-Air Batteries with High Power Density.* Adv Mater, 2018. **30**(46): p. 1804653.

93. Béjar, J., et al., *An advanced three–dimensionally ordered macroporous NiCo2O4 spinel as bifunctional electrocatalyst for rechargeable Zn–Air batteries.* Journal of Materials Chemistry A, 2020. **8**.

94. Xu, N., et al., *Superior stability of a bifunctional oxygen electrode for primary, rechargeable and flexible Zn–air batteries.* Nanoscale, 2018. **10**(28): p. 13626-13637.

95. Cheng, F. and J. Chen, *Metal–air batteries: from oxygen reduction electrochemistry to cathode catalysts.* Chemical Society Reviews, 2012. **41**(6): p. 2172-2192.

96. Wang, H.-F. and Q. Xu, *Materials Design for Rechargeable Metal-Air Batteries.* Matter, 2019. **1**(3): p. 565-595.

97. Yanqiang, L., et al., *2D nanoplate assembled nitrogen doped hollow carbon sphere decorated with Fe3O4 as an efficient electrocatalyst for oxygen reduction reaction and Zn-air batteries.* Nano Research, 2019. **12**.

98. Mai, Z., et al., *Integrating ZnCo2O4 submicro/nanospheres with CoxSey nanosheets for the oxygen evolution reaction and zinc–air batteries.* Sustainable Energy & Fuels, 2020. **4**(5): p. 2184-2191.

99. Li, L., et al., *Anchoring Mn3O4 Nanoparticles on Oxygen Functionalized Carbon Nanotubes as Bifunctional Catalyst for Rechargeable Zinc-Air Battery.* ACS Applied Energy Materials, 2018. **1**(3): p. 963-969.

100. An, K., et al., *Filter paper derived three-dimensional mesoporous carbon with Co3O4 loaded on surface: An excellent binder-free air-cathode for rechargeable Zinc-air battery.* Journal of Solid State Chemistry, 2019. **270**: p. 539-546.

101. Majee, R., S. Mondal, and S. Bhattacharyya, *Charge transfer from perovskite oxide nanosheets to N-doped carbon nanotubes to promote enhanced performance of a zinc–air battery.* Chemical Communications, 2020. **56**(59): p. 8277-8280.

102. Levy, M., *Crystal Structure and Defect Properties in Ceramic Materials*, in *Department of Materials*

Imperial College of Science, Technology and Medicine. January 2005, University of London.

103. Kim, N.-I., et al., *B-site doping effects of NdBa0.75Ca0.25Co2O5+δ double perovskite catalysts for oxygen evolution and reduction reactions.* Journal of Materials Chemistry A, 2018. **6**(36): p. 17807-17818.

104. Pandis, P. and C. Ftikos, *Oxygen Permeation Study through dense ceramic membranes with perovskite structure (Ba0,8Sr0,2MxB1-xO3±δ, M=Co,Al, B=Mn,Fe,Ni)*, in *11th International Conference and Exhibition of the European Ceramic Society* 2009: Krakow, Poland.

105. Argirusis, C., et al., *Study of the oxygen incorporation and diffusion in Sr(Ti0.65Fe0.35)O3 ceramics.* Solid State Ionics, 2011. **192**: p. 9–11.

106. Bu, Y., et al., *Synergistic interaction of perovskite oxides and N-doped graphene in versatile electrocatalyst.* Journal of Materials Chemistry A, 2019. **7**(5): p. 2048-2054.

107. Zhang, L., et al., *Co-deficient PrBaCo2−xO6−δ perovskites as cathode materials for intermediate-temperature solid oxide fuel cells: Enhanced electrochemical performance and oxygen reduction kinetics.* International Journal of Hydrogen Energy, 2018. **43**(7): p. 3761-3775.

108. Noll, F., et al., *SrTiO3 as a prototype of a mixed conductor Conductivities, oxygen diffusion and boundary effects.* Solid State Ionics, 1996. **86-88**: p. 711-717.

109. Strandbakke, R., et al., *Gd- and Pr-based double perovskite cobaltites as oxygen electrodes for proton ceramic fuel cells and electrolyser cells.* Solid State Ionics, 2015. **278**: p. 120-132.

110. Kharlamova, T., et al., *Perovskite and Composite Materials for Intermediate Temperatures Solid Oxide Fuel Cells.* MRS Online Proceedings Library, 2008. **1056**(1): p. 364.

111. Bu, Y., et al., *A Highly Efficient and Robust Cation Ordered Perovskite Oxide as a Bifunctional Catalyst for Rechargeable Zinc-Air Batteries.* ACS Nano, 2017. **11**(11): p. 11594-11601.

112. Zhang, Y., et al., *The Synergistic Effect Accelerates the Oxygen Reduction/Evolution Reaction in a Zn-Air Battery.* Frontiers in Chemistry, 2019. **7**.

113. Yan, Z., et al., *Rapid low-temperature synthesis of perovskite/carbon nanocomposites as superior electrocatalysts for oxygen reduction in Zn-air batteries.* Nano Research, 2017. **11**.

114. Gaki, A., et al., *Synthesis and characterization of La0.8Sr0.2MnO 3 nanopowders through a modified pechini technique*, in *A Global Road Map for Ceramic Materials and Technologies: Forecasting the Future of Ceramics, International Ceramic Federation - 2nd International Congress on Ceramics*. 2008.

115. Kuai, L., et al., *Mesoporous LaMnO3+δ perovskite from spray−pyrolysis with superior performance for oxygen reduction reaction and Zn−air battery.* Nano Energy, 2018. **43**: p. 81-90.

116. Miao, H., et al., *A-site deficient/excessive effects of LaMnO3 perovskite as bifunctional oxygen catalyst for zinc-air batteries.* Electrochimica Acta, 2020. **333**: p. 135566.

117. Kanagaraj, I., P. M, and P. Annigere, *Highly nanocrystalline interconnected La0.5Ca0.5CoO3-δ as an efficient bi-functional electrocatalyst for zinc-air battery with structural and morphological evidence for ZnO mitigation.* Sustainable Energy & Fuels, 2019. **3**.

118. Ishihara, T., et al., *Mesoporous La0.6Ca0.4CoO3 Perovskite with Large Surface Area as Stable Air Electrode for Zn-air Rechargeable Battery.* Journal of Materials Chemistry A, 2018. **6**.

119. Qian, J., et al., *Engineered spin state in Ce doped LaCoO3 with enhanced electrocatalytic activity for rechargeable Zn-Air batteries.* Nano Energy, 2020. **74**: p. 104948.

120. Lee, H., et al., *Advanced Electrochemical Properties of PrBa0.5Sr0.5Co1.9Ni0.1O5+δ as a Bifunctional Catalyst for Rechargeable Zinc-Air Batteries.* ChemElectroChem, 2019. **6**.

121. Liu, Q., et al., *Recent advances in energy materials by electrospinning.* Renewable and Sustainable Energy Reviews, 2018. **81**: p. 1825-1858.

122. Bian, J., et al., *Mg Doped Perovskite LaNiO3 Nanofibers as an Efficient Bifunctional Catalyst for Rechargeable Zinc–Air Batteries.* ACS Applied Energy Materials, 2019. **2**(1): p. 923-931.

123. Wang, Q., et al., *La0.8Sr0.2Co1-xMnxO3 perovskites as efficient bi-functional cathode catalysts for rechargeable zinc-air batteries.* Electrochimica Acta, 2017. **254**: p. 14-24.

124. Li, P., et al., *La1.7Sr0.3Co0.5Ni0.5O4+δ layered perovskite as an efficient bifunctional electrocatalyst for rechargeable zinc-air batteries.* Applied Surface Science, 2019. **464**: p. 494-501.

125. Huet, F., *A review of impedance measurements for determination of the state-of-charge or state-of-health of secondary batteries.* Journal of Power Sources, 1998. **70**(1): p. 59-69.

126. *Electrochemical Research Techniques*, in *Fundamentals of Electrochemistry*. 2005. p. 191-215.

127. *Experimental Design*, in *Electrochemical Impedance Spectroscopy*. 2008. p. 129-152.

128. *Equivalent Circuit Analogs*, in *Electrochemical Impedance Spectroscopy*. 2008. p. 153-162.

129. Middlemiss, L.A., et al., *Characterisation of batteries by electrochemical impedance spectroscopy.* Energy Reports, 2020. **6**: p. 232-241.

130. Macdonald, D.D., *Reflections on the history of electrochemical impedance spectroscopy.* Electrochimica Acta, 2006. **51**(8): p. 1376-1388.

131. *Electrical Circuits*, in *Electrochemical Impedance Spectroscopy*. 2008. p. 61-72.

132. Bontempelli, G., N. Dossi, and R. Toniolo, *Linear Sweep and Cyclic*, in *Reference Module in Chemistry, Molecular Sciences and Chemical Engineering*. 2016, Elsevier.

133. Fang, Y.-H. and Z.-P. Liu, *Tafel Kinetics of Electrocatalytic Reactions: From Experiment to First-Principles.* ACS Catalysis, 2014. **4**(12): p. 4364-4376.

134. Dickinson, E.J.F. and A.J. Wain, *The Butler-Volmer equation in electrochemical theory: Origins, value, and practical application.* Journal of Electroanalytical Chemistry, 2020. **872**: p. 114145.

135. Gu, X.-K., S. Samira, and E. Nikolla, *Oxygen Sponges for Electrocatalysis: Oxygen Reduction/Evolution on Nonstoichiometric, Mixed Metal Oxides.* Chemistry of Materials, 2018. **30**(9): p. 2860-2872.

136. Pan, Y., et al., *Direct evidence of boosted oxygen evolution over perovskite by enhanced lattice oxygen participation.* Nature Communications, 2020. **11**(1): p. 2002.

137. Negahdar, L., et al., *Mechanistic Aspects of the Electrocatalytic Oxygen Evolution Reaction over Ni−Co Oxides.* ChemElectroChem, 2019. **6**(22): p. 5588-5595.

138. Biesheuvel, M., S. Porada, and J. Dykstra, *The difference between Faradaic and non-Faradaic electrode processes*. 2018.

139. Zu, C.-X. and H. Li, *Thermodynamic analysis on energy densities of batteries.* Energy & Environmental Science, 2011. **4**(8): p. 2614-2624.

140. Lee, J.-S., et al., *Metal–Air Batteries with High Energy Density: Li–Air versus Zn–Air.* Advanced Energy Materials, 2011. **1**(1): p. 34-50.

141. Li, Y. and J. Lu, *Metal-Air Batteries: Will They Be Future Electrochemical Energy Storage of Choice?* ACS Energy Letters, 2017. **2**.

142. Tornheim, A. and D.C. O'Hanlon, *What do Coulombic Efficiency and Capacity Retention Truly Measure? A Deep Dive into Cyclable Lithium Inventory, Limitation Type, and Redox Side Reactions.* Journal of The Electrochemical Society, 2020. **167**(11): p. 110520.

143. J. Balej, K.B.a.O.S., *Possibility of producing hydrogen peroxide by cathodic reduction of oxygen.* Institute of Inorganic Chemistry, 1975.

144. Bajracharya, S., et al., *6 - Cathodes for microbial fuel cells*, in *Microbial Electrochemical and Fuel Cells*, K. Scott and E.H. Yu, Editors. 2016, Woodhead Publishing: Boston. p. 179-213.

145. He, D., et al., *Hydrogen peroxide electrosynthesis via regulating the oxygen reduction reaction pathway on Pt noble metal with ion poisoning.* Electrochimica Acta, 2021. **371**: p. 137721.

146. Wang, H., et al., *Perovskite oxides as bifunctional oxygen electrocatalysts for oxygen evolution/reduction reactions – A mini review.* Applied Materials Today, 2019. **16**: p. 56-71.

147. Badreldin, A., A. Abusrafa, and A. Abdel-Wahab, *Oxygen-deficient perovskites for oxygen evolution reaction in alkaline media: a review.* Emergent Materials, 2020. **3**.

148. Lim, C., et al., *Investigation of the Fe doping effect on the B-site of the layered perovskite PrBa0.8Ca0.2Co2O5+δ for a promising cathode material of the intermediate-temperature solid oxide fuel cells.* International Journal of Hydrogen Energy, 2019. **44**(2): p. 1088-1095.

149. Rincón Ovalles, R., et al., *Evaluation of Perovskites as Electrocatalysts for the Oxygen Evolution Reaction.* ChemPhysChem, 2014. **15**.

150. Kim, B.-J., et al., *Oxygen evolution reaction activity and underlying mechanism of perovskite electrocatalysts at different pH.* Materials Advances, 2021. **2**(1): p. 345-355.

151. Kim, B.-J., et al., *Fe-Doping in Double Perovskite PrBaCo2(1-x)Fe2xO6-δ: Insights into Structural and Electronic Effects to Enhance Oxygen Evolution Catalyst Stability.* Catalysts, 2019. **9**(3): p. 263.

152. Yin, J., et al., *CoFe2O4 nanoparticles as efficient bifunctional catalysts applied in Zn–air battery.* Journal of Materials Research, 2017. **33**(5): p. 590-600.

153. Meng, J., et al., *Spent alkaline battery-derived manganese oxides as efficient oxygen electrocatalysts for Zn–air batteries.* Inorganic Chemistry Frontiers, 2018. **5**(9): p. 2167-2173.

154. Vayenas, M., et al., *Investigation of alternative materials as bifunctional catalysts for electrochemical applications.* Chimica Techno Acta, 2019. **6**(4): p. 120-129.

155. Chen, S., et al., *Bifunctional Oxygen Electrocatalysis of N, S-Codoped Porous Carbon with Interspersed Hollow CoO Nanoparticles for Rechargeable Zn-Air Batteries.* ACS Appl Mater Interfaces, 2019. **11**(18): p. 16720-16728.

156. Lee, H., et al., *Advanced Electrochemical Properties of PrBa0.5Sr0.5Co1.9Ni0.1O5+δ as a Bifunctional Catalyst for Rechargeable Zinc-Air Batteries.* ChemElectroChem, 2019. **6**(12): p. 3154-3159.